$$z_s = 35.21734 \text{ cm at } \tilde{\xi} = 7$$

$$z_s = 59.48100 \text{ cm at } \tilde{\xi} = 8$$

$$z_s = 100.0000 \text{ cm at } \tilde{\xi} = 9$$

The first and second derivatives of $\tilde{\xi}$ with respect to z_s can be evaluated exactly,

$$\frac{\partial \tilde{\xi}}{\partial z_s} = \frac{A'}{1+z_s} \tag{4.3}$$

$$\frac{\partial^2 \tilde{\xi}}{\partial z_s^2} = - \frac{A'}{(1+z_s)^2} \tag{4.4}$$

Equation (4.1) is transformed into $\tilde{\xi}$-coordinates and becomes,

$$\frac{\partial T_s}{\partial t} = K_s \left[\frac{\partial T_s}{\partial \tilde{\xi}} \frac{\partial^2 \tilde{\xi}}{\partial z_s^2} + \frac{\partial^2 T_s}{\partial \tilde{\xi}^2} \left(\frac{\partial \tilde{\xi}}{z_s} \right)^2 \right] \tag{4.5}$$

4.3 Equation for the Steady State.

The equation for the steady state is obtained by setting the time derivative to zero, in which case (4.1) reduces to,

$$K_s \frac{\partial^2 T_s}{\partial z_s^2} = 0 \tag{4.6}$$

This implies that,

$$\frac{\partial T_s}{\partial z_s} = \text{constant} = C \tag{4.7}$$

Under steady-state conditions we will obtain a linear variation in the soil temperature.

4.4 Time-Dependent Equation.

We will use an implicit finite-difference approximation to the time-dependent equation so that the computations will be absolutely stable. The implicit scheme is the same as the one for the atmospheric equations in which the time derivative is evaluated at the time

$t_o + \frac{1}{2}\Delta t$. We transform (4.5) into a finite-difference equation and make use of the fact that $\Delta\xi = \Delta k = 1$ to get,

$$T_s(k_o,t_o+\Delta t)[1+\Delta t\ K_s DDZ2(k_o)] = T_s(k_o,t_o) + \frac{\Delta t}{2} K_s\{[T_s(k_o+1,t_o)+T_s(k_o+1,t_o+\Delta t)-T_s(k_o-1,t_o)-T_s(k_o-1,t_o+\Delta t)]\ DD2Z(k_o)+[T_s(k_o+1,t_o)+T_s(k_o+1,t_o+\Delta t)-2T_s(k_o,t_o)-2T_s(k_o,t_o+\Delta t)+T_s(k_o-1,t_o)+T_s(k_o-1,t_o+\Delta t)]\ DDZ2(k_o)\} \tag{4.8}$$

where,

$$DDZ2(k_o) = \left(\frac{\partial \xi}{\partial z_s}\right)^2\Big|_{k_o}$$

$$DD2Z(k_o) = \frac{1}{2}\left(\frac{\partial^2 \xi}{\partial z_s^2}\right)\Big|_{k_o}$$

4.5 Initial Soil Temperature Profile.

The urban heat island model is started at the time of maximum temperature because the atmospheric heat flux is approximately zero near the ground at that time. However, it is probable that the soil heat flux reaches its maximum value near the time of maximum surface temperature so that a special initialization is needed for the soil temperature profile. This can be done by integrating the soil equation for a few days of real time, letting the surface temperature vary according to a diurnal cycle as given by a cyclic function like a sine. At the end of a few days of real time the soil temperature profile should have adjusted to a value fairly close to the one it should have over a diurnal cycle. The soil temperature profile computed at the time of maximum temperature will be used as the initial soil temperature profile in the urban heat island model. However, the exact amplitude of the diurnal temperature wave is not generally known *a priori* so that the derived temperature profile must be put into a form which would

be useable for any temperature difference between the surface and the lower boundary. This is done by computing ZS(k) which gives a weight to DIFF, the temperature difference between the surface and the lower boundary, at each grid point.

$$DIFF = T_s(0) - T_s(9) \tag{4.9}$$

And ZS(k) is defined by,

$$ZS(k) = \left[T_s(k) - T_s(9)\right]/DIFF \tag{4.10}$$

Therefore, in the complete program for the steady state, we will not compute the temperature profile but assume it to be of the form,

$$T_s(k) = T_s(9) + ZS(k) \times \left[T_s(0) - T_s(9)\right] \tag{4.11}$$

Equation (4.11) should give better initial conditions than (4.7) which assumes a linear variation of temperature in the soil.

CHAPTER V

SURFACE TEMPERATURE

The temperature at the earth's surface is determined by a heat-balance equation which includes long-wave and short-wave radiation, heat flux from the ground, latent and sensible heat fluxes from the atmosphere and artificial heat input generated by a city.

$$R_n = -(\rho C_p H + \rho_s c_s S + \rho L E) + A \qquad (5.1)$$

where, R_n = net radiation at the earth's surface,

ρ = atmospheric air density,

ρ_s = density of the soil,

C_p = heat capacity at constant pressure of the atmosphere,

c_s = heat capacity of the soil,

L = latent heat of vaporization,

H = sensible heat flux from the atmosphere,

E = latent heat flux from the atmosphere,

S = sensible heat flux from the soil,

A = artificial heat.

5.1 Net Radiation.

The radiation balance at the earth's surface is,

$$R_n = I_a + R\downarrow - R\uparrow \qquad (5.2)$$

where, I_a = net solar radiation,

$R\downarrow$ = infrared sky radiation,

$R\uparrow$ = terrestrial outgoing infrared radiation

5.1.1 Outgoing Terrestrial Infrared Radiation.

We will assume that the earth's surface radiates like a gray body,

$$R\uparrow = \varepsilon_1 \sigma T^4 \qquad (5.3)$$

where, ε_1 = emissivity of the earth's surface

σ = Stefan-Boltzmann constant

T = temperature of the earth's surface

5.1.2 Sky Infrared Radiation.

Most of the sky infrared radiation is emitted by water vapor and carbon dioxide. The exact radiation transfer equations become extremely complex when we divide the spectrum into many frequency bands in order to model the selective absorptivity and emissivity of H_2O and CO_2. In order to keep the model simple it is necessary to average the infrared radiation over all of the spectrum. The climatological models which use only the observed temperature and humidity at the observing weather station are too simplistic. A compromise between accuracy and reasonable computing time is the Brooks (1950) model as described by Atwater (1966). Brooks has presented values of the emissivity ε and of $\frac{d\varepsilon}{dw}$, the slope of the emissivity curve for water vapor with respect to the path length w. Haltiner and Martin (1957) have modelled the infrared radiation due to the atmospheric carbon dioxide in terms of the infrared emission of the earth's surface,

$$R\downarrow (CO_2) = 0.18 \varepsilon_1 \sigma T^4 \qquad (5.4)$$

We will derive the radiative transfer equation for water

vapor. Our starting point is Schwarzschild's equation for monochromatic radiation,

$$dI_\nu = -\rho k_\nu [I_\nu - B_\nu(T)]\, ds \qquad (5.5)$$

where, I_ν = intensity of radiation at frequency ν,

k_ν = absorption coefficient of water vapor in a thin layer ds,

B_ν = blackbody radiance as given by Planck's law,

Now we relate ds to the absorber path length du,

$$ds = \sec\psi\, du \qquad (5.6)$$

where ψ = zenith angle.

We include the integral over the zenith angle in du and obtain for the downward radiation,

$$dI_\nu = k_\nu [I_\nu - B_\nu(T)]\, du \qquad (5.7)$$

We integrate (5.7) over frequency and path length,

$$F_\nu\downarrow(u = 0) = \int_0^\infty d\nu \int_0^{u_t} B\, \frac{\partial \tau(u,u')}{\partial u'}\, du' \qquad (5.8)$$

where u_t = total path length.

The Brooks model transforms (5.8) into a finite-difference equation,

$$F_w(0) = \sum_{j=1}^{n} \overline{(\sigma T^4)}_j \left(\frac{\partial \varepsilon}{\partial u}\right) \Delta u \qquad (5.9)$$

where Δu is the path length in a given layer as given by

$$\Delta u = \left(\frac{p}{1000}\right)^a 1000\, q\, \frac{\Delta p}{g} \qquad (5.10)$$

where, a = constant between $\frac{1}{2}$ and 1,

g = gravity,

p = pressure in millibars,

q = mixing ratio for water vapor.

Elliot and Stevens (1961) have derived equations for the emissivity from the data of Brooks (1950), and Hales et al. (1963) have presented an equation for short path lengths. In Table 2 we summarize these equations. The constant a which appears in (5.10) has to be determined from radiation experiments. Atwater (1967) points out that a value of ½ or 1 is used generally. In our model we will choose the simplest formulation (a=1) because the actual formulation for the infrared radiation is not a crucial factor in understanding the urban heat island when the radiative flux divergence is neglected.

In Appendix D we describe in detail how the computation of the infrared is done. In that computation we have made the assumption that the surface pressure is constant over the period of one day. This is justified because the actual value of the pressure is not used in the computation of the mean wind but only in the computation of the infrared flux. However, this is not a serious restriction because we can allow the surface pressure to vary according to the synoptic conditions if these are known.

5.1.3 Incoming Solar Radiation.

The solar radiation received at the earth's surface is,

$$I_a = R_o (1-a) \cos (Z) (T_r)^{\sec Z} \qquad (5.11)$$

where, R_o = solar constant,

a = albedo of the earth's surface,

T_r = transmissivity of the cloudless atmosphere,

Z = zenith solar angle determined by,

$$\cos Z = \sin (\varphi) \sin (\delta) - \cos (\varphi) \cos (\delta) \cos (2\pi \Omega t) \qquad (5.12)$$

TABLE 2. Equations used for emissivity in the Brooks method, as a function of total path length (cm). This table is a reproduction of Atwater's (1967) Table 2, p 827.

$\varepsilon = 0.1579 \log(1 + 4275\ w)$	$0 < w < 10^{-4}$
$\varepsilon = 0.0396 \ln w + 0.389$	$10^{-4} < w < 10^{-3}$
$\varepsilon = 0.0565 \ln w + 0.506$	$10^{-3} < w < 10^{-2}$
$\varepsilon = 0.0653 \ln w + 0.546$	$10^{-2} < w < 10^{-1}$
$\varepsilon = 0.0778 \ln w + 0.575$	$10^{-1} < w$

The first entry is from Hales et al. (1963) and the last four entries are from Elliot and Stevens (1961).

where, φ = latitude,

δ = solar declination which depends on the time of year and varies from 23° (summer) to -23° (winter)

Ω = earth's angular velocity.

5.2 Sensible Heat Flux from the Atmosphere.

The atmospheric heat flux is,

$$H = \lim_{z \to z_o} \left(K_t \frac{\partial \Theta}{\partial z}\right) \qquad (5.13)$$

This theory is valid only above the roughness height whereas the heat-balance equation is applied at the interface between the atmosphere and the soil. Therefore, we need an equation relating the temperature at z_o to the temperature at the ground level. There are many possible equations depending mainly on the nature of the roughness elements. The most common assumption is to assume an isothermal layer from the earth's surface up to z_o. This has the advantage of simplicity and is a justifiable assumption in the case of small roughness elements. However, in the case of large roughness elements like a forest or a city such an assumption is certainly not realistic for that layer of air. In the case of a thick forest we can expect that the maximum temperature will be reached at about the level of the average height of the trees. In that case the effective surface where the radiation balance should be used would not be at the ground but at the height where the vegetation absorbs most of the incoming solar radiation. Therefore, we can expect that the modelling of the layer between the roughness height and the earth's surface will depend mainly on the physical situation to be modelled.

Consider an extreme case in which the assumption of constant heat flux would be valid down to the ground. This could be the case for a relatively rigid, tall and sparse grass through which the air could circulate easily and which has a relatively high roughness height. In this case we can apply (5.13) in the layer below z_o. We average (5.13) over the layer between z_o and the ground and obtain,

$$H = \overline{K_t} \frac{\overline{\partial \Theta}}{\partial z} \qquad (5.14)$$

In a finite-difference form this is expressed as,

$$\Theta(z_o) = \Theta(z=0) + z_o \frac{H}{K_t} \qquad (5.15)$$

The coefficient of eddy diffusivity for temperature K_t varies linearly near the roughness height so that a good average for K_t over the layer is,

$$\overline{K_t} = \tfrac{1}{2}\left[K_t(z_o) + K_t(0)\right] = (K_t)_{mol} + \frac{k_o z_o}{2 P_{rt}} \qquad (5.16)$$

where, $(K_t)_{mol}$ = molecular diffusivity = 0.18 cm^2/sec.

In general we can neglect the molecular diffusivity with respect to the turbulent diffusivity, in which case (5.15) can be rewritten as,

$$\Theta(z_o) = \Theta(z=0) + \frac{2 P_{rt}}{k_o} H \qquad (5.17)$$

We can generalize (5.17). H is computed near the roughness height and is an interesting variable to keep in the formula as well as the ground temperature and therefore the following can be used,

$$\Theta(z_o) = \Theta(z=0) + B\,H \qquad (5.18)$$

Some special cases of this formula are,

$B = 0$ implies an isothermal layer between z_o and the ground.

$B = \frac{2 P_{r_t}}{k_o}$ implies a constant heat-flux layer between z_o and the ground.

$B < 0$ implies that the temperature gradient in the layer between z_o and the ground has a different value from the temperature gradient in the layer above z_o. This could be the case, for example, for a dense forest.

5.3 Sensible Heat Flux from the Soil.

The sensible heat flux from the soil is simply,

$$S = \lim_{z \to 0} \left(K_s \frac{\partial T_s}{\partial z_s} \right) \qquad (5.19)$$

5.4 Latent Heat Flux from the Atmosphere.

The latent heat flux from the atmosphere is,

$$E = \lim_{z \to z_o} \left(K_w \frac{\partial Q}{\partial z} \right) \qquad (5.20)$$

5.5 Artificial Heat Generation.

Artificial heat generation is likely to be more important during the winter months than during the summer months. In fact, during the summertime we would expect that the man-generated heat would be insignificant when compared to the high solar energy input. All of the numerical simulations will be done for summertime situations in which artificial heat is neglected completely.

5.6 Solution of the Surface Temperature Equation.

We now have a mathematical expression for each of the terms in (5.1) and the unknown variable is surface temperature. The next

step is to write down these expressions in finite-difference form. The resulting fourth-degree equation is then solved exactly yielding directly the surface temperature. The numerical solution is described in detail in Appendix E.

CHAPTER VI

NUMERICAL SIMULATION OF THE URBAN HEAT ISLAND

6.1 Steady-State Model.

The steady-state model is used mainly to provide initial conditions for the time-dependent model. Therefore, we do not require a great accuracy in the numerical results because that does not affect greatly the time-dependent model. This implies that we must be careful in our interpretation of small differences between two steady-state simulations. Three situations were simulated:

a) small roughness height (1cm) and moderate geostrophic wind (10 m/sec).

b) Small roughness height (1 cm) and strong geostrophic wind (20 m/sec).

c) Large roughness height (100 cm) and moderate geostophic wind (10 m/sec).

From these three cases we should be able to assess the effects of the geostrophic wind speed and of the roughness height.

6.1.1 Effect of the Geostrophic Wind Speed.

Fig. 6 represents the wind hodographs for the three cases. The hodographs for moderate and strong geostrophic winds are virtually on the same normalized curve. The main difference is the height at which the relationship between U and V is realized. Table 3 shows more clearly the effect of the increased wind speed. We define arbitrarily the constant-stress layer as the layer close to the ground in which the stress does not vary by more than 20%. The constant-stress layer doubles approximately with a geostrophic wind twice as strong to reach a thickness

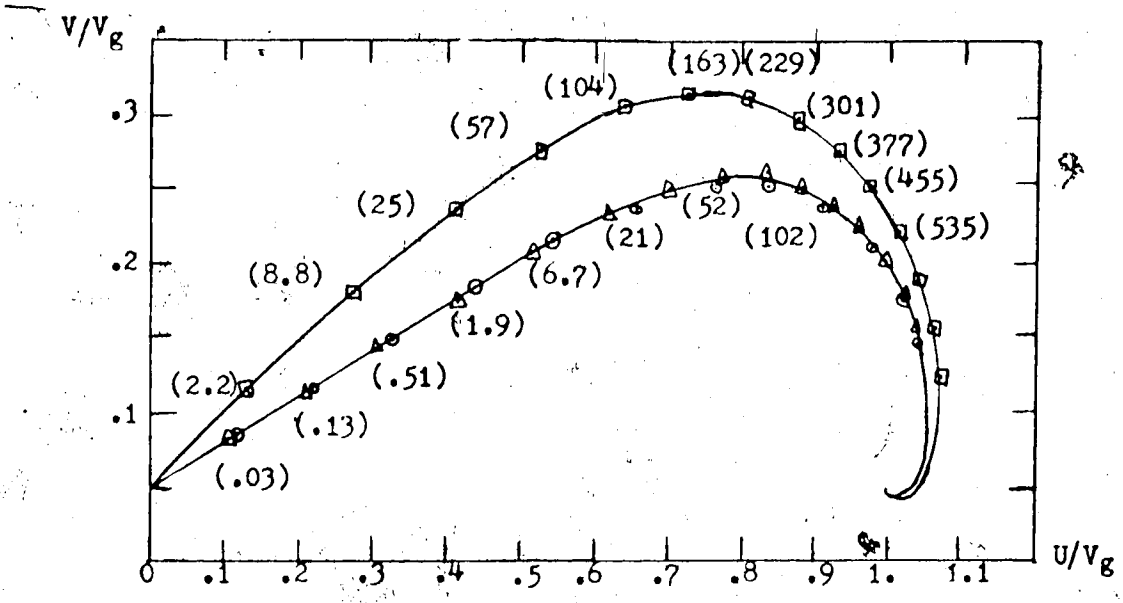

Figure 6. Normalized wind hodograph. The various symbols are:

⊙ for the case V_g = 10 m/sec, z_o = 1 cm,

△ for the case V_g = 20 m/sec, z_o = 1 cm and,

⊡ for the case V_g = 10 m/sec, z_o = 100 cm.

The number inside the parentheses is the height in meters.

Table 3. Comparison between three steady-state simulations.

case / parameter	#1	#2	#3
z_o	1 cm	1 cm	100 cm
V_g	10 m/sec	20 m/sec	10 m/sec
α	17.34°	17.53°	26.14°
max U/V_g	1.0477	1.0504	1.0630
max V/V_g	0.205	0.210	0.264
u_*	30.19 m/sec	56.76 m/sec	45.26 m/sec
Top of c.-s. layer	120 m	240 m	180 m

of 240 m. The roughness angle α is comparable in both cases. Greater accuracy in the numerical results would have been needed in order to assess with certainty the effect of the increased geostrophic wind on α. From Estoque's (1973) numerical model we would have expected a decrease of 1° in α due to the doubling of the geostrophic wind and not an increase of 0.2° as obtained in our numerical simulation. The maximum normalized values for both U and V are larger by about 1% for the case of strong geostrophic wind.

In Fig. 7 we compare the behavior of e^2/u_*^2 for all the situations. We observe that the turbulent energy is nearly constant in the constant stress-layer as indicated by the lower straight line, but decreases rather rapidly above that layer for the case of moderate geostrophic wind and much more slowly for the case of strong geostrophic wind. Fig. 8 gives the vertical profile of $K_m/k_o u_*$. The lower boundary value is z_o. In the constant-stress layer we have a linear relationship between K_m and z as indicated by the lower straight line in the nearly log-log graph. The vertical axis in Figs. 7 and 8 is the φ-coordinate expressed in terms of ordinary heights; therefore, it is logarithmic in the lowest part and nearly linear in the upper part. Both Figs. 7 and 8 indicate that the turbulence will be greatly increased above the constant-flux layer in the case of strong geostrophic wind. This causes a substantial increase in the boundary-layer depth which exceeds 1900 m for the strong wind case as compared to 1300 m for the moderate wind case.

6.1.2 Effect of Increased Roughness Height.

In Fig. 6 we observe that the rougher terrain causes an

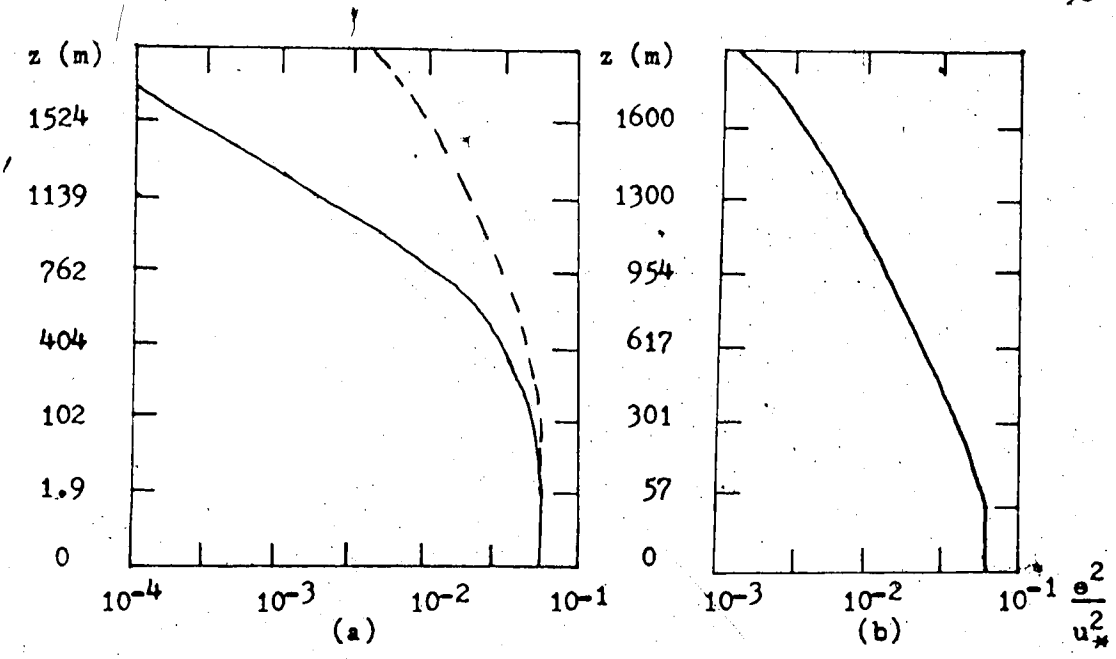

Figure 7. Vertical variation of e^2/u_*^2 : a) over z_o=1 cm. Solid line: V_g=10 m/sec. Dotted line: V_g=20m/sec. b) Over z_o=100 cm.

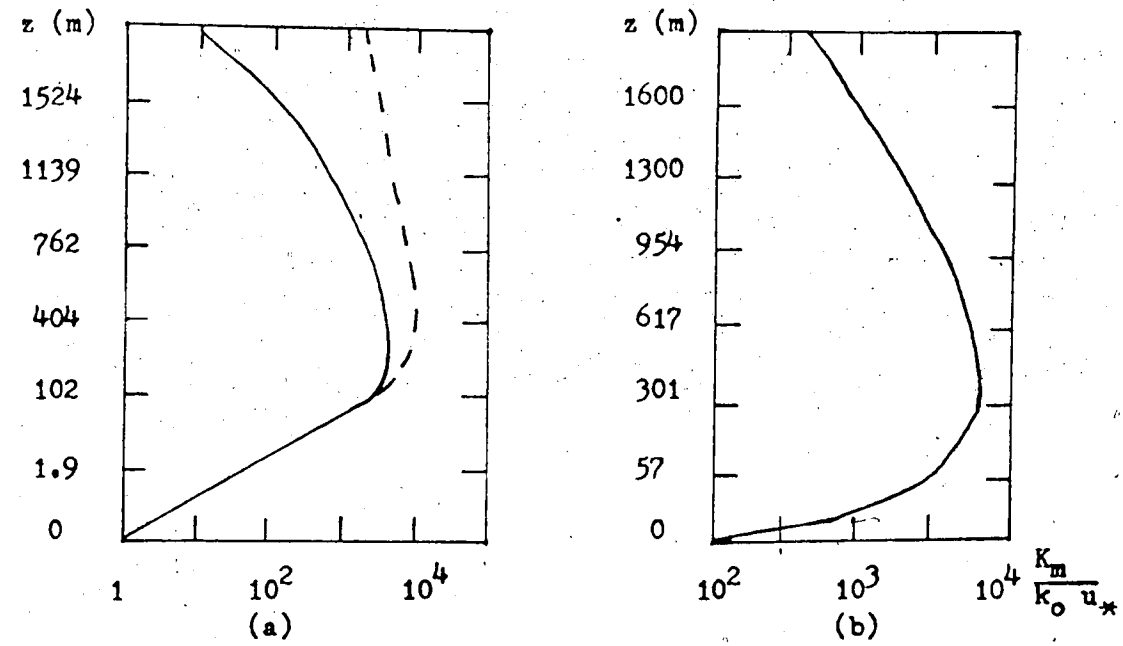

Figure 8. Vertical variation of $K_m/k_o u_*$: a) Over z_o=1 cm. Dotted line for V_g=20 m/sec and solid line for V_g=10 m/sec. b) Over z_o=100 cm.

increase in the roughness angle as expected from theoretical considerations. The increase of 8.5° for a change in roughness height of 2 orders of magnitude agrees very well with Estoque's (1973) Fig. 6.4. From Table 3 we can see that the maximum values for U and V are, respectively, 1.5% and 30% larger over rougher terrain. The top of the constant-stress layer is increased by about 50% by a change in roughness height of two orders of magnitude. The friction velocity u_* is also increased by 50%. This is an interesting result because Table 3 seems to indicate a linear relationship between u_* and the top of the constant-stress layer under neutral conditions. However, such a relationship would need to be investigated over a wider range of roughness heights and of geostrophic wind speeds. From the knowledge of u_* we could estimate the height of the constant-stress layer by a formula like:

$$\text{Top of c.-s. layer} = 400\ u_*$$

From Figs. 7 and 8 we deduce that both e^2 and K_m are increased by an increase in z_o. Again, the increase in the turbulence is greater above the constant-stress layer than below it. This increases the depth of the boundary layer by at least 50%.

6.2 Time-Dependent Model.

The time-dependent model was run with the second form of the equations for the mean quantities. The model ran smoothly with OMEGA = 0.7. We have supposed that convergence was reached whenever the differences between two successsive iterative values for the diffusivity coefficients were all smaller than 10 cm^2/sec. In the constant-stress layer, this generally insures an accuracy of 0.1 m/sec in

the mean winds and of 0.001°C in Ⓗ. Above the constant-stress layer the accuracy is generally greater because the variables are varying more slowly with respect to time. The model is started at the time of maximum temperature which occurs near 2 PM. The parameters common to all simulations are:

$\delta = 23°$ (summer solstice)

$\varphi = 53°$ (Edmonton's latitude)

$T_r = 0.85$

$\varepsilon_1 = 0.82$

albedo = 0.25

$P(z_o) = 940$ mb (altitude near 2200 feet)

$Q = 0.006$ g/g

Four simulations were made:

a) Moderate wind, small roughness height and high soil conductivity.

b) Strong wind, small roughness height and high soil conductivity.

c) Moderate wind, large roughness height and high soil conductivity.

d) Moderate wind, small roughness height and low soil conductivity.

Table 4 lists the differences in the external parameters for the four cases under study. From these four simulations we should be able to assess the effect of the geostrophic wind speed, the effect of the roughness height and the effect of the soil conductivity. Using simulation a) as a reference, we will compare U, V, Ⓗ, K_t and $\overline{w\theta}$ for the three other cases. Then, we will examine the diurnal cycle of the other turbulent quantities using model b). Model b) is chosen in this case because its diurnal cycle is smoother than the others due to the increased turbulence caused by the stronger geostrophic wind.

Table 4. Parameters for the time-dependent simulations.

parameter \ model #	1	2	3	4
z_0 [cm]	1	1	100	1
V_g [m/sec]	10	20	10	10
ρ_s [g/cm^3]	2.6	2.6	2.6	1.8
k_s [cm^2/sec]	0.021	0.021	0.021	0.0053
c_s [ergs/(g- ^oC)]	1.25×10^7	1.25×10^7	1.25×10^7	8.3×10^6
$\rho_s k_s c_s$ [ergs/(cm-sec- ^oC)]	4.53×10^5	4.53×10^5	4.53×10^5	1.19×10^5

6.2.1 Geostrophic Wind Speed.

Fig. 9 shows the diurnal variation of the surface temperature. The increased geostrophic wind reduces the amplitude of the diurnal cycle; the minimum temperature is increased by 2.92 °C and the second-day maximum temperature is decreased by 1.71 °C. There is no detectable time lag between the two temperature cycles and they both reach their minimum near 4.30 AM and their maximum near 2.30 PM. The surface cooling rate illustrated in Fig. 10 also shows the moderating effect of the stronger wind. Stronger winds increase the mixing which allows a deeper layer to cool down or warm up, thus decreasing the amplitude of the diurnal temperature cycle. We see in Fig.11 that the amplitude of the diurnal variation of the roughness angle is also reduced by the stronger wind. The shape of both curves is similar. We observe a rapid decrease in α during the first 6 hours after the time of maximum temperature. However, the surface cooling rate has reached its maximum intensity near 6 PM and is decreasing rapidly between 6 PM and 8 PM. This reduces the growth rate of α which reaches a secondary maximum near 7 to 8 PM. α decreases after the decrease in the cooling rate because the level of maximum cooling rate shifts higher, destabilizing slightly the layer close to the ground. However, after a while a deep layer above the ground becomes so stable as to permit a continuous increase in α, which is observed between 11 PM and 6 AM. After 8 AM α exhibits a tendency to decrease. However, we observe a large oscillation with minimum near 9 AM and maximum near 11 AM. This is similar to the overnight maximum in α. The maximum warming rate occurs near 9 AM. Due to enhanced turbulence under unstable conditions, the slight decrease in the warming rate after 9 AM is

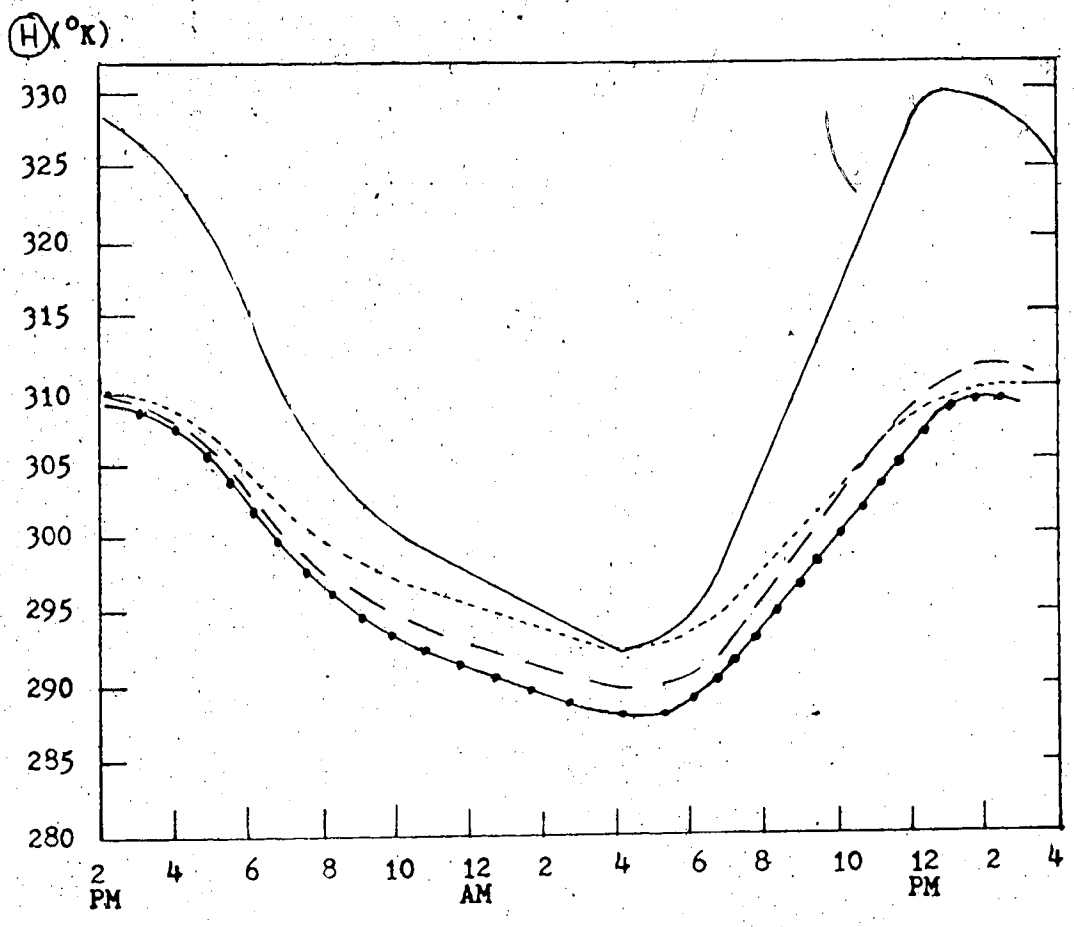

Figure 9. Diurnal cycle of the surface potential temperature. The different curves represent the following:

— z_o=1 cm, V_g = 10 m/sec, soil thermal conductivity= low.

—●— z_o= 100 cm, V_g = 10 m/sec, soil thermal conductivity = high.

– – z_o= 1 cm, V_g = 10 m/sec, soil thermal conductivity = high.

····· z_o= 1 cm, V_g = 20 m/sec, soil thermal conductivity = high.

The hour in this and the subsequent graphs is expressed in solar time related to the mountain standard time by: LST = MST-0.6. Sunrise occurs at $3\frac{40}{}$ AM LST and sunset at $8\frac{20}{}$ PM LST.

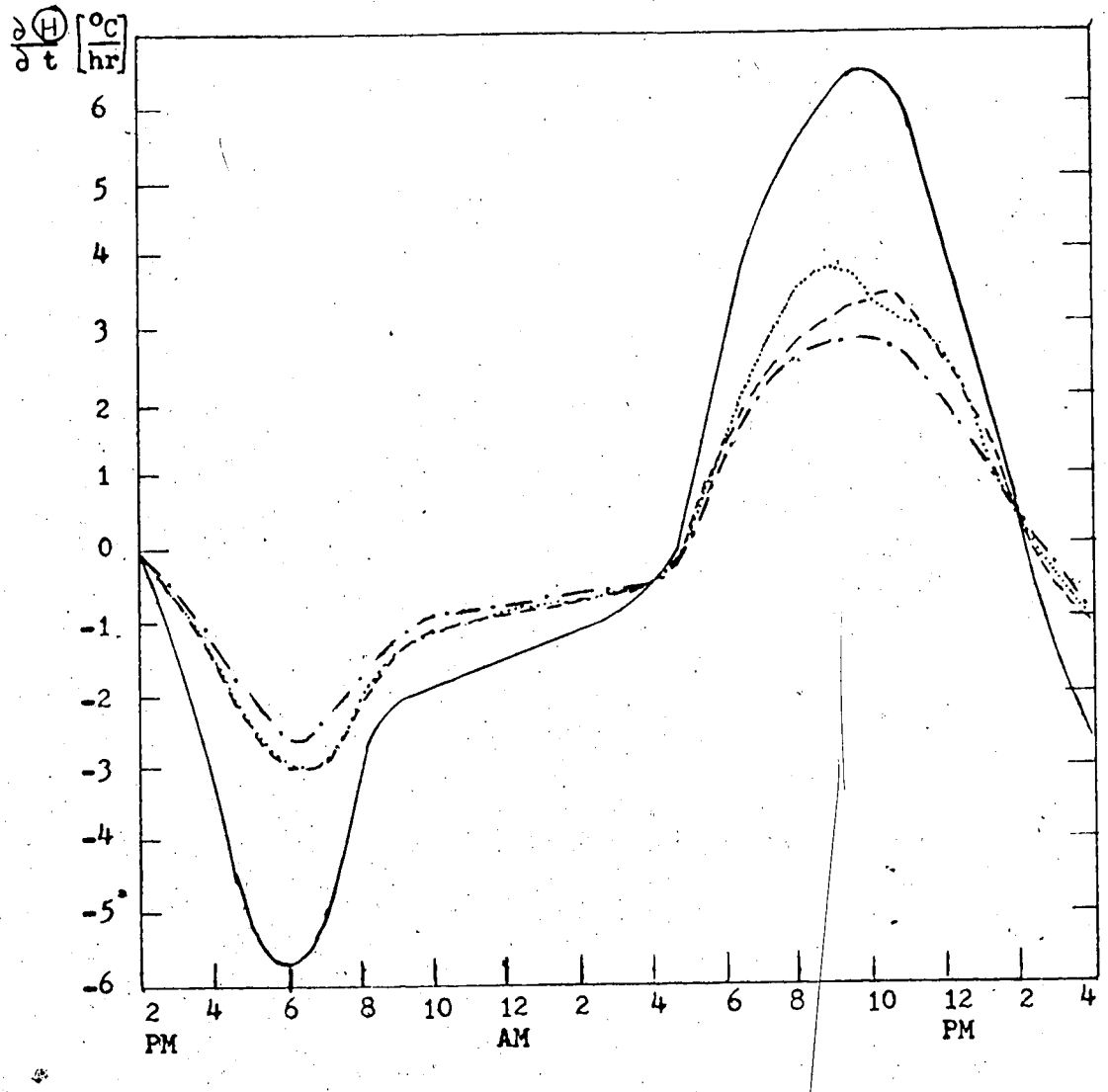

Figure 10. Warming rate at the surface. The four curves represent:

— z_o=1 cm, V_g = 10 m/sec, soil thermal conductivity = low.

..... z_o= 100 cm, V_g = 10 m/sec, soil thermal conductivity = high.

-- z_o= 1 cm, V_g = 10 m/sec, soil thermal conductivity = high.

—·— z_o= 1 cm, V_g = 20 m/sec, soil thermal conductivity = high.

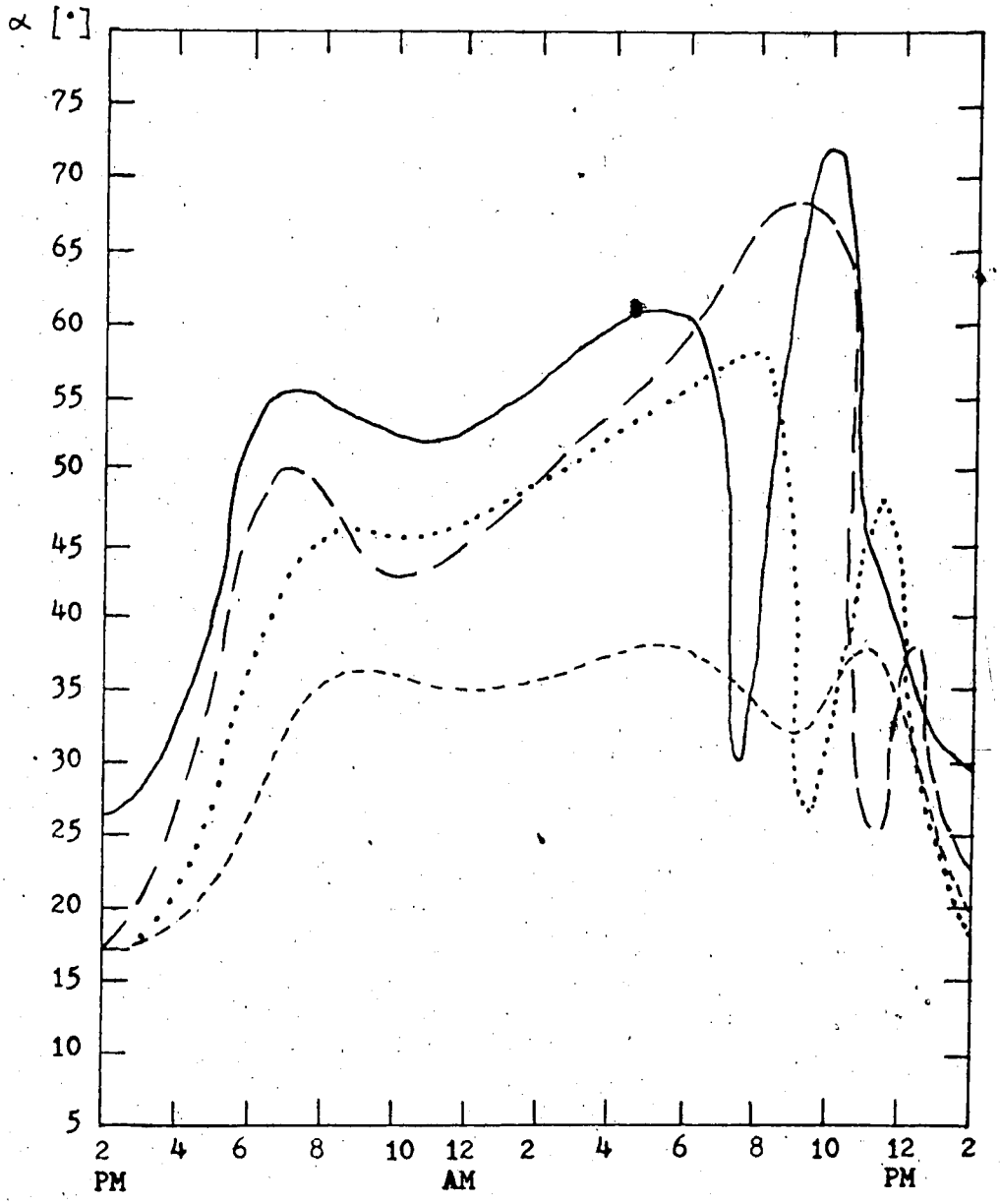

Figure 11. Diurnal variation of the roughness angle. The various curves are:

— — z_o= 1 cm, V_g = 10 m/sec, soil thermal conductivity = low.

— z_o= 100 cm, V_g = 10 m/sec, soil thermal conductivity = high.

···· z_o= 1 cm, V_g = 10 m/sec, soil thermal conductivity = high.

---- z_o= 1 cm, V_g = 20 m/sec, soil thermal conductivity = high.

almost immediately reflected in α which increases suddenly. The oscillation is certainly amplified by the finite grid because the inversion height is not lifted continuously but by discrete steps. Therefore, even if there are some physical reasons for the oscillation in α near 10 AM, the amplitude of the phenomenon is certainly much smaller than indicated in Fig. 11.

Figs. 12 and 13 represent the diurnal cycle of the vertical distribution of Θ for strong and moderate geostrophic winds, respectively. With moderate geostrophic winds the nocturnal cooling is only 0.03 °C at 240 m and 0.1 °C at 166 m. However, with strong geostrophic winds the overnight cooling at 166 m, 240 m and 670 m is, respectively, 12.3 °C, 6 °C and 0.1 °C. This is a reflection of the increased turbulence and deeper mixing layer. One interesting feature of the model is that it predicts a delay between the time at which the surface temperature starts increasing after sunrise and the time at which the atmosphere becomes unstable in the lowest levels. Near sunrise the atmospheric heat flux is positive and it will take some time before it changes sign. The increase in surface temperature destabilizes the lower layer which increases the turbulence and the coefficient of eddy diffusivity and therefore permits a slower decrease in the heat flux. That delay is about one hour for the moderate wind case but reaches two hours in the case of strong winds. The surface temperature warms up by 0.7 °C in the moderate-wind case and by 2.4 °C in the strong-wind case before the lower atmosphere becomes unstable. The Kansas experiments have shown an average delay of one hour between sunrise and the appearance of an unstable lapse rate at 6 m (Wyngaard; 1973). This agrees very well with our results if we

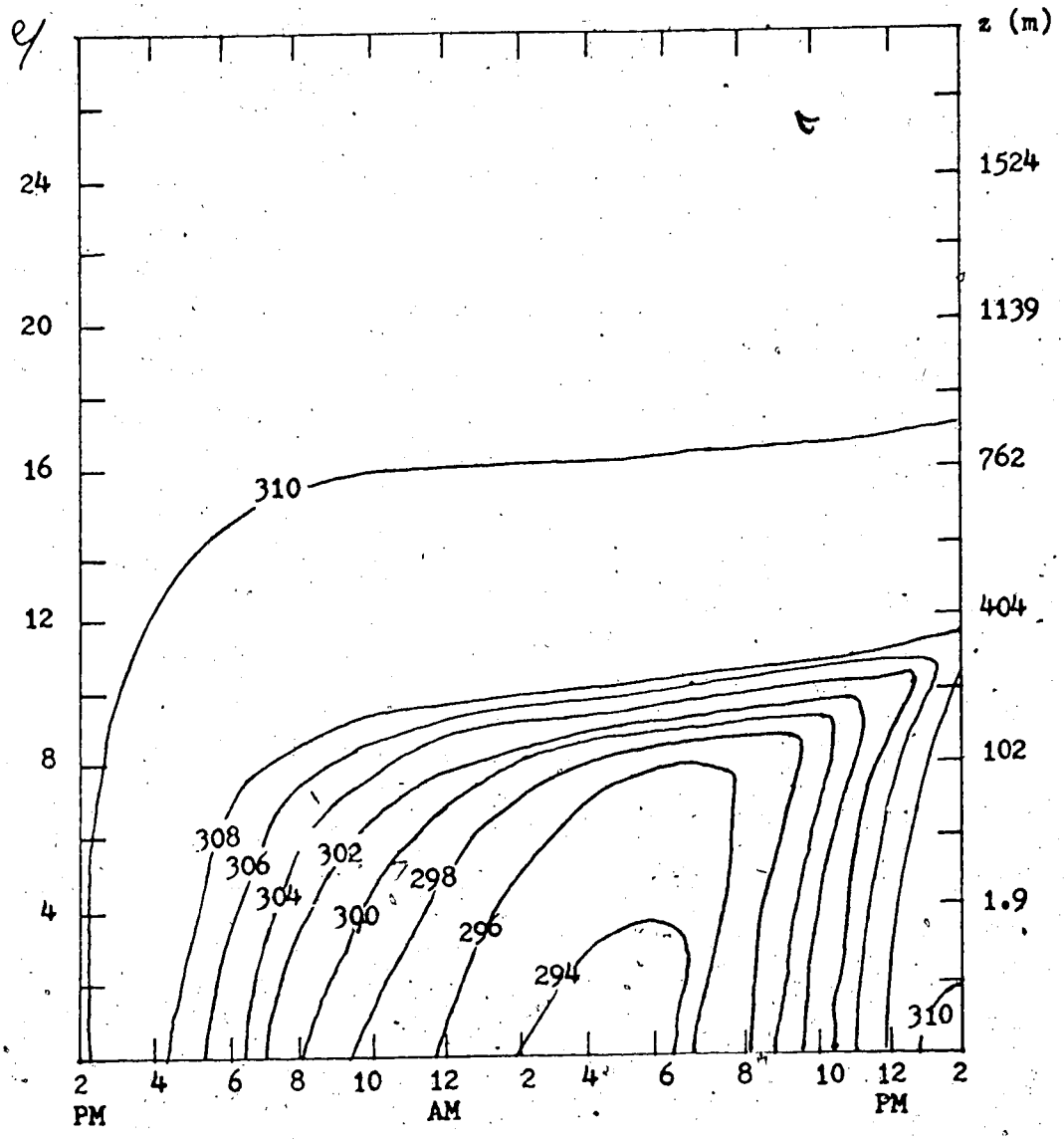

Figure 12. Diurnal cycle of the vertical distribution of potential temperature for the case z_o = 1 cm, V_g = 20 m/sec and high soil conductivity. The units are [°K].

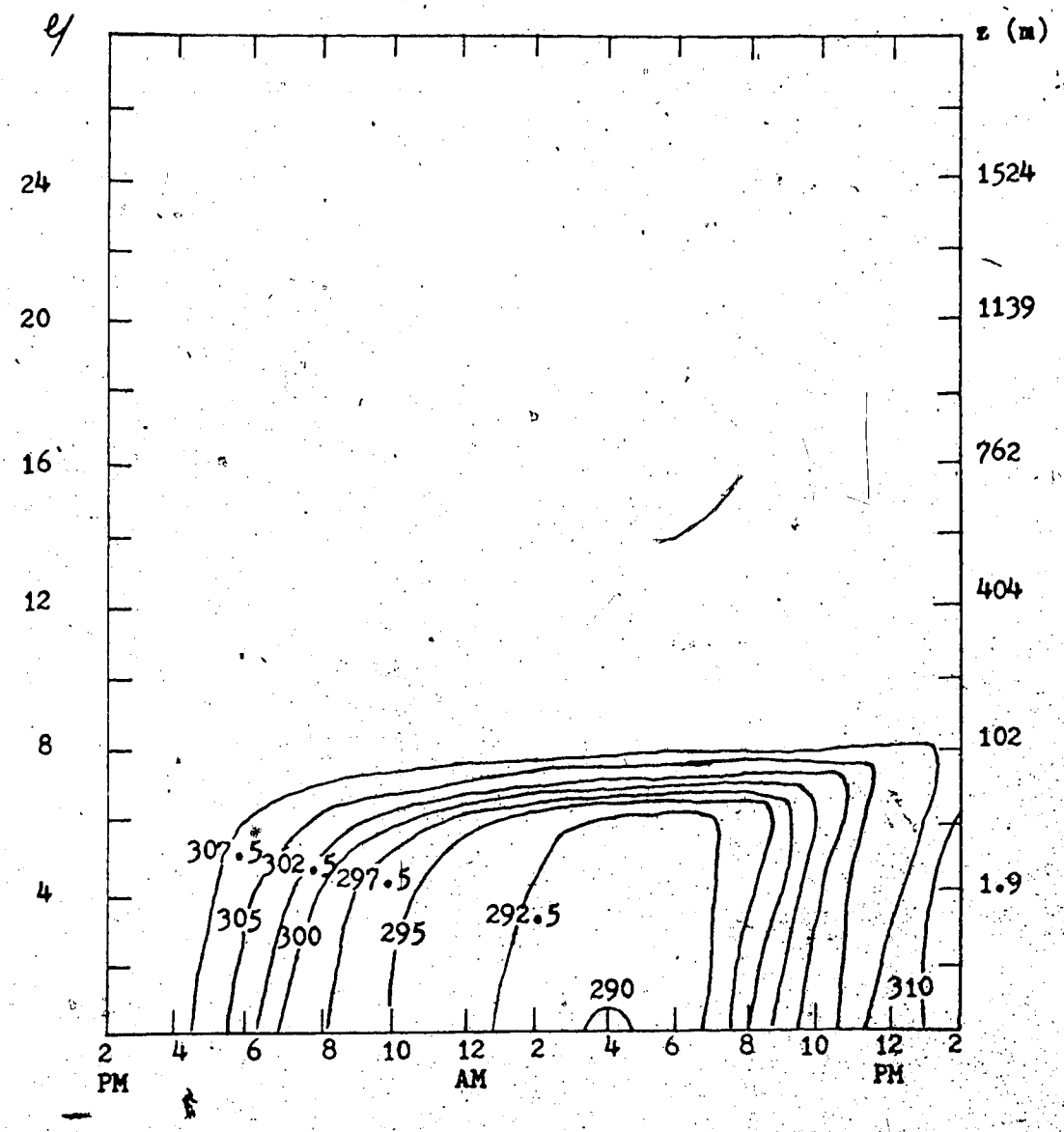

Figure 13. Diurnal cycle of the vertical distribution of potential temperature for the case z_o = 1 cm, V_g = 10 m/sec and high soil conductivity. The units are [°K].

suppose that the average geostrophic wind during these experiments was less than 10 m/sec.

The heat flux is represented in Figs. 14 and 15 for the cases of high and moderate winds. We observe that $\overline{w\theta}$ is more than doubled by doubling the geostrophic wind speed. The phase difference already noted in the surface value of $\overline{w\theta}$ between the two simulations is also apparent up to 50 m. We observe also that the inversion height is lifted more rapidly with the stronger winds after the instability has been established in the lower grid points.

By comparing Fig. 16 with Fig. 17 we can say that the maximum value for K_t is increased by a factor of 2 to 4 and that the height at which that maximum occurs is shifted upwards by about 50 m. Therefore, $\overline{w\theta}$ is larger with stronger winds, even if the temperature gradients are smaller, because of the much larger values for K_t in that case. The general shape of both curves for K_t is similar: very high values during near neutral and unstable situations and very small values everywhere overnight during stable situations. We observe also a marked difference between the first day and the second day due to the fact that the upper levels have remained stable during the 24-hour cycle which caused a decrease in K_t above 500 m. The model has a tendency to produce negative values for K_t under very stable conditions. We reset K_t automatically to a very small number of the order of 10^{-2} cm^2/sec whenever that happens. We need that restriction in order to insure the stability of the finite-difference scheme. Otherwise we would get the formation of many artificial inversions which could easily prevent the convergence of the model. This problem is more serious in the moderate wind case as 5 to 6 levels

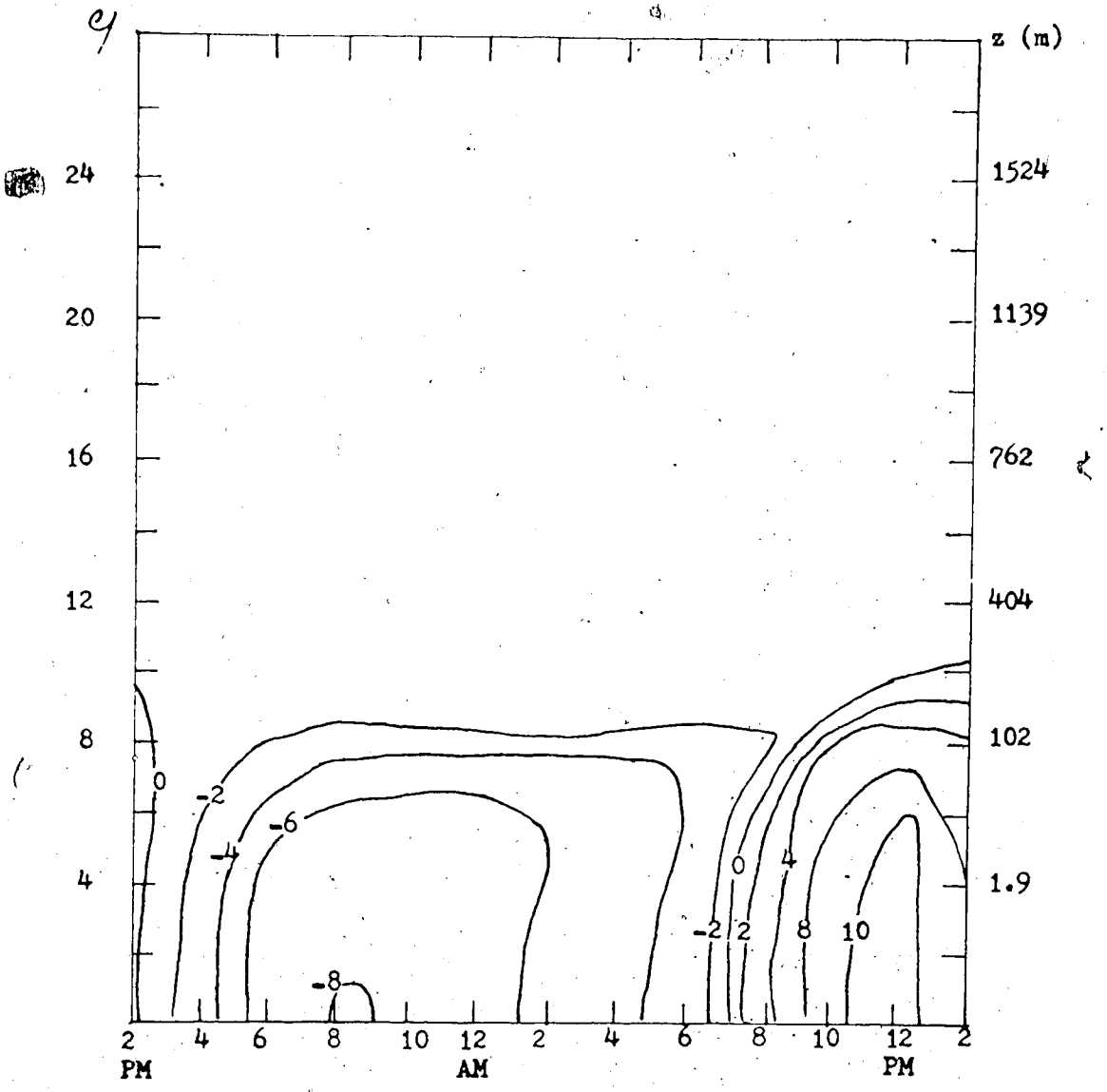

Figure 14. Diurnal cycle of the vertical distribution of $\overline{w\theta}$ for the case z_o = 1 cm, V_g = 20 m/sec and high soil conductivity. The units are [cm ^{o}C sec^{-1}].

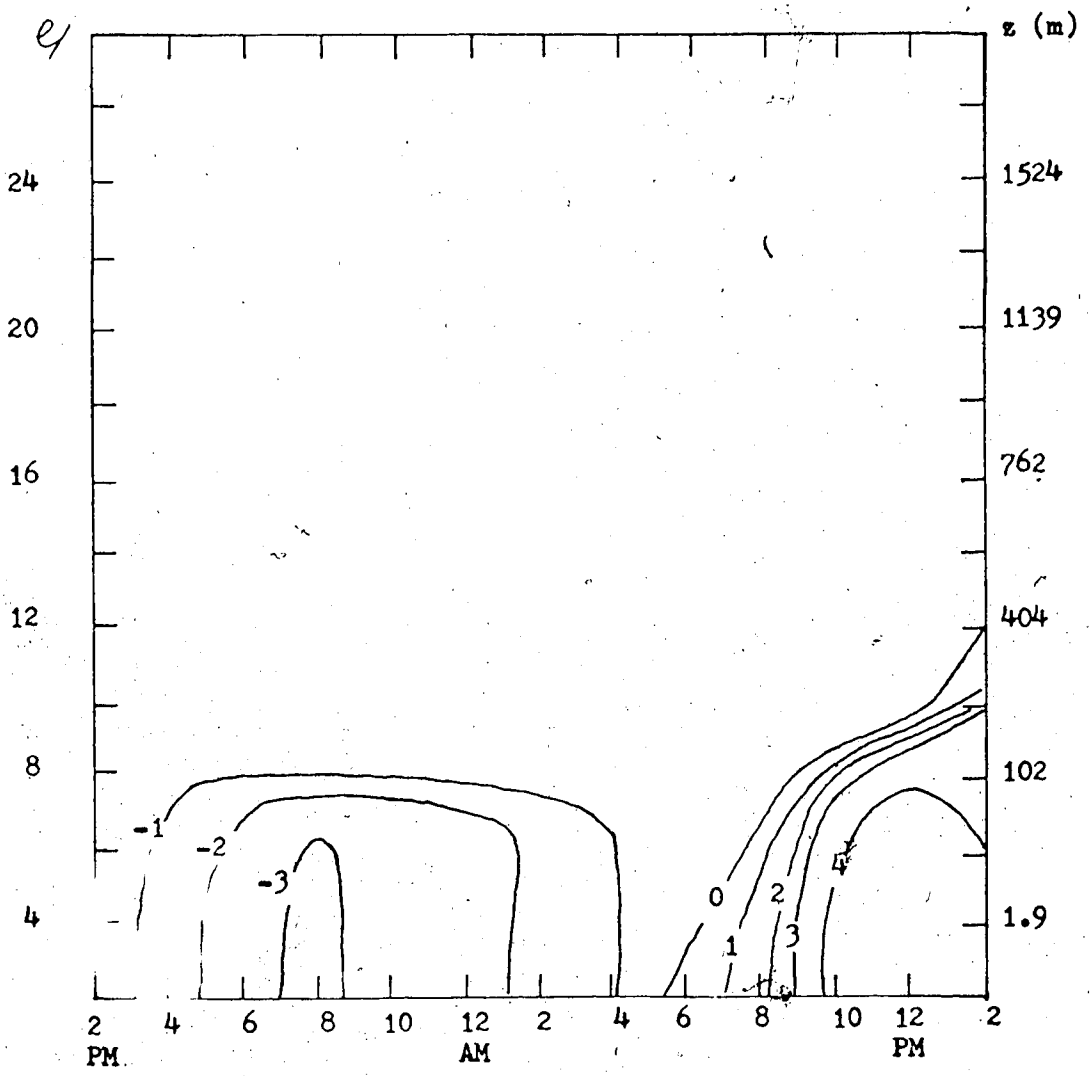

Figure 15. Diurnal cycle of the vertical distribution of $\overline{w\theta}$ for the case z_o = 1 cm, V_g = 10 m/sec and high soil conductivity. The units are $[\text{cm } ^{\circ}\text{C sec}^{-1}]$.

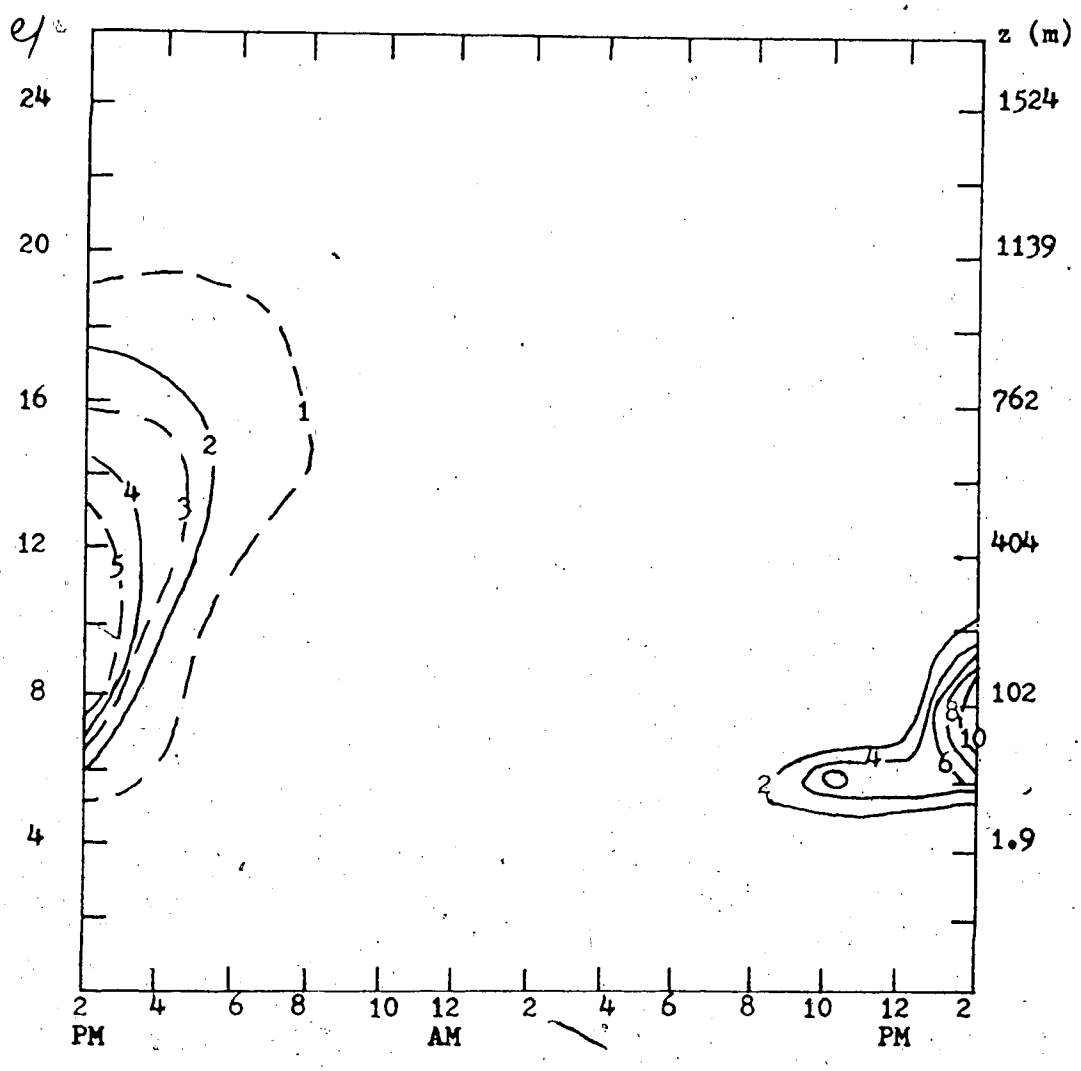

Figure 16. Diurnal cycle of the vertical distribution of the coefficient of diffusivity for temperature for the case z_o = 1 cm, V_g = 10 m/sec and high soil conductivity. The units are $[10^4$ cm^2/sec$]$.

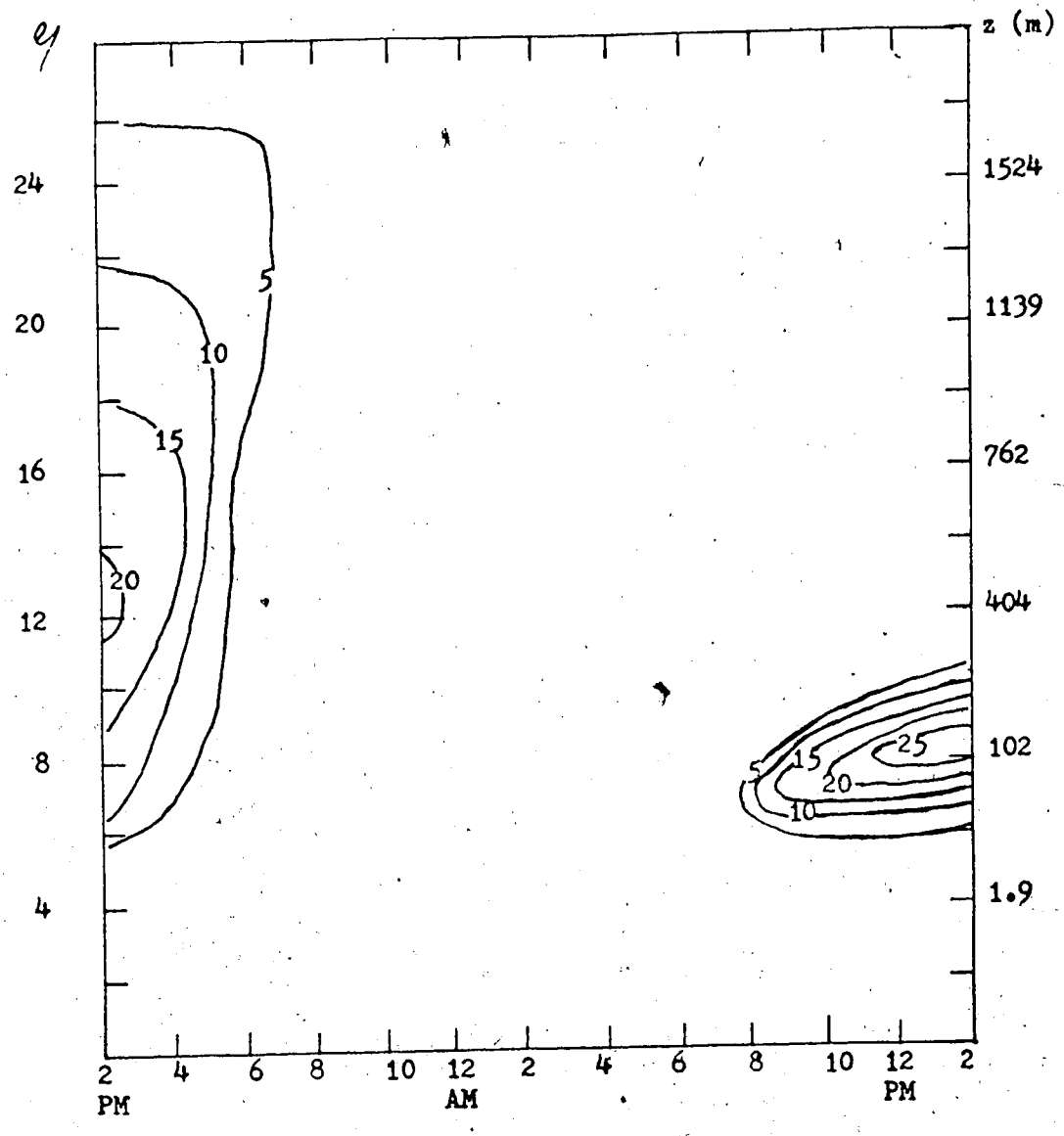

Figure 17. Diurnal cycle of the vertical distribution of the coefficient of diffusivity for temperature for the case z_o = 1 cm, V_g = 20 m/sec and high soil conductivity. The units are $[10^4$ cm^2/sec$]$.

are computed with negative values by early morning. With strong geostrophic winds only one or two levels exhibit that tendency. We feel that allowing negatives values for K_t would not change significantly the results while compromising the convergence of the iterative process. This is the justification for not allowing K_t to become negative.

Figs. 18 and 19 show the diurnal variation of U for moderate and strong winds. Both graphs are similar in shape. The maximum wind gradient is near the ground under unstable or near-neutral lapse rates. The wind gradient decreases overnight in both the upper boundary layer and the lower part of the surface layer. The region of large overnight wind gradient is concentrated between 20 m and 50 m for the moderate wind case and between 20 m and 166 m for the strong-wind case. Between about 100 m and 300 m, U has maxima near 12 PM and 12 AM and minima near 5 AM and 5 PM. The overnight maximum is caused by an inertial oscillation which takes place some time after the initial cooling when the friction force decreases above 50 m within a short period of time, from a relatively large daytime value to an extremely small value. There is a tendency for the wind to "overshoot" its geostrophic value which is caused by the non-zero time derivative term in the equations of motion. Fig. 20 illustrates the diurnal cycle of the total wind speed at different heights for the case of strong geostrophic winds. Near the ground the first minimum occurs near 8 PM, just after the time of maximum cooling rate. The decreasing cooling rate after 6 PM permits a small recovery in the surface wind speed which reaches a secondary maximum near 12 AM. The stabilization of the cooling rate after 10 PM causes a further decrease in the surface wind until sunrise. After sunrise, the surface wind increases to reach its maximum near the time

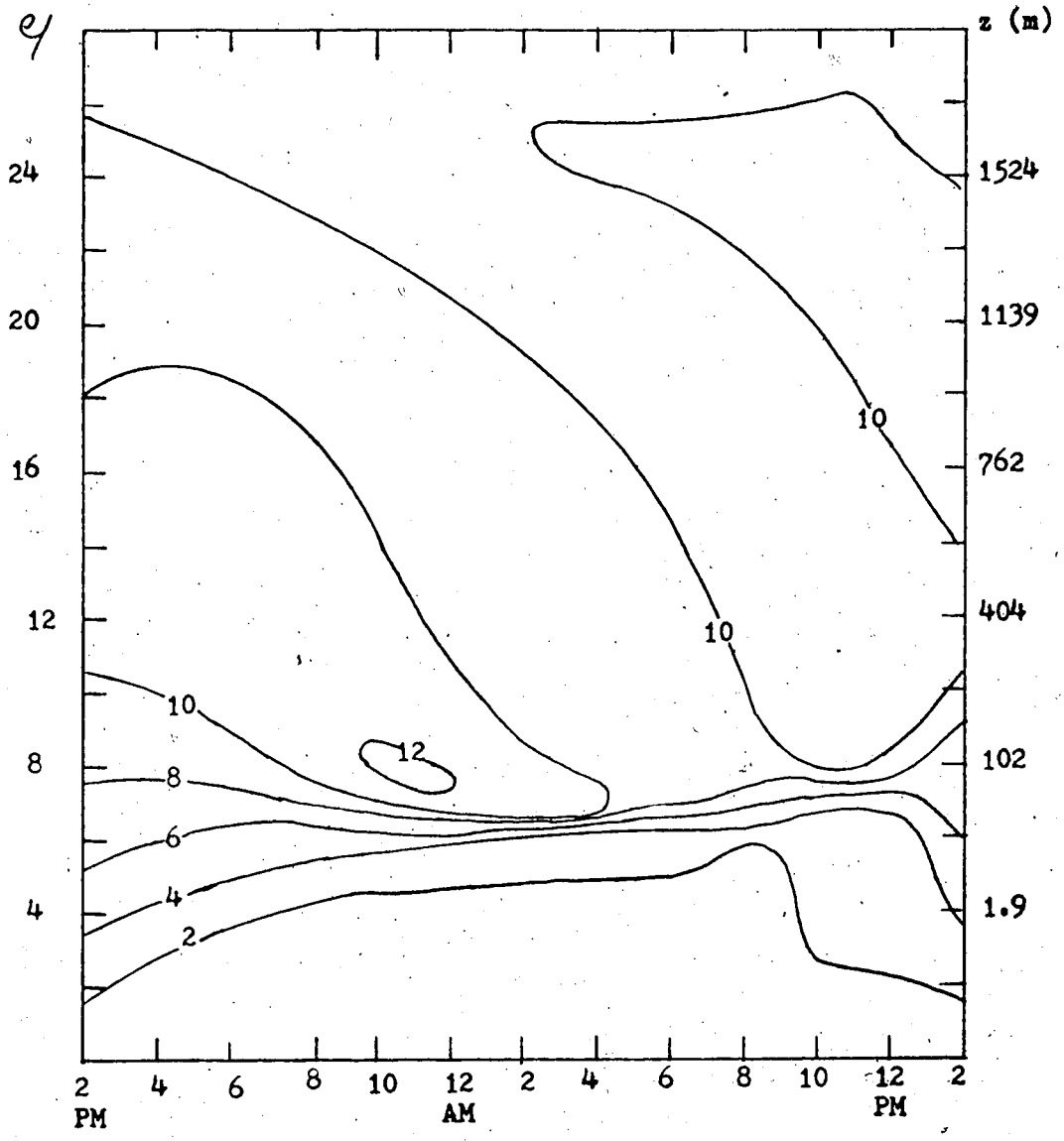

Figure 18. Diurnal cycle of the vertical distribution of U for the case of z_o = 1 cm, V_g = 10 m/sec and high soil conductivity. The units are [m/sec].

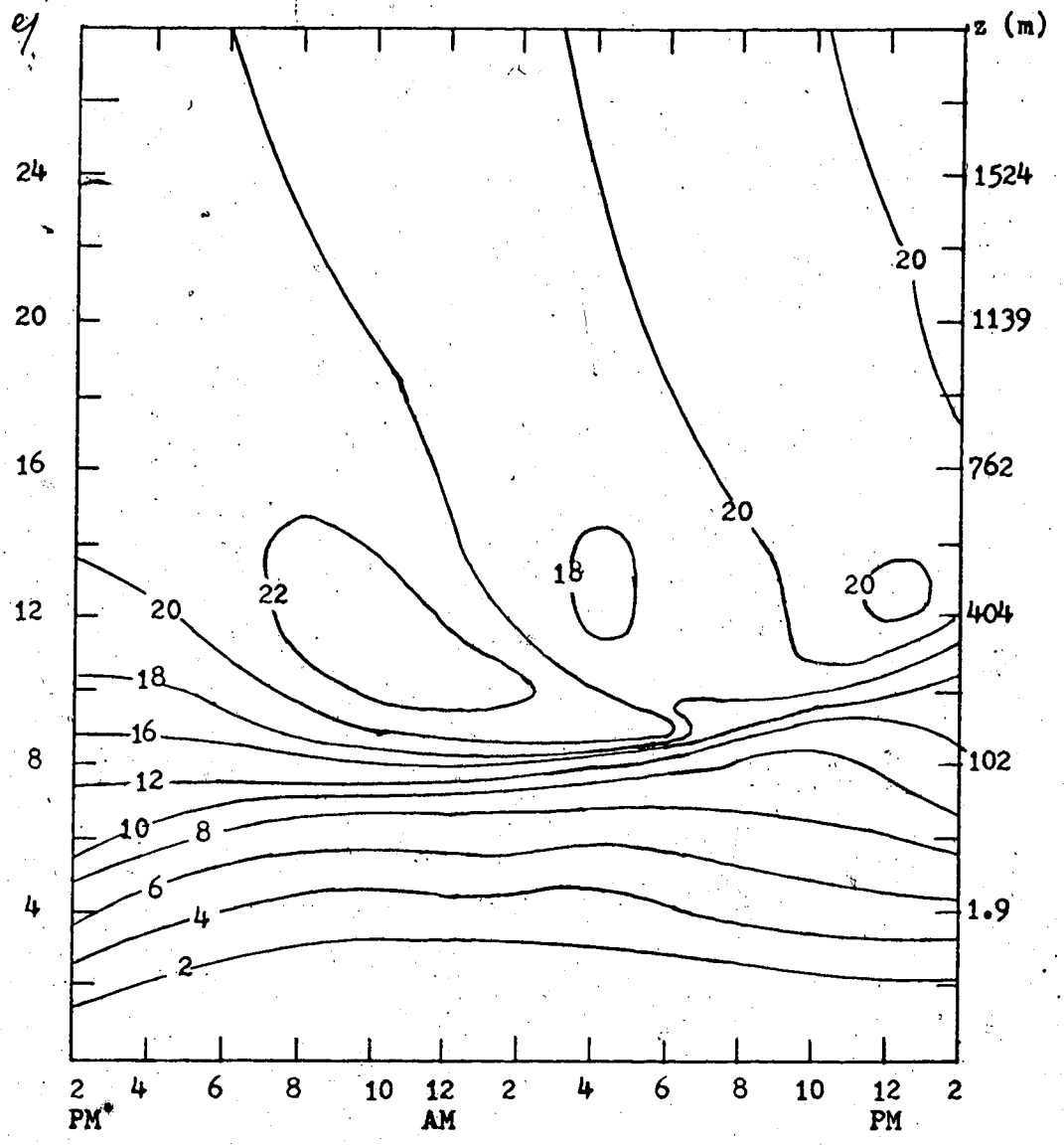

Figure 19. Diurnal cycle of the vertical distribution of U for the case z_o = 1 cm, V_g = 20 m/sec and high soil conductivity. The units are [m/sec].

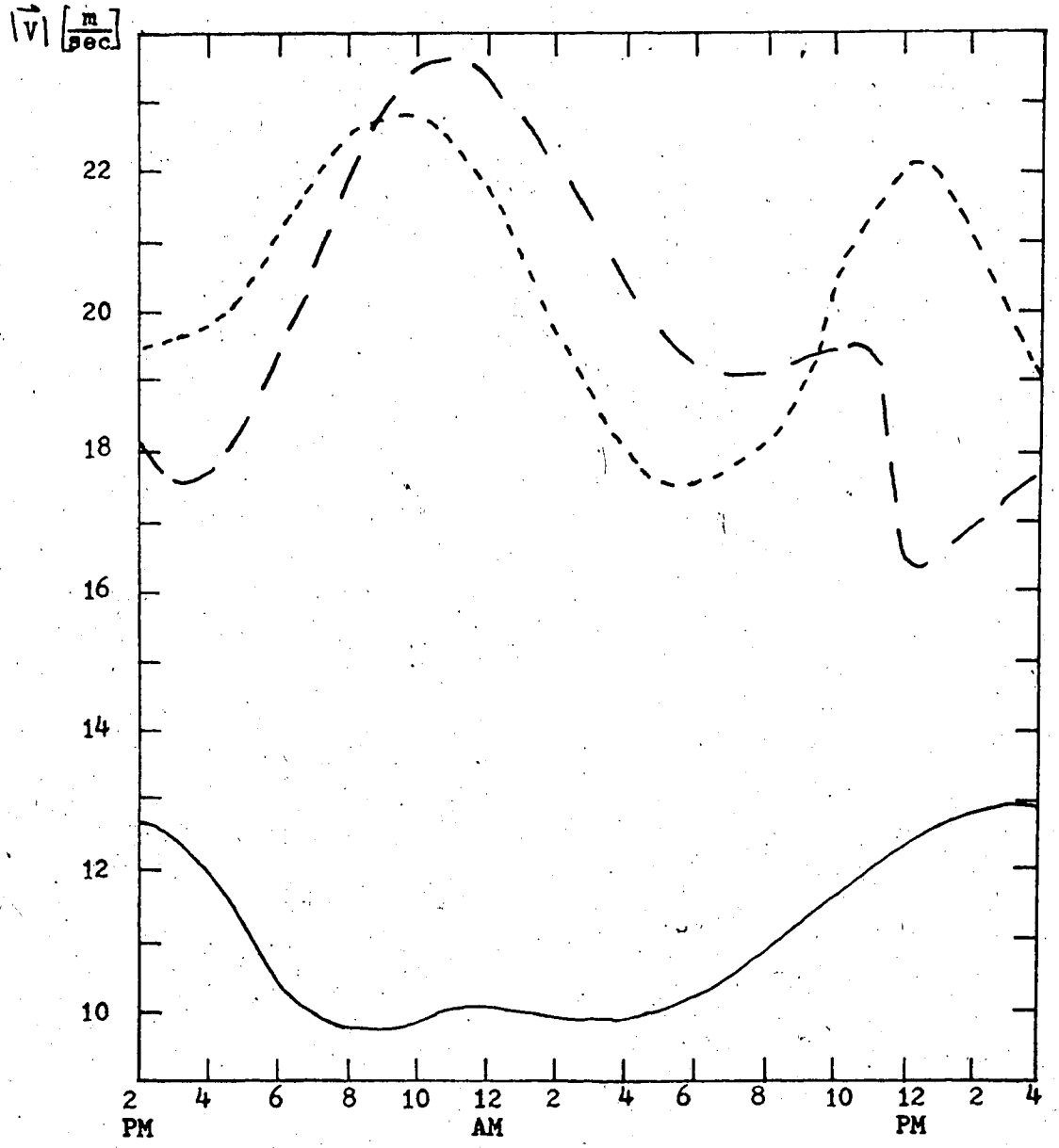

Figure 20. Diurnal cycle of the total mean wind for the case z_o = 1 cm, V_g = 20 m/sec and high soil conductivity. The various curves represent the following heights:

— φ = 6, z = 21 m

— — φ = 10, z = 240 m

----- φ = 12, z = 404 m.

of maximum temperature. With strong winds the maximum amplitude of the double-maximum-wind cycle is reached near 404 m. The overnight maximum near 12 AM is due to the inertial oscillation and the maximum near 12 PM is due to the influence of surface heating.

Figs. 21 and 22 represent the diurnal cycle of V. In the surface layer, V increases generally overnight causing an increase in the roughness angle. V reaches a secondary maximum near 8 PM in the vicinity of 40 m for moderate winds and of 80 m for strong winds. V shows also a daytime maximum near 11 AM. The region of overnight maximum gradient for V is slighly higher than the region of maximum gradient for U. Above that region, V undergoes a double cycle with maxima near 4 PM and 10 AM and negative minima near 2 AM and 2 PM. The influence of the higher wind speed is to spread out the velocity gradient over a larger region and to shift the position of the maximum winds higher in the atmosphere.

Figs. 23 and 24 represent the diurnal cycle of e. We have a rough estimate of the constant-stress layer by looking at the layer in which e does not vary by more than 20%. For the moderate-wind case, the height of the constant-stress layer is near 120 m under neutral conditions and could be as high as 400 m during unstable situations. It seems more difficult to define a constant-stress layer overnight because the stress reaches its maximum value above the ground, near 7 m. In any case, it seems that the lowest overnight constant-stress layer was around 20 m, and happened just after sunrise. The strong wind case is similar with the turbulent energy in the surface layer being twice as large during daytime and 2½ times during nighttime. The height of the constant-stress layer varies from its value of 240 m

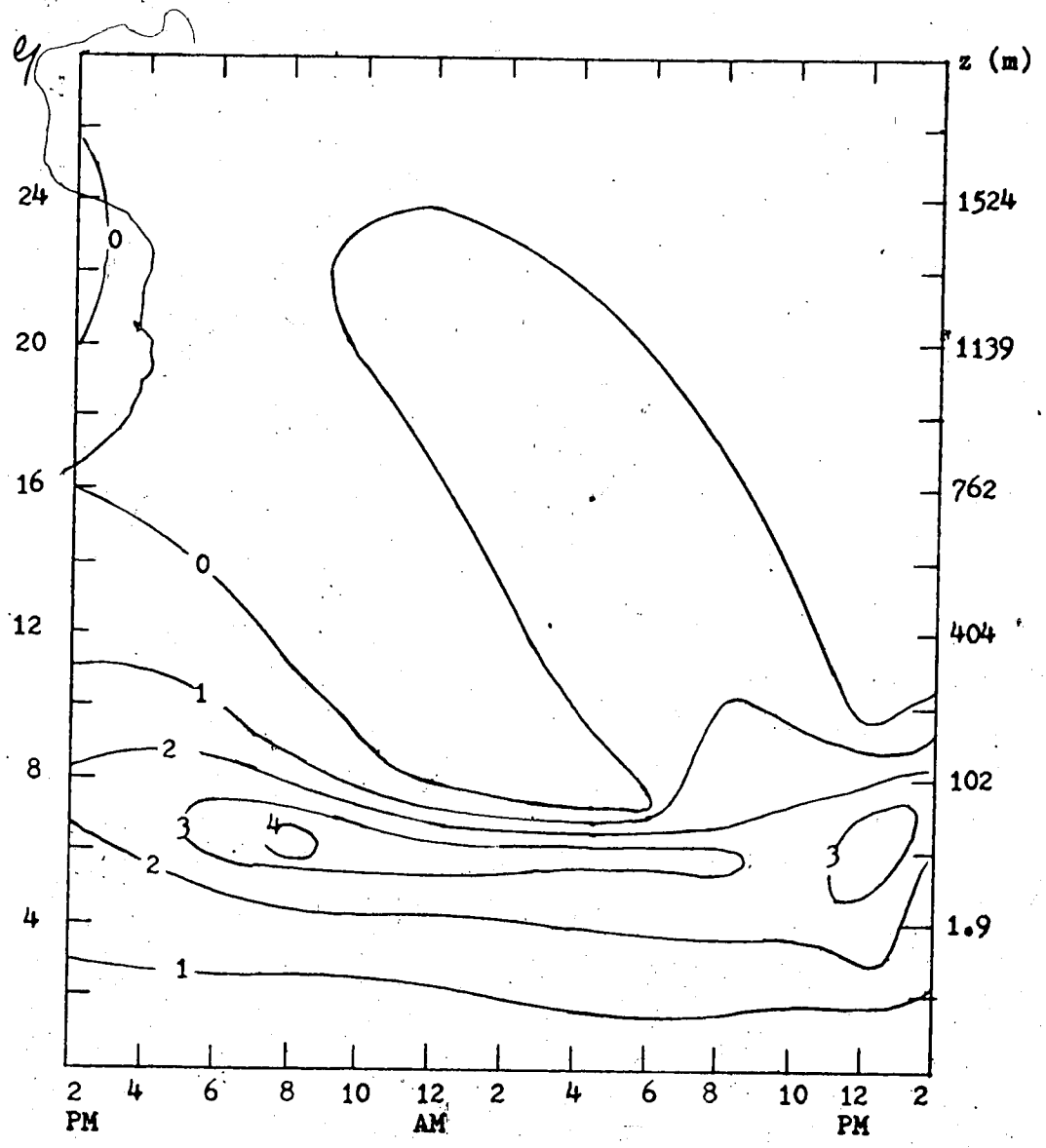

Figure 21. Diurnal cycle of the vertical profile of V for the case z_o = 1 cm, V_g = 10 m/sec and high conductivity. The units are [m/sec].

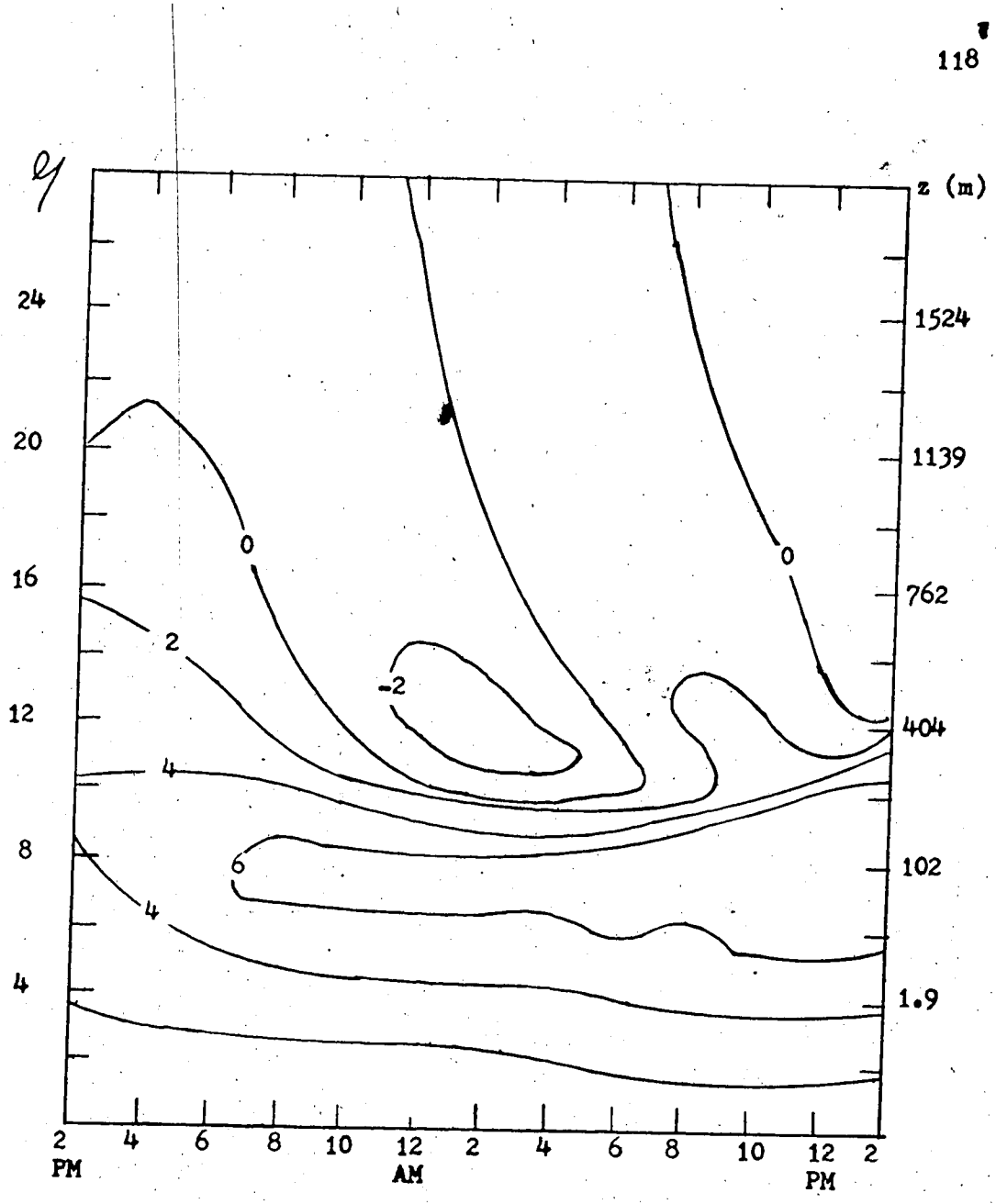

Figure 22. Diurnal variation of the vertical distribution of V for the case z_o = 1 cm, V_g = 20 m/sec and high soil conductivity. The units are [m/sec].

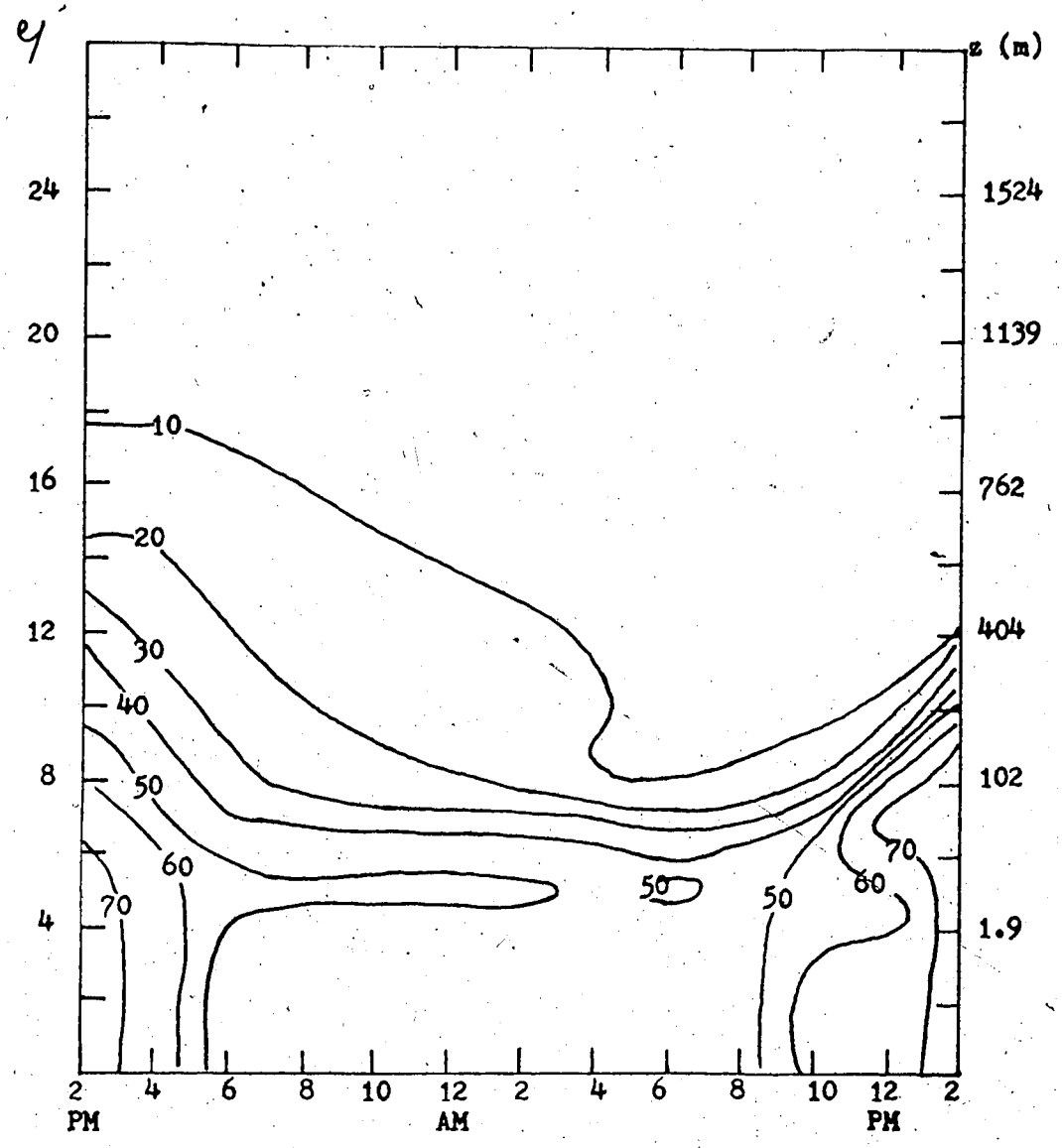

Figure 23. Diurnal variation of the vertical profile of e for the case z_o = 1 cm, V_g = 10 m/sec and high soil conductivity. The units are $[cm^2/sec^2]$.

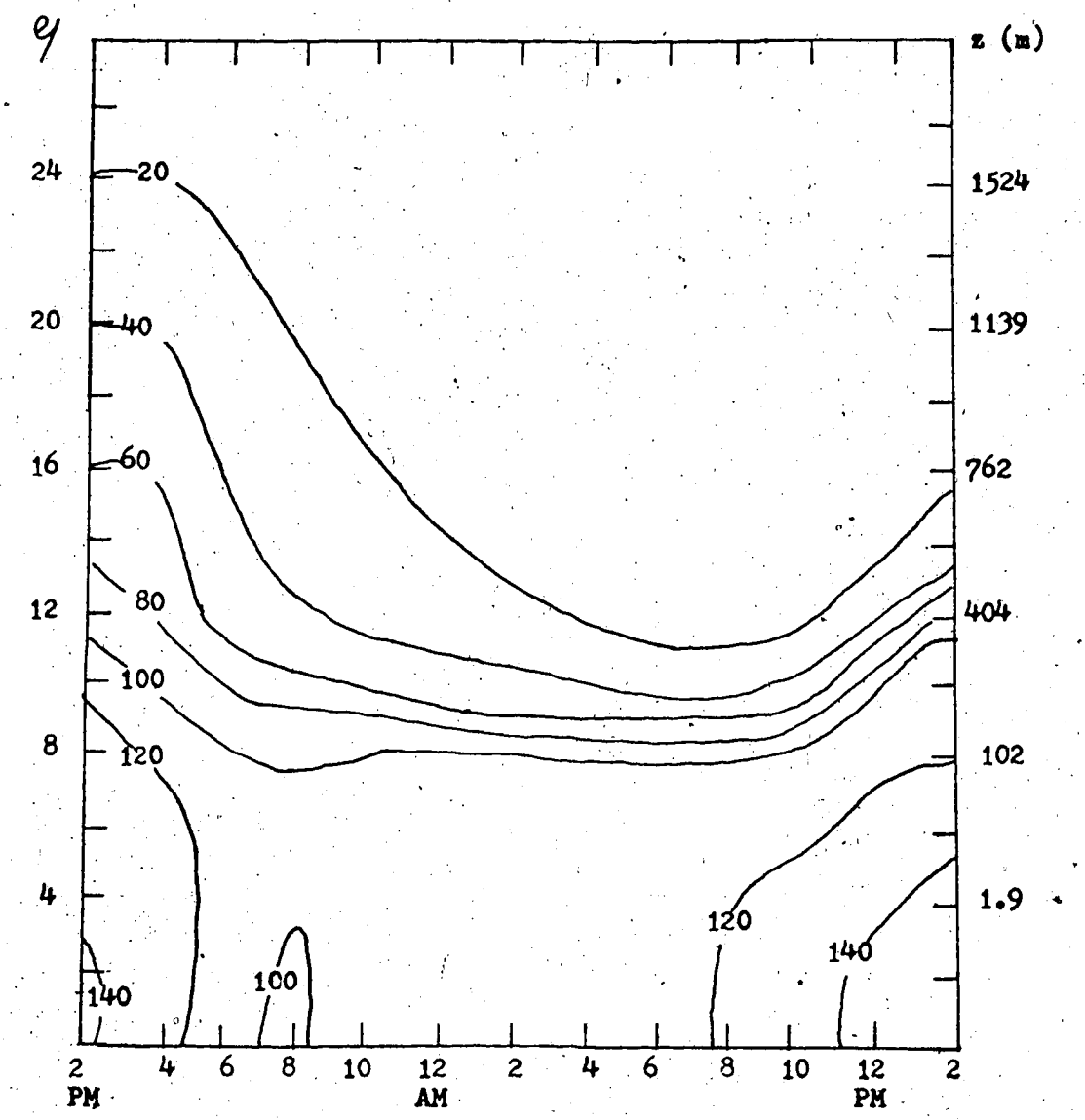

Figure 24. Diurnal cycle of the vertical distribution of e for the case z_o = 1 cm, V_g = 20 m/sec and high soil conductivity. The units are $[cm^2/sec^2]$.

under neutral conditions to above 320 m under unstable lapse rate and goes down to 120 m overnight. .The maximum daytime value of the constant-stress layer depth depends strongly on the depth of the unstable layer.

6.2.2 Effect of the Roughness Height.

We go back to Fig. 9 and note that the temperatures over rough terrain always remain lower than the temperatures over smooth terrain. The initial temperature difference is 1.4 °C, it increases to 1.8 °C by sunrise and to 2.7 °C by the time of maximum temperature. The greater cooling over the rough terrain during the nighttime is contrary to theoretical expectations because we expect that with the enhanced turbulence over the rough terrain, a deeper layer will cool down, thus increasing relatively the surface temperature. Fig. 10 shows that the cooling rates over smooth and rough terrain are almost identical until 6 AM. A more detailed analysis of the data reveals that between 2 PM and 8 PM, the air over the rough terrain cools down more slowly in agreement with the theory. However, this situation is reversed between 8 PM and 4 AM. When we compare Fig. 25 with Fig. 13, we observe that the temperature gradient in both cases accumulates between 20 and 100 m. For z_o = 1 cm, the temperature difference near sunrise between 20 m and 50 m is 10.6 °C, and between 50 m and 100 m is 7 °C. Similarly, for z_o = 100 cm, the difference is 6.5 °C between 20 m and 50 m, and 9.7 °C between 50 m and 100 m. Therefore, a deeper layer is cooling over the rough terrain as indicated by the spreading out of the temperature gradient. Now, we compare the heat fluxes in the atmosphere as represented in Figs. 15 and 26. In the

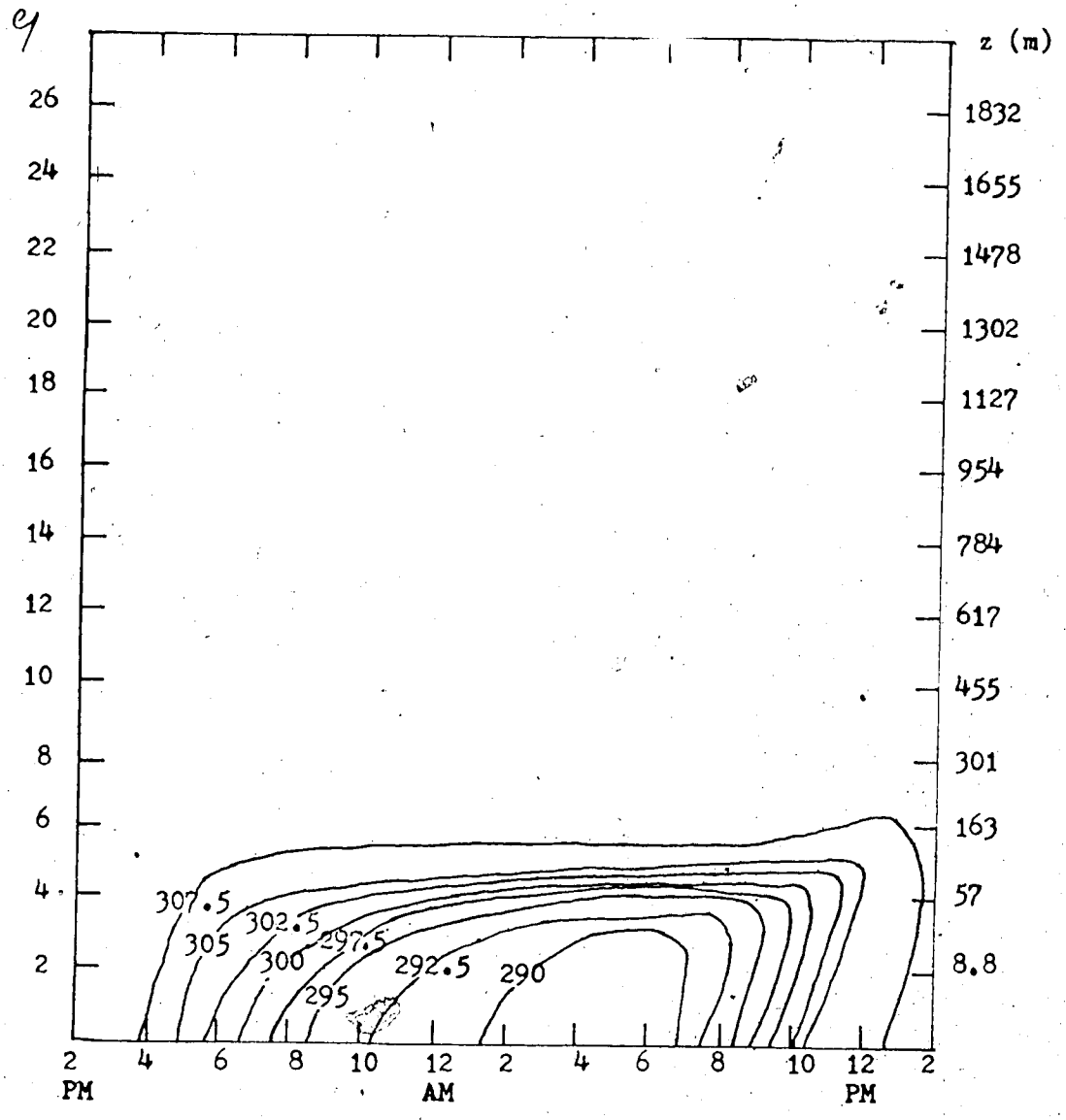

Figure 25. Diurnal cycle of the atmospheric potential temperature for the case z_o = 100 cm, V_g = 10 m/sec and high soil conductivity. The units are [°K].

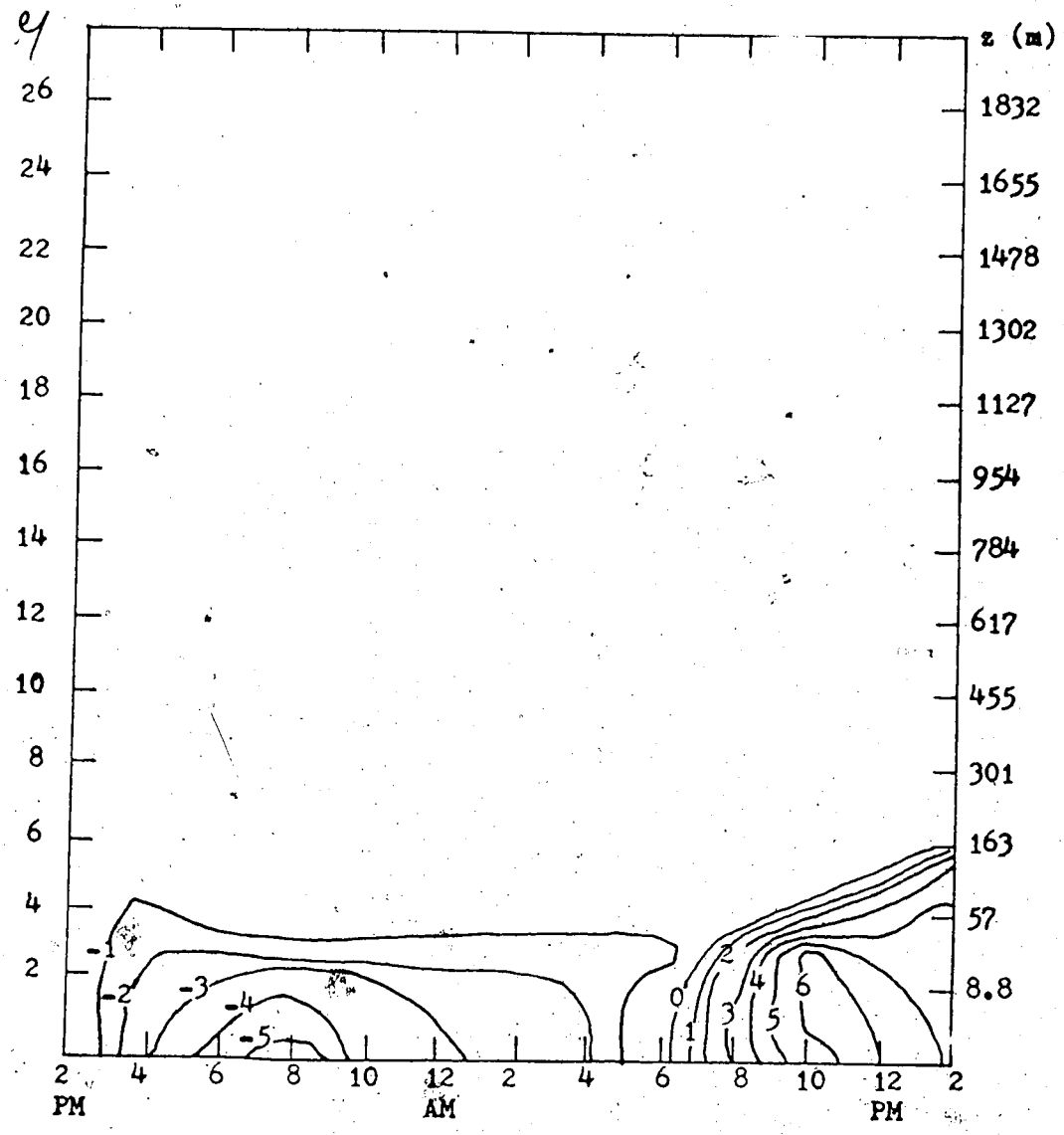

Figure 26. Diurnal cycle of the vertical profile of $\overline{w\theta}$ for the case z_o = 100 cm, V_g = 10 m/sec and high soil conductivity. The units are [cm- °C/sec].

lower boundary layer, the heat flux is about twice as large over rough terrain between 4 PM and 8 PM. After 8 PM, the difference between the two heat fluxes diminishes to become negligible by sunrise. The influence of the larger roughness height is reflected in the fact that the heat flux has a larger value over a deeper layer over rough terrain than over the smooth terrain. There is also more diffusion over rougher terrain as demonstrated by the higher values of K_t in Fig. 27 as compared to Fig. 16.

Comparing Figs. 28 and 23, we note that the turbulent energy in the surface layer is increased by 50% over rough terrain during daytime, and only by 25% overnight.

Figs. 29 and 18 show that the diurnal cycle of U is similar over smooth and rough terrains. The overnight wind gradient which was concentrated between 20 m and 50 m over smooth terrain is now spread between 20 m and 100 m over the rougher terrain. The double-wind-maxima feature above 100 m is also very evident over rough terrain. The diurnal cycle of V over rough terrain is very similar to the one over smooth terrain as demonstrated by the comparison of Fig. 30 with Fig. 21. The rough terrain induces more turbulence which causes a spreading of the wind gradient and a shifting of the maximum wind speed higher. The only other major difference is in the roughness angle which is illustrated in Fig. 11. The roughness angle is generally 10 to 15 degrees greater over the rougher terrain. The oscillation in α after sunrise has a larger amplitude over the rough terrain and reaches 40°.

Therefore, the rougher terrain creates more turbulence at all times even if the difference in turbulent energy and heat flux

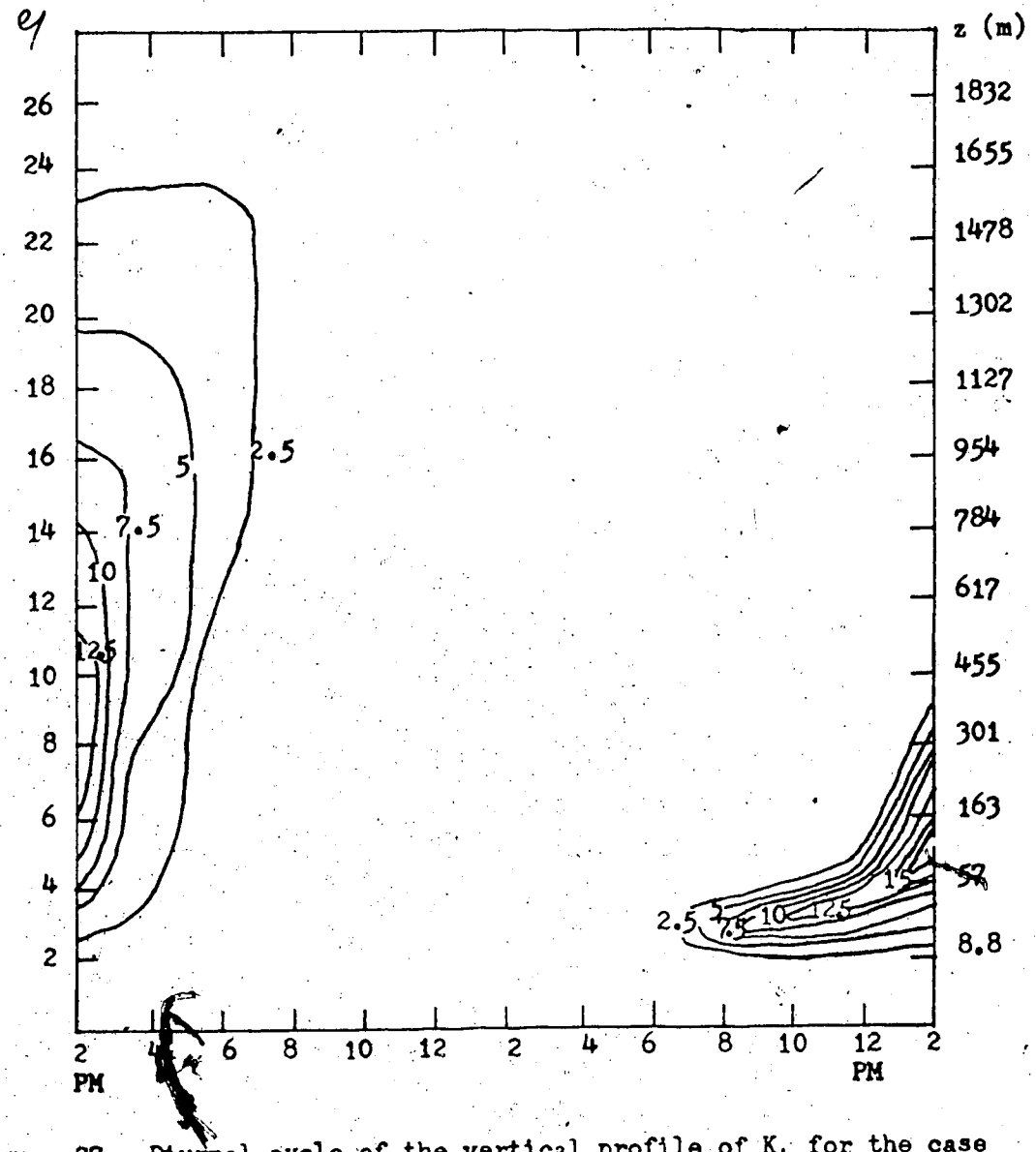

Figure 27. Diurnal cycle of the vertical profile of K_t for the case z_o = 100 cm, V_g = 10 m/sec and high soil conductivity. The units are $[10^4\ cm^2/sec]$.

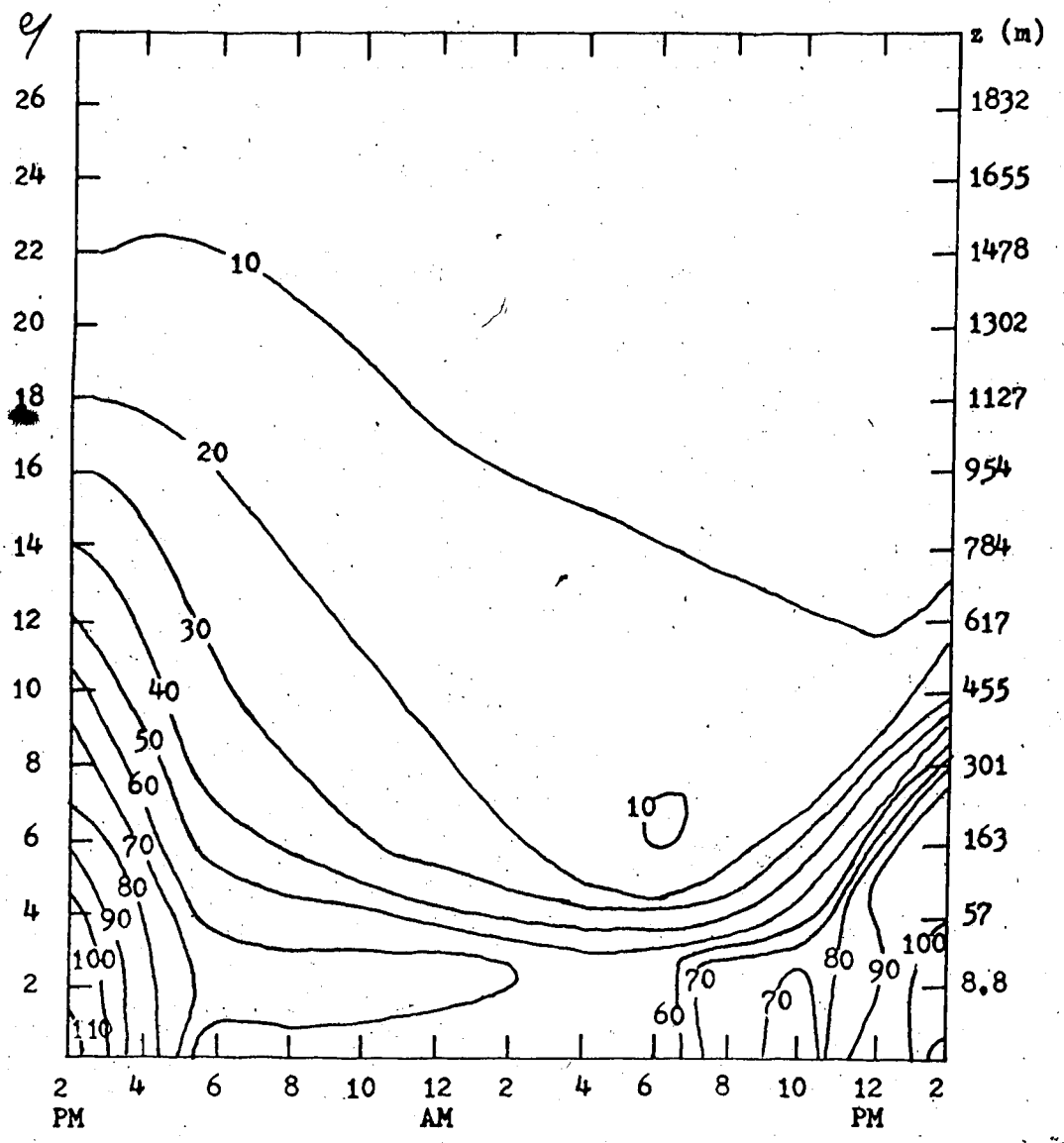

Figure 28. Diurnal cycle of the vertical profile of e for the case z_o = 100 cm, V_g = 10 m/sec and high soil conductivity. The units are $[cm^2/sec^2]$.

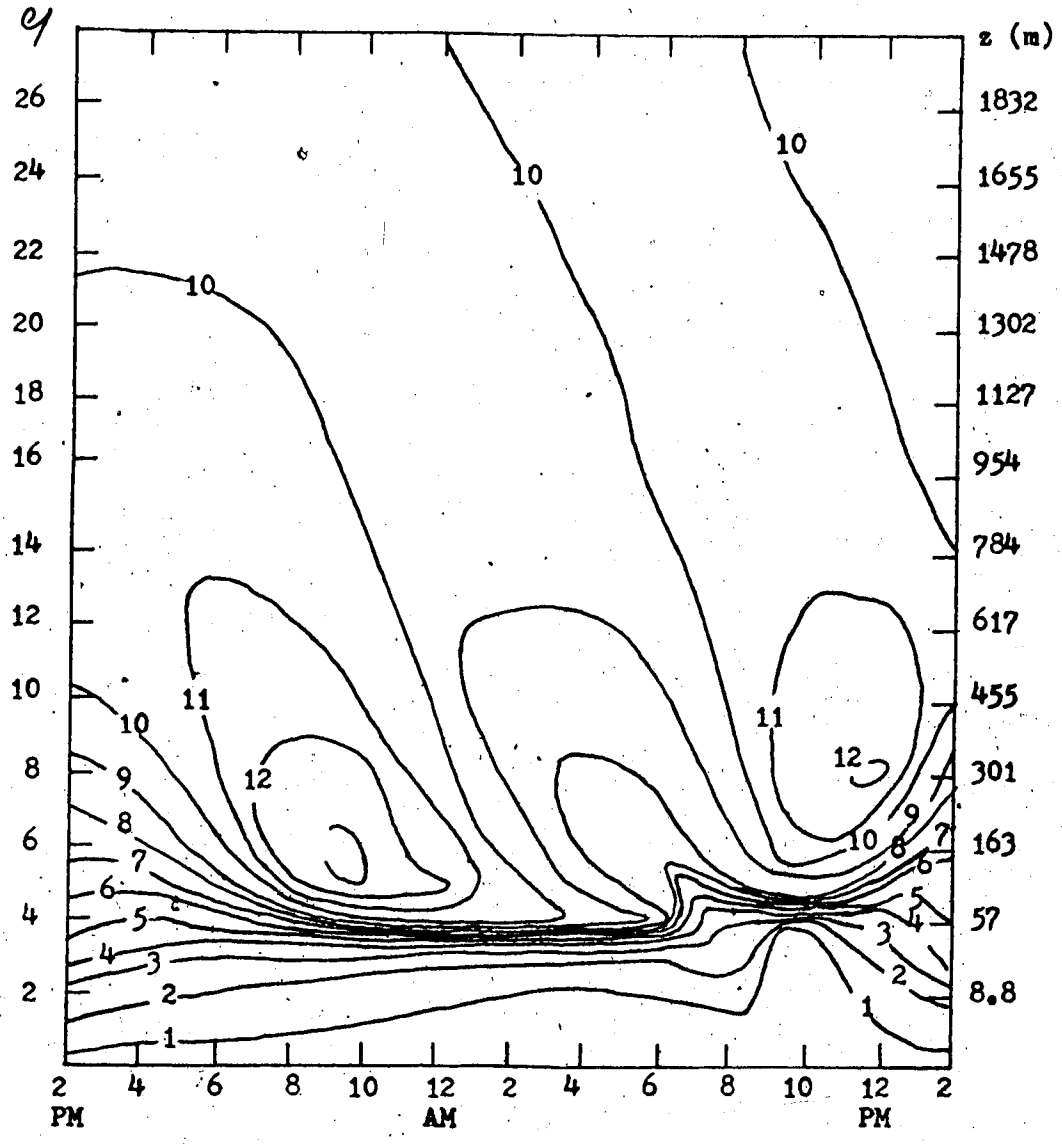

Figure 29. Diurnal variation of the vertical profile of U for the case z_o = 100 cm, V_g = 10 m/sec and high soil conductivity. The units are [m/sec].

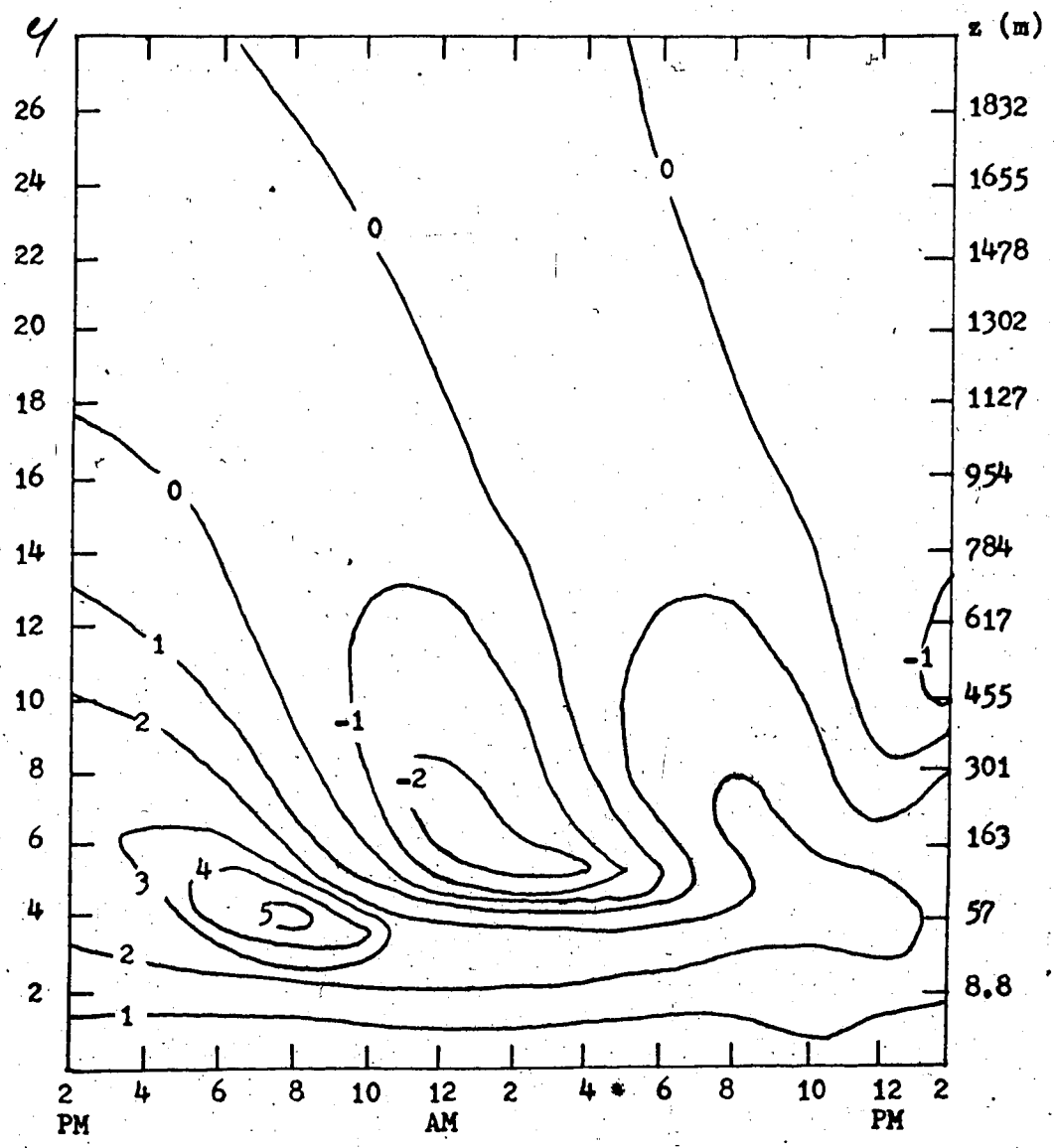

Figure 30. Diurnal variation of the vertical profile of V for the case z_o = 100 cm, V_g = 10 m/sec and high soil conductivity. The units are [m/sec].

is reduced overnight due to the stability. The greater cooling over the rougher terrain between 8 AM and 4 PM remains unexplained. A plausible explanation would be that the two simulations have not converged sufficiently to their true values at each time step, creating an artificial difference between the two simulations which has persisted overnight. Therefore, it seems necessary to require more accuracy than 10 cm^2 /sec overnight because the maximum value of K_t is reduced by an order of magnitude overnight which reduces considerably the relative accuracy with which we solve the equations.

6.2.3 Effect of the Soil Conductivity.

Fig. 9 shows that the effect of decreasing the soil thermal conductivity is to amplify the diurnal temperature wave at the surface of the earth. The maximum surface temperature is increased by 18.5 °C and the minimum by 2.8 °C. As indicated in Fig. 10, the warming rate is twice as large over the poorly-conductive soil. The graphs of (H) and $\overline{w\theta}$ over the poorly-conductive soil are Figs. 31 and 32. These are very similar to Figs. 13 and 15 which represent the same variables over a good conductive soil. The only major difference is in the intensity of the cooling which is more pronounced over a soil with low thermal conductivity. Fig. 33 reveals the influence of the amplification of the diurnal temperature wave on the atmospheric diffusivity. Over a poorly conductive soil, K_t is larger under unstable conditions and smaller under stable conditions.

The behavior of e over a soil with low conductivity is represented in Fig. 34 and is basically the same as over a soil with high conductivity as represented in Fig. 23. Due to strong cooling, the

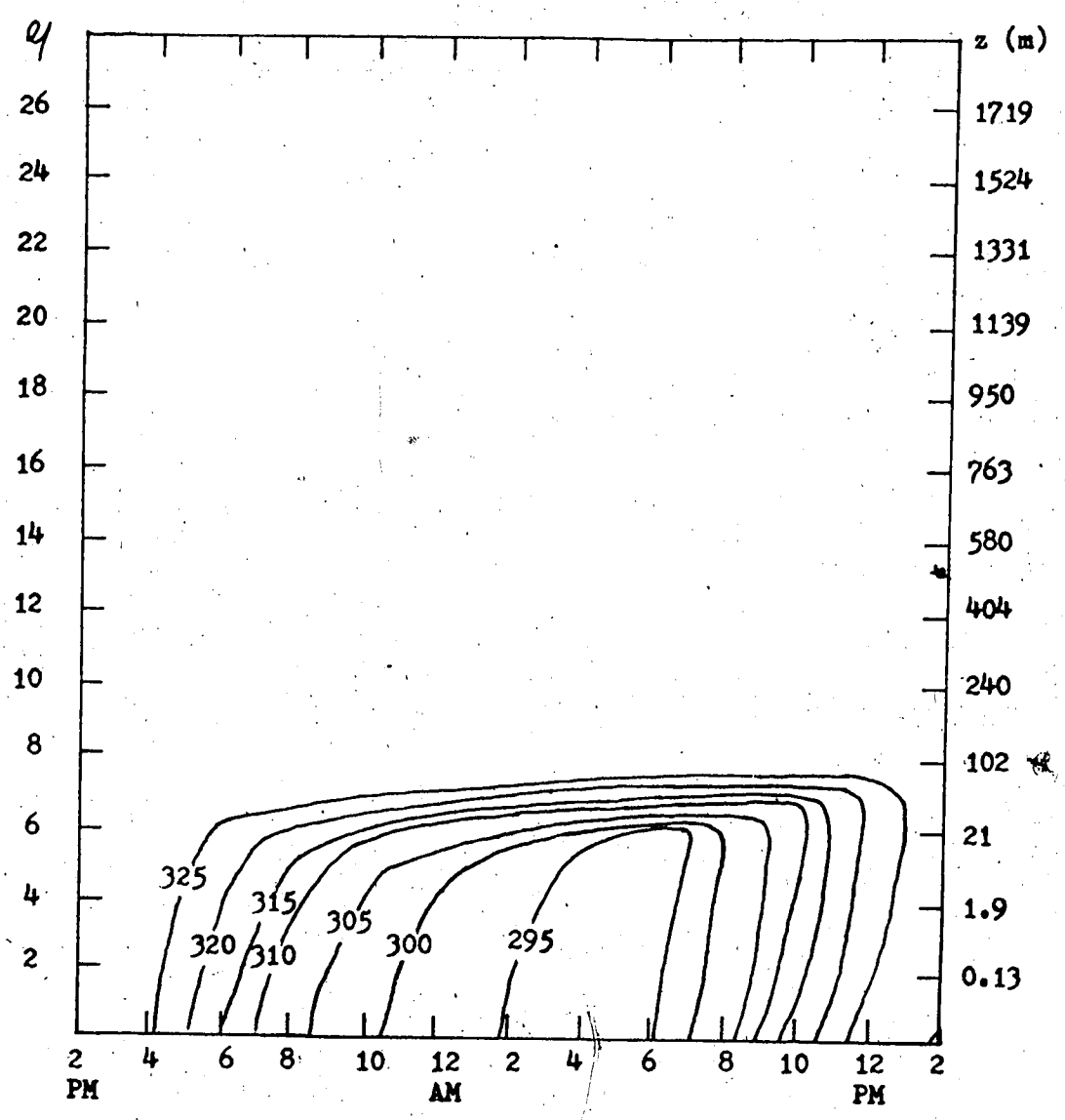

Figure 31. Diurnal cycle of the vertical profile of the potential temperature for the case z_o = 1 cm, V_g = 10 m/sec and low conductivity in the soil. The units are [°K].

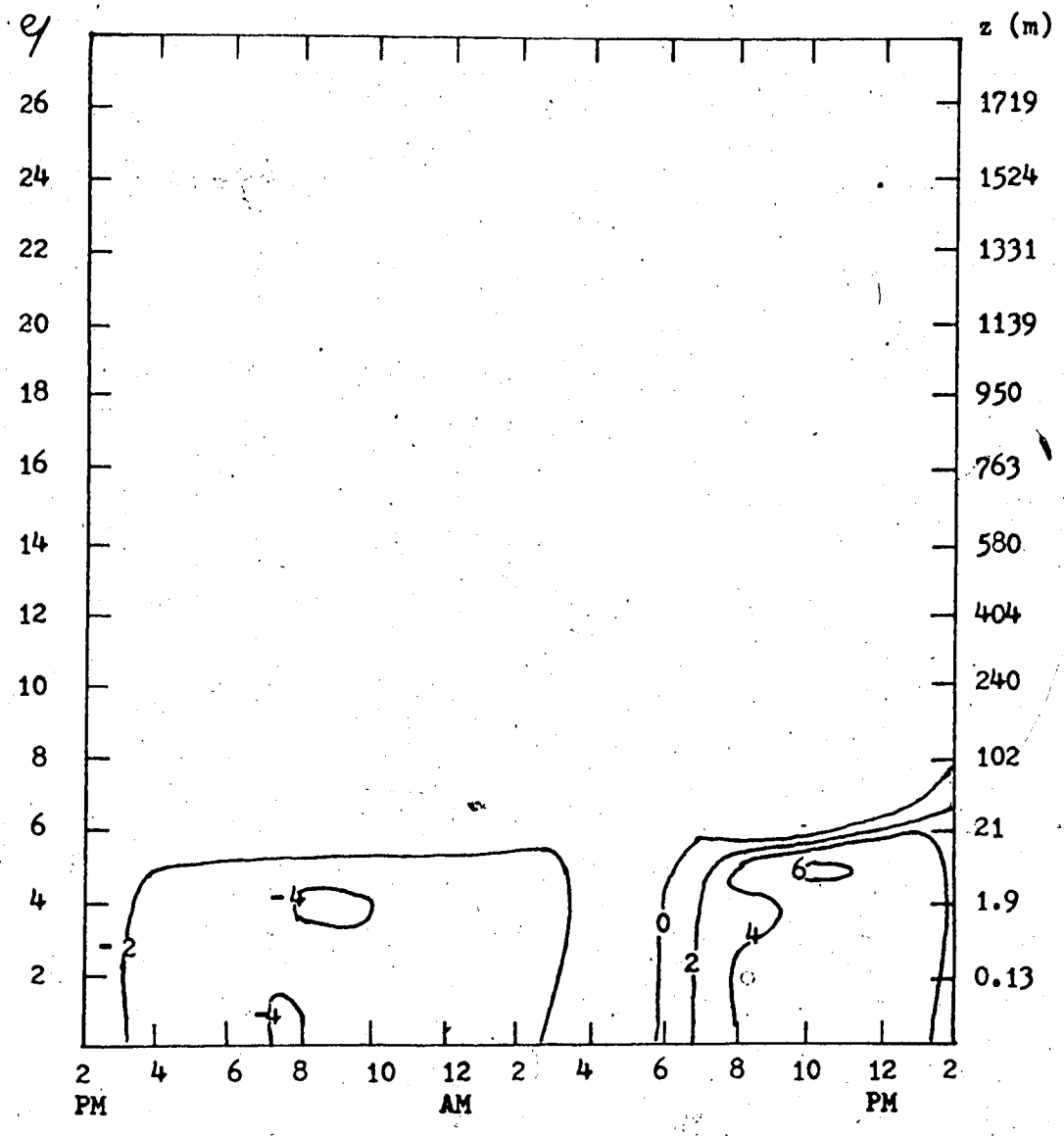

Figure 32. Diurnal cycle of the vertical profile of $\overline{w\theta}$ for the case $z_o = 1$ cm, $V_g = 10$ m/sec and low thermal soil conductivity. The units are [cm-°C/sec].

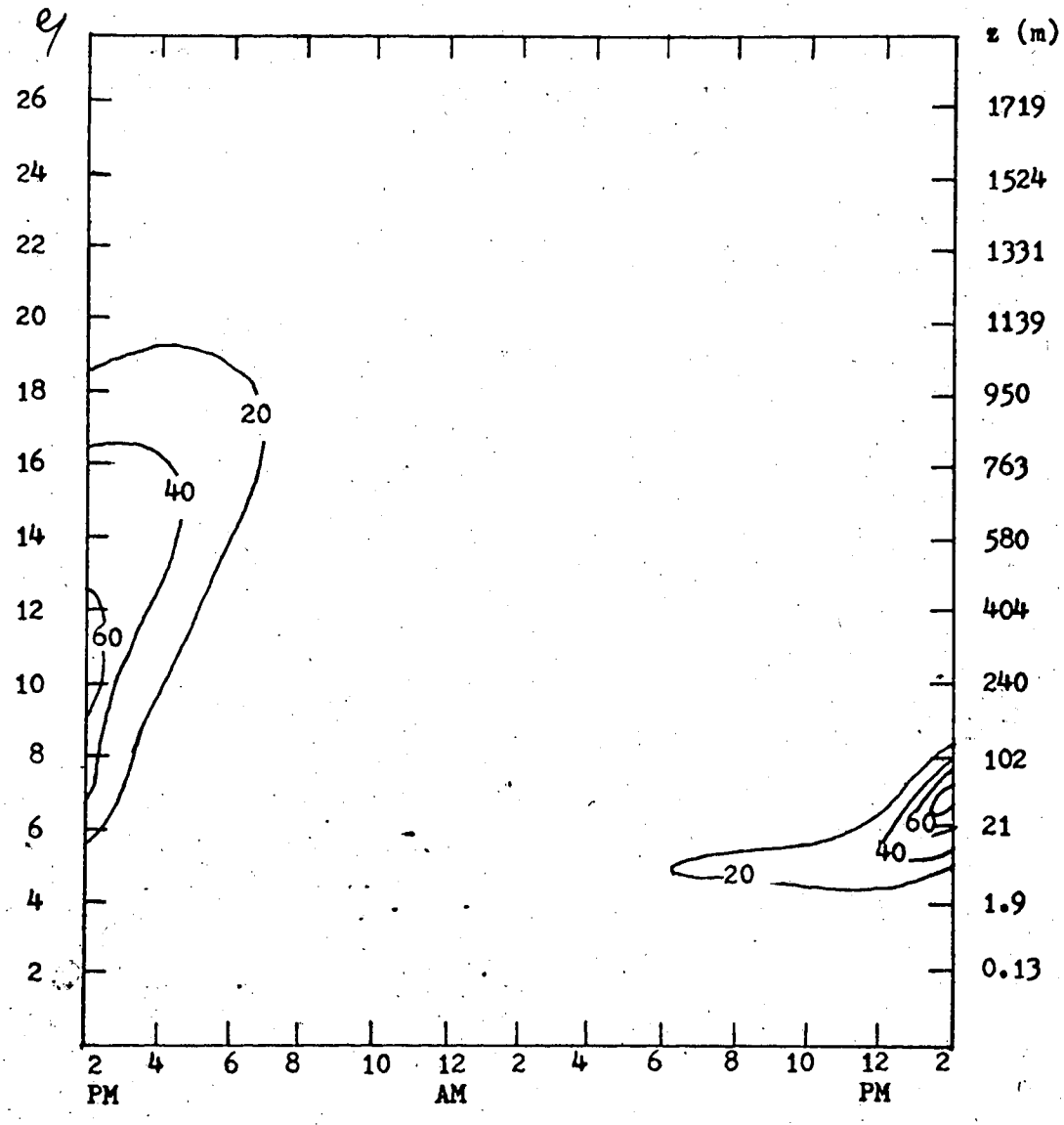

Figure 33. Diurnal cycle of the vertical profile of K_t for the case z_o = 1 cm, V_g = 20 m/sec and high soil conductivity. The units are [cm^2/sec].

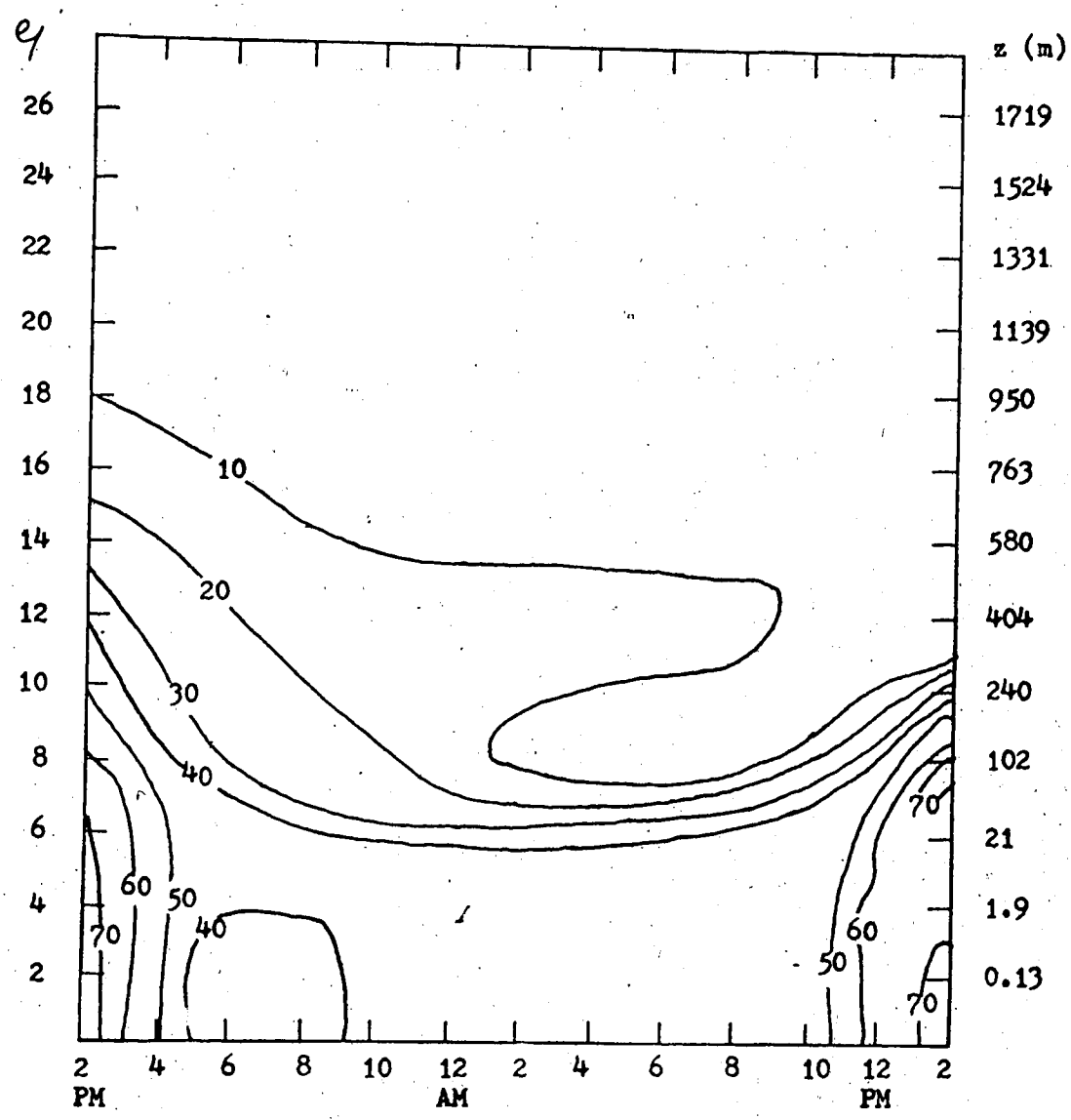

Figure 34. Diurnal cycle of the vertical profile of e for the case z_o = 1 cm, V_g = 10 m/sec and low thermal soil conductivity. The units are $[cm^2/sec^2]$.

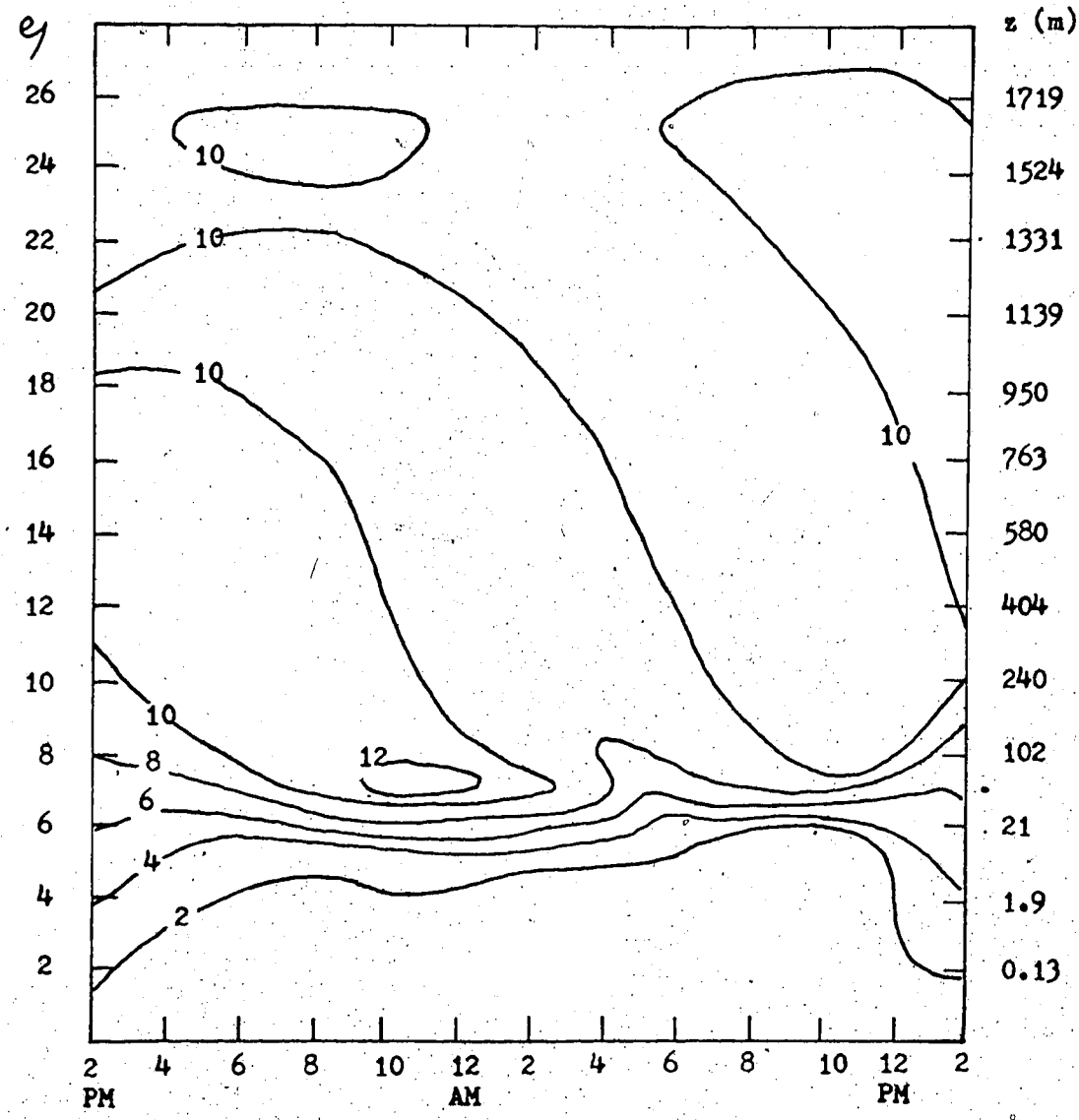

Figure 35. Diurnal cycle of the vertical profile of U for the case z_o = 1 cm, V_g = 10 m/sec and low soil conductivity. The units are [m/sec].

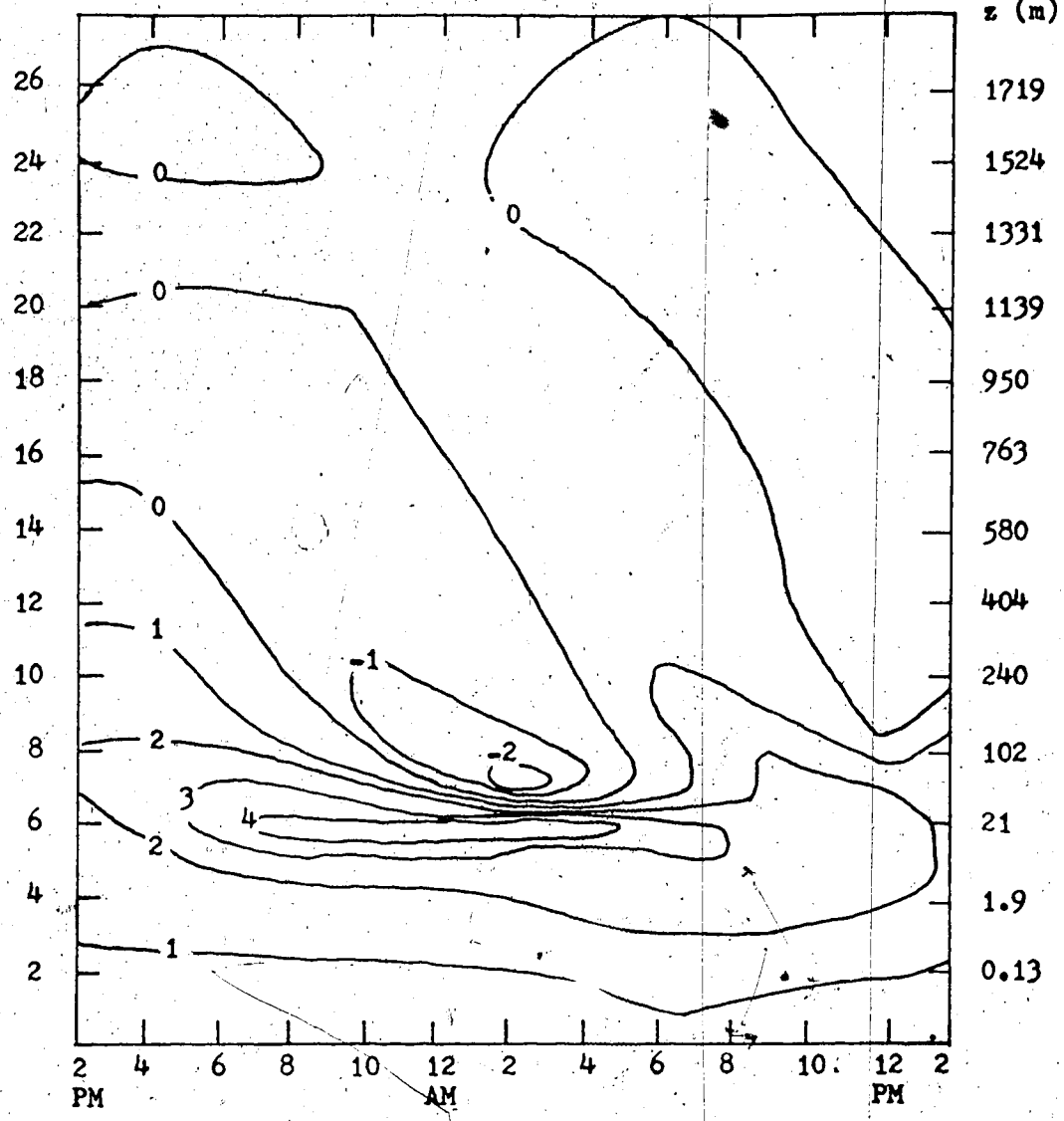

Figure 36. Diurnal variation of the vertical profile of V for the case z_o = 1 cm, V_g = 10 m/sec and low soil conductivity. The units are [m/sec].

minimum near 6 PM is 15% lower over a poorly-conductive soil. However, e recovers after 12 AM and has almost the same profile as over soil with a high conductivity.

Figs. 35 and 36 represent the U and V profiles over a poorly-conductive soil. These are similar to the profiles over a good-conductive soil as represented in Figs. 18 and 21. The overnight minimum in U within the surface layer is reduced by about 20% over a poorly-conductive soil. Above the region of maximum wind gradient, the double-wind-maxima cycle is still observed but with an amplified amplitude. As shown in Fig. 11, the variations in α are amplified over a poorly-conductive soil, with higher maxima and lower minima.

6.2.4 Examination of the Other Variables.

We will examine very briefly the behavior of the other atmospheric variables. Only one specific case will be studied: z_o = 1 cm, V_g = 20 m/sec and high soil conductivity. This case was chosen for the following reasons:

a) the profiles of most of the variables are smoother with strong geostrophic winds.

b) The overnight gradients in Θ, U, V and e are spread out over a few more grid points.

c) K_t becomes negative at fewer grid points.

The diurnal variation of l is fairly regular as shown in Fig. 37. The diurnal variation is negligible close to z_o, reaches 8% of the mean value at 21 m and exceeds 50% of the mean value near the top of the boundary layer. Due to its definition, l is always increa-

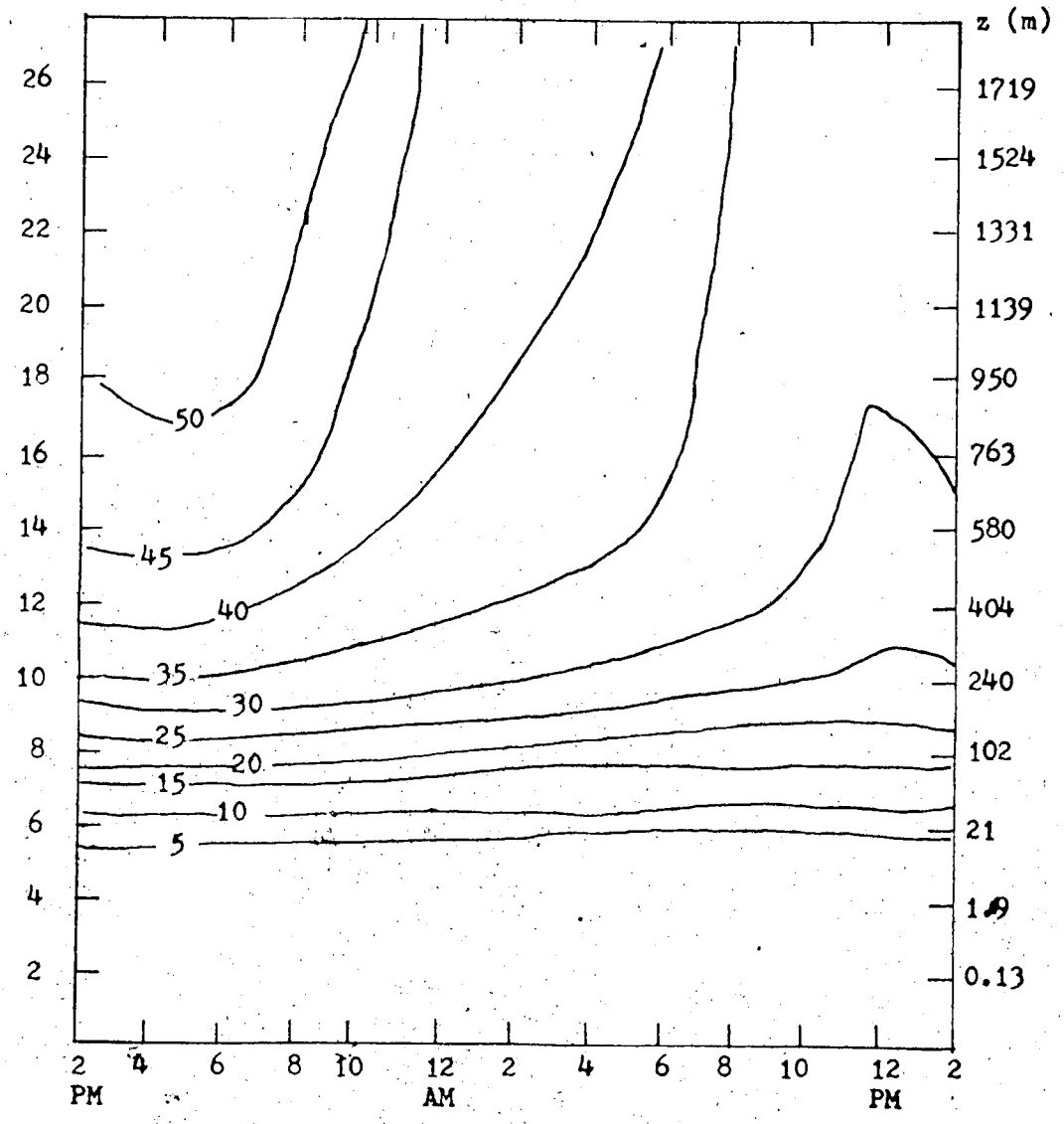

Figure 37. Diurnal variation of the vertical profile of ℓ for the case z_o = 1 cm, V_g = 20 m/sec and high soil conductivity. The units are [m].

sing upwards. The delay of 6 to 8 hours between the time of change in stability in the lower boundary layer and the time of minimum for ℓ indicates clearly that the formula which computes ℓ depends to a large degree on the value of e in the uppermost levels.

As illustrated in Fig. 38, $\overline{\theta^2}$ reaches an overnight maximum in the lower boundary layer just after the time of maximum cooling rate and decreases until the air becomes unstable near 6 AM. Between 8 AM and 12 PM there is a rapid increase in $\overline{\theta^2}$ which corresponds to the increase in the warming rate. Under unstable conditions the maximum value of $\overline{\theta^2}$ is always near the surface. However, the temperature gradient accumulates overnight between 20 m and 100 m. This is reflected in the large overnight maximum in $\overline{\theta^2}$ in that region.

The diurnal cycles of $\overline{u\theta}$ and $\overline{v\theta}$ are shown in Figs. 39 and 40. Equations (2.195) and (2.196) indicate that these variables are proportional to the product of the appropriate wind gradient by the temperature gradient. Therefore, under stable conditions, these variables are positive if the wind increases with height and negative if the wind decreases with height. As the wind and temperature gradients accumulate overnight between 20 m and 100 m, the maximum value is reached in that region.

Figs. 41 and 42 illustrate the stress in the x and y directions. In the lower boundary layer, $\overline{u\,w}$ has a large negative value during daytime and a smaller negative value during nighttime. This is another illustration of the effect of the decreasing turbulence overnight. $\overline{v\,w}$ decreases between 2 PM and 6 PM but increases after 6 PM. Therefore, the overnight increase in roughness angle is accompanied by an increase in the stress in the y direction. These va-

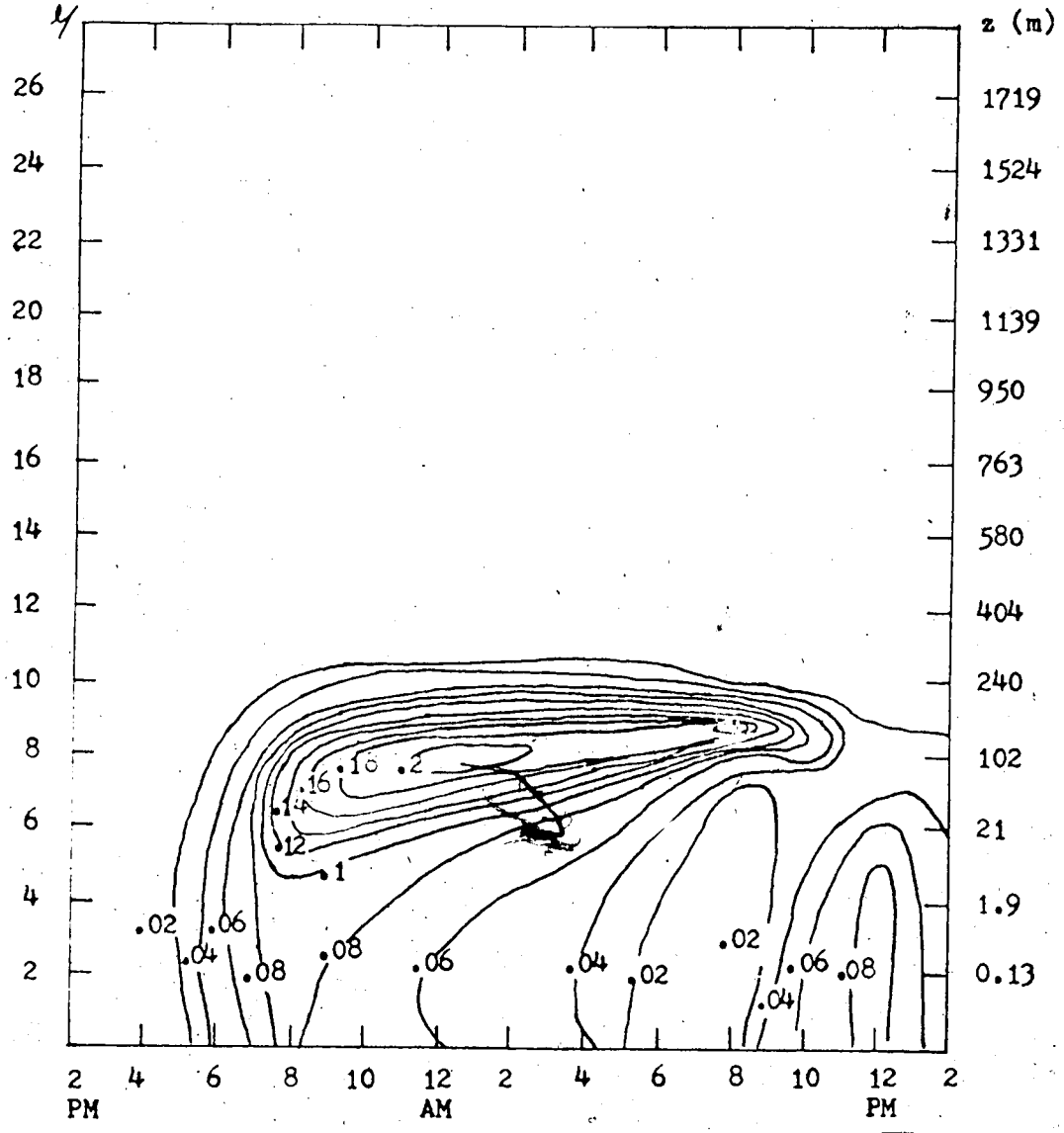

Figure 38. Diurnal variation of the vertical profile of $\overline{\theta^2}$ for the case z_o = 1 cm, V_g = 20 m/sec and high soil conductivity. The units are $[{}^{o}C^2]$.

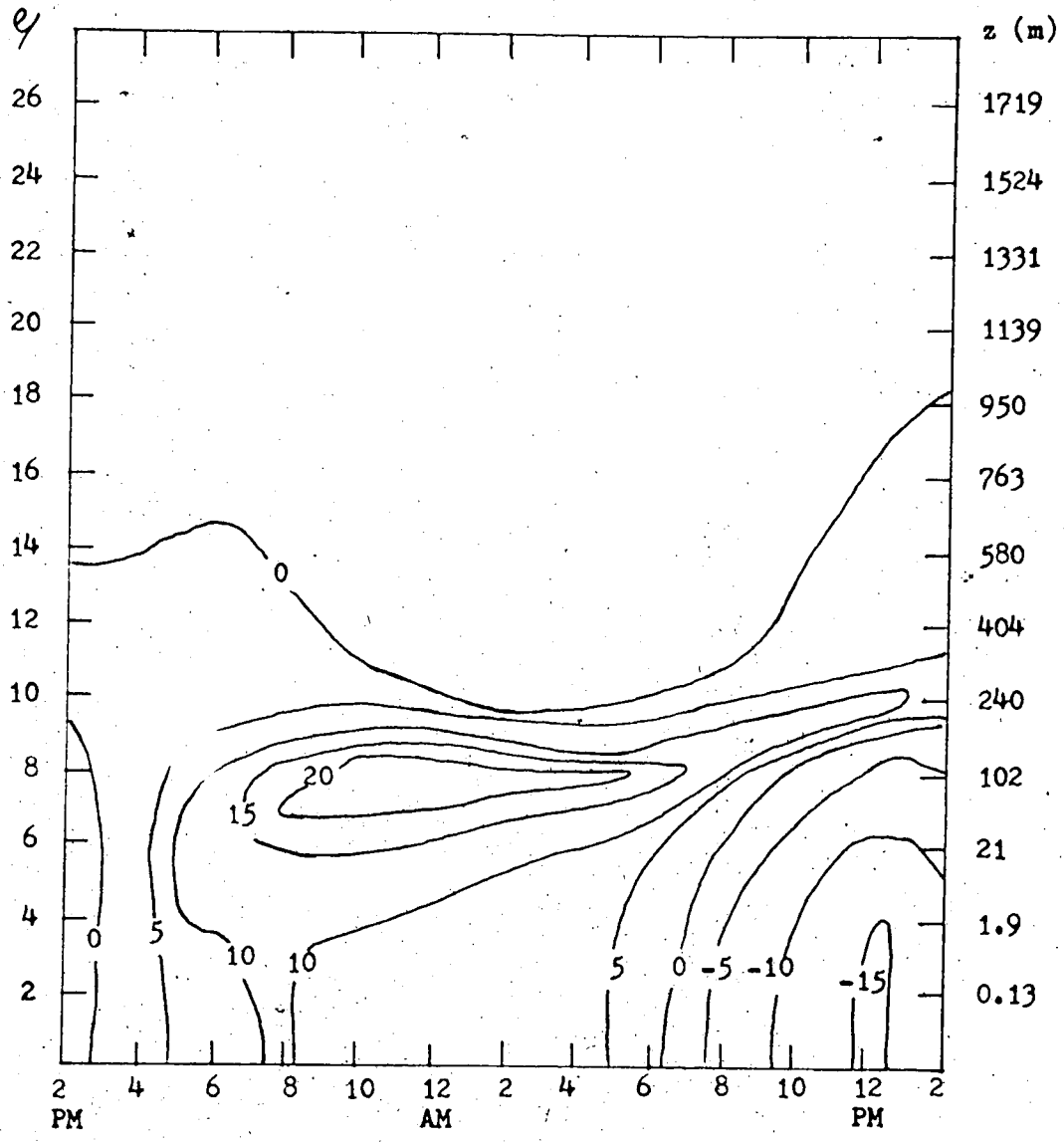

Figure 39. Diurnal cycle of the vertical profile of $\overline{u\theta}$ for the case z_o = 1 cm, V_g = 20 m/sec and high soil conductivity. The units are [cm-°C/sec].

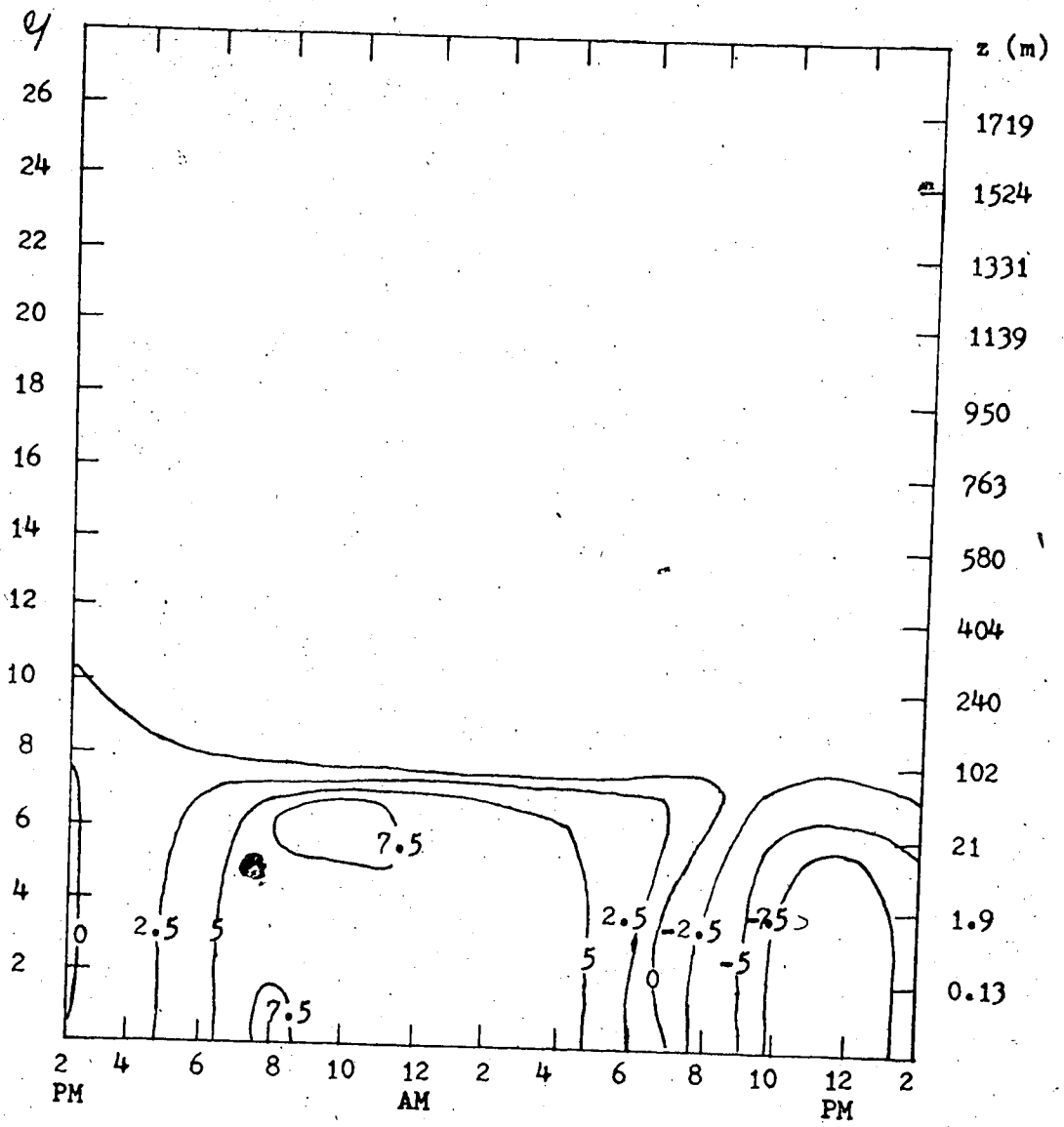

Figure 40. Diurnal cycle of the vertical profile of $\overline{v\theta}$ for the case z_o = 1 cm, V_g = 20 m/sec and high soil conductivity. The units are [cm-°C/sec].

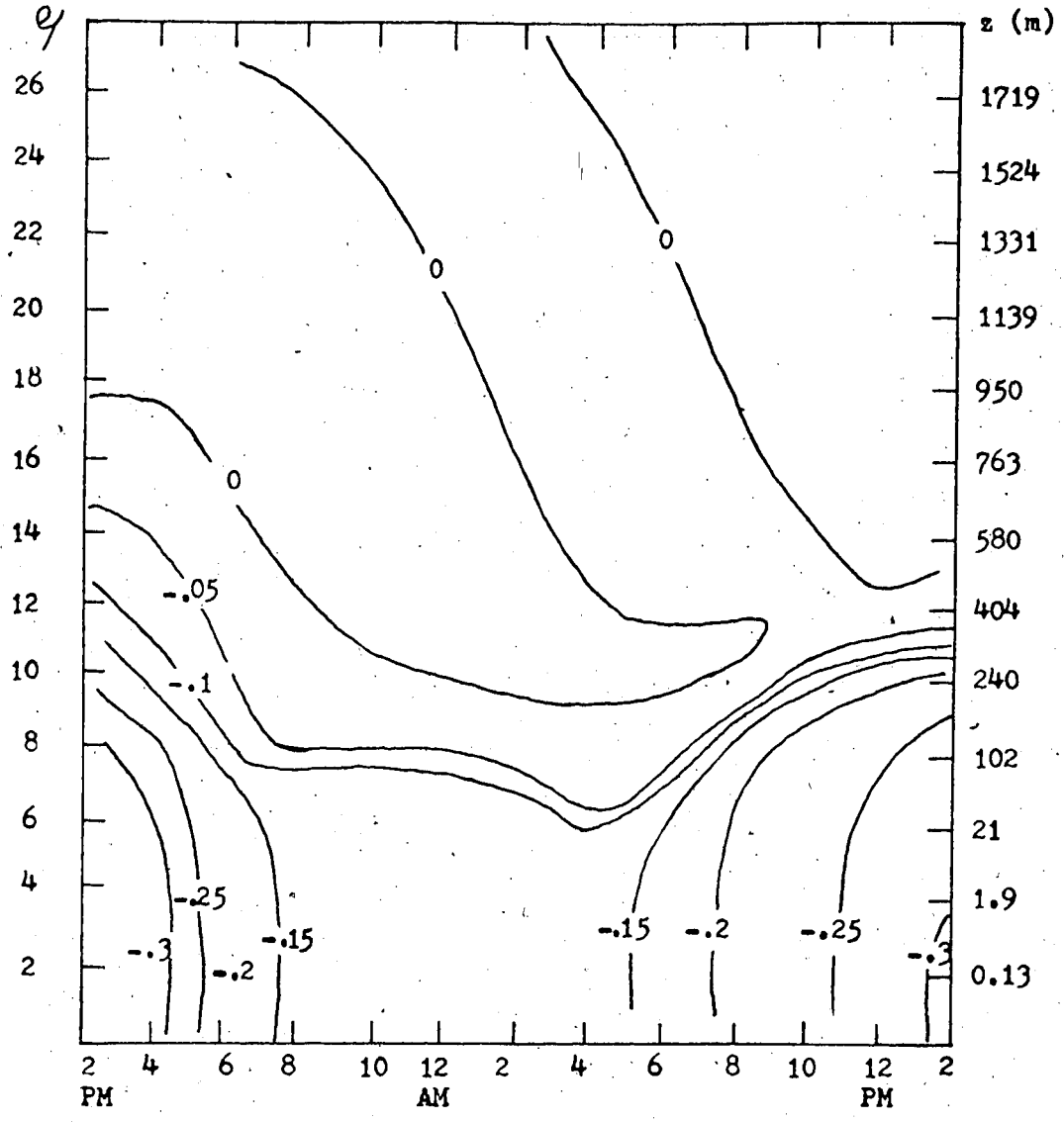

Figure 41. Diurnal variation of the vertical profile of $\overline{u\,w}$ for the case z_o = 1 cm, V_g = 20 m/sec and high soil conductivity. The units are $\left[m^2/sec^2\right]$.

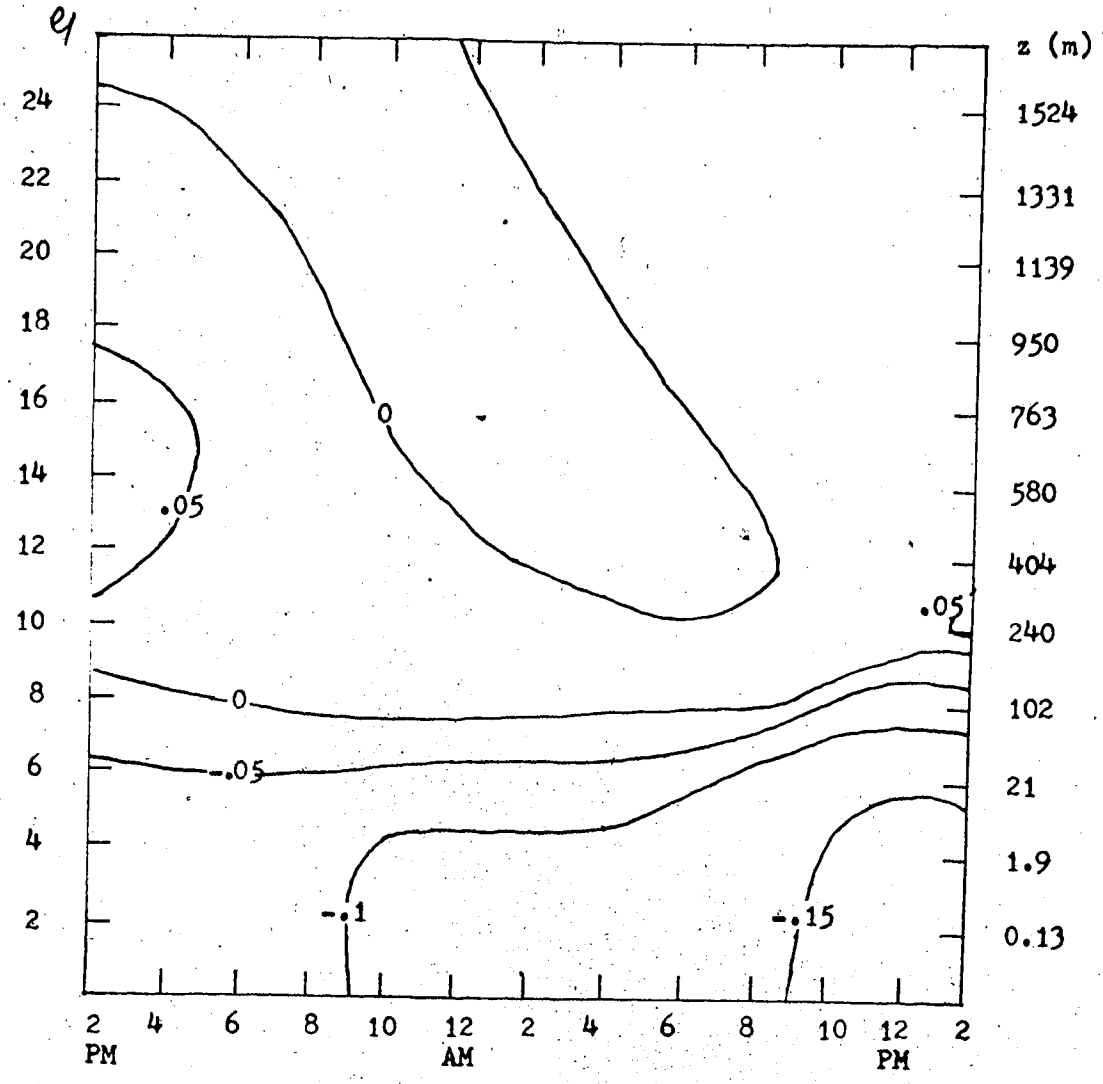

Figure 42. Diurnal cycle of the vertical profile of $\overline{v\,w}$ for the case z_o = 1 cm, V_g = 20 m/sec and high soil conductivity. The units are $[m^2/sec^2]$.

riables depend on the vertical gradient of the mean wind components.

Fig. 43 illustrates the behavior of K_m which has lower daytime values than K_t. However, K_m has a smaller tendency than K_t to develop negative values overnight.

Figs. 44 to 46 illustrate the behavior of $\overline{u^2}$, $\overline{v^2}$ and $\overline{w^2}$ whose sum is simply e^2. Therefore, their behavior is very similar to the behavior of e. They reach a maximum during daytime and a minimum overnight. The approximate daytime contributions of $\overline{u^2}$, $\overline{v^2}$ and $\overline{w^2}$ to e^2 are, respectively, 45%, 32% and 23%. Fig. 47 represents the behavior of $\overline{u\,v}$. Near the surface, the minimum is reached just after the time of maximum cooling rate and the maximum is obtained just after the time of maximum warming rate. This variable is proportional to the product of the gradients of U and V which explains the positive sign in the lowest 50 m and the negative sign in the region above 100 m.

6.3 Comparison of the Soil Temperatures.

Figs. 48 to 51 represent the diurnal variation of the soil temperature for the four simulations. The features common to all graphs are:

1- There is a time lag between the upper and lower levels in the time at which they repectively reach their maximum and minimum temperatures.

2- The temperature variation below 0.5 m is very small. This indicates that the soil depth of 1 m is appropriate for the numerical simulations for the periods of the order of one day.

3- The temperatures near the bottom increase almost continuously because the surface minimum temperature is too warm. The other levels

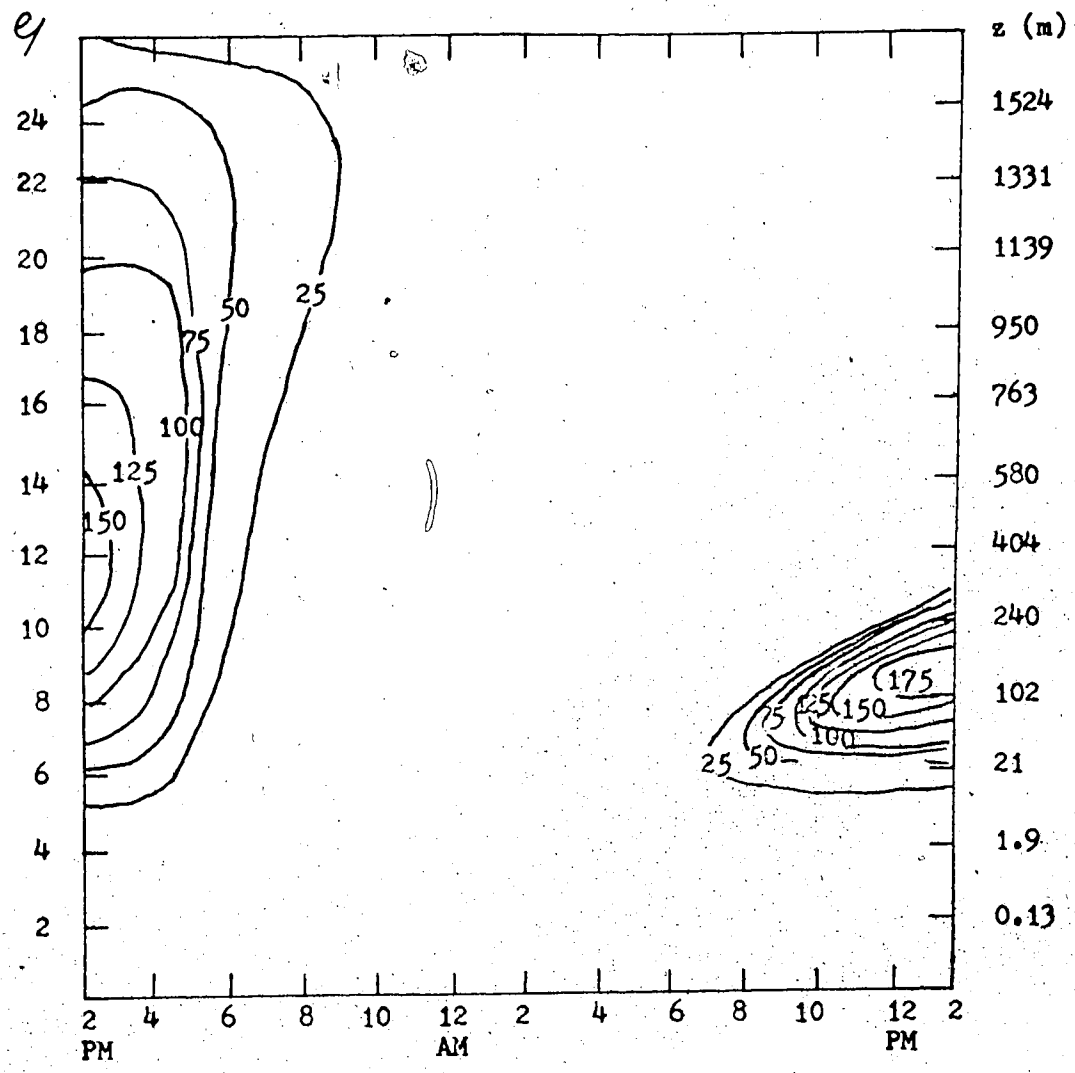

Figure 43. Diurnal cycle of the vertical variation of K_m for the case z_o = 1 cm, V_g = 20 m/sec and high soil conductivity. The units are $[10^3\ cm^2/sec]$.

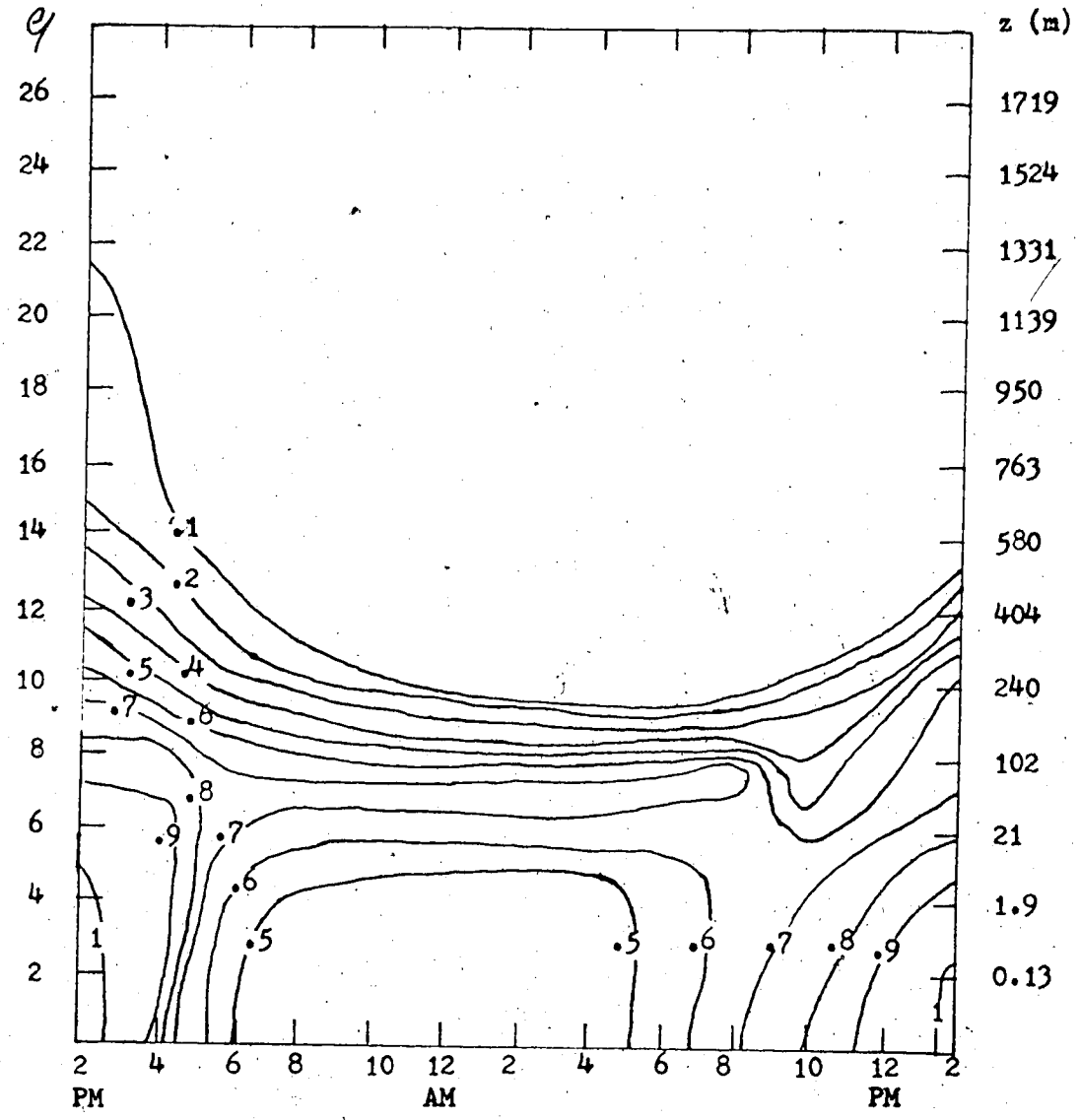

Figure 44. Diurnal variation of the vertical profile of $\overline{u^2}$ for the case z_o = 1 cm, V_g = 20 m/sec and high soil conductivity. The units are $[m^2/sec^2]$.

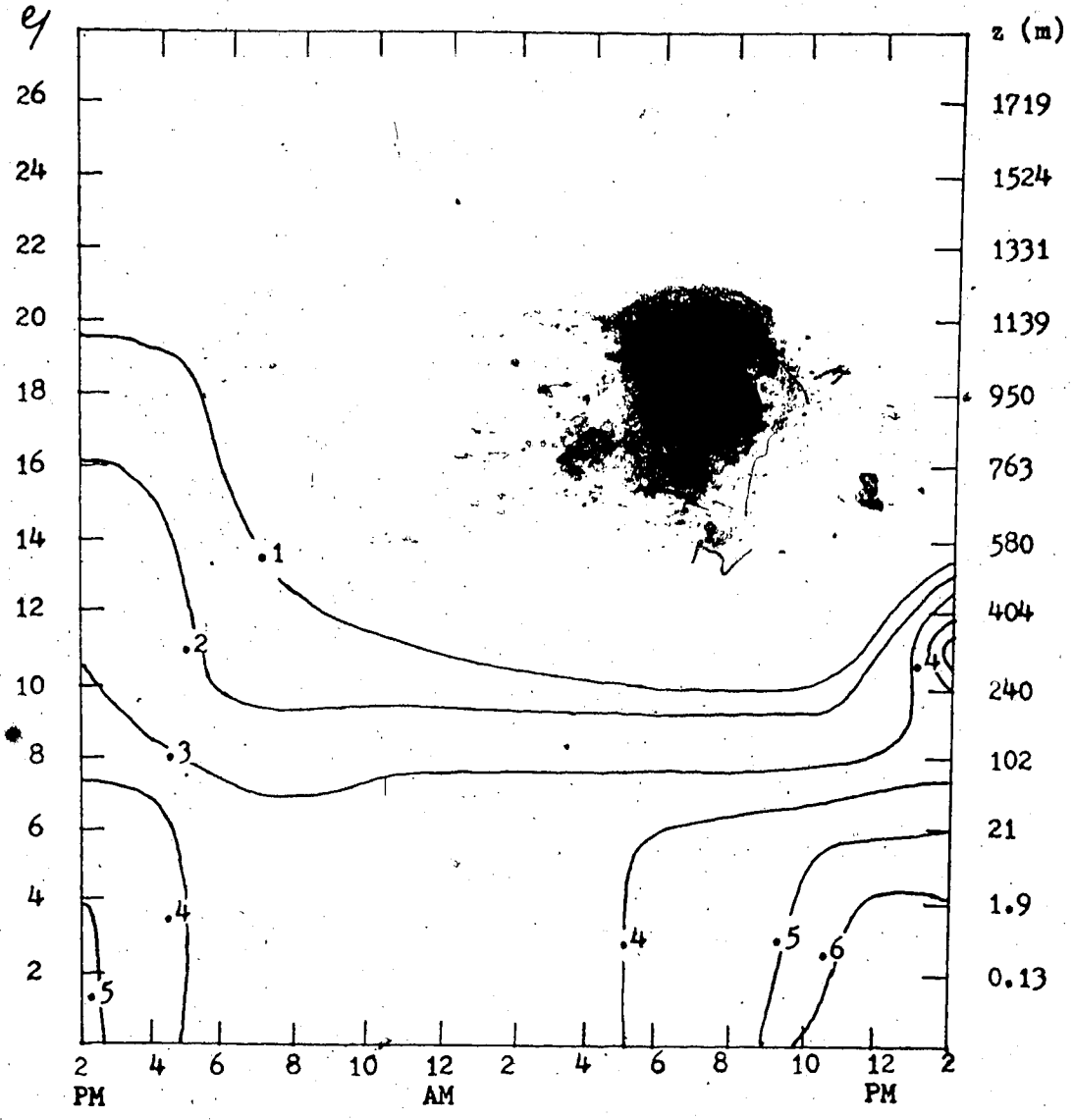

Figure 45. Diurnal variation of the vertical profile of $\overline{v^2}$ for the case z_o = 1 cm, V_g = 20 m/sec and high soil conductivity. The units are $[m^2/sec^2]$.

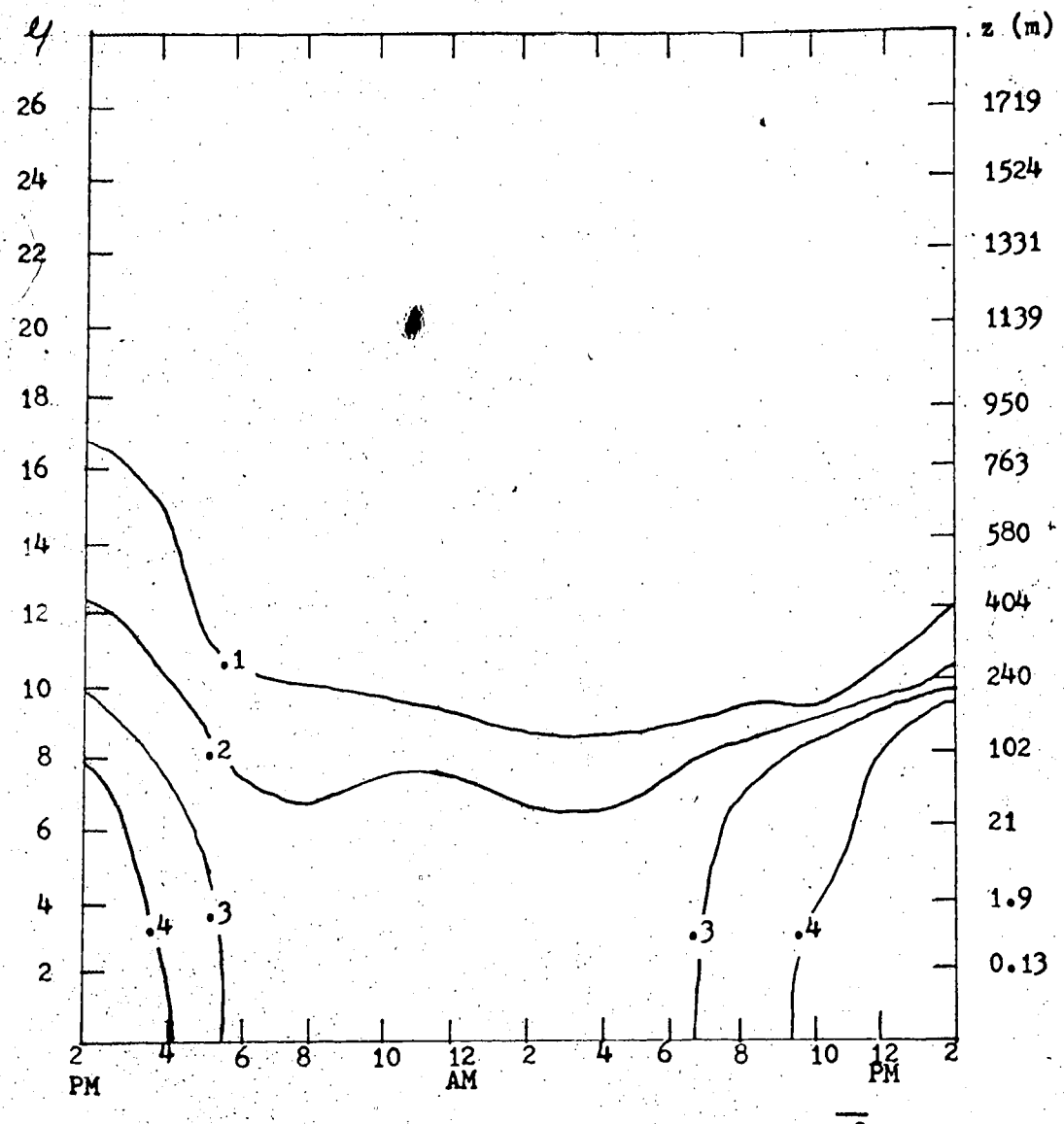

Figure 46. Diurnal variation of the vertical profile of $\overline{w^2}$ for the case z_o = 1 cm, V_g = 20 m/sec and high soil conductivity. The units are $[m^2/sec^2]$.

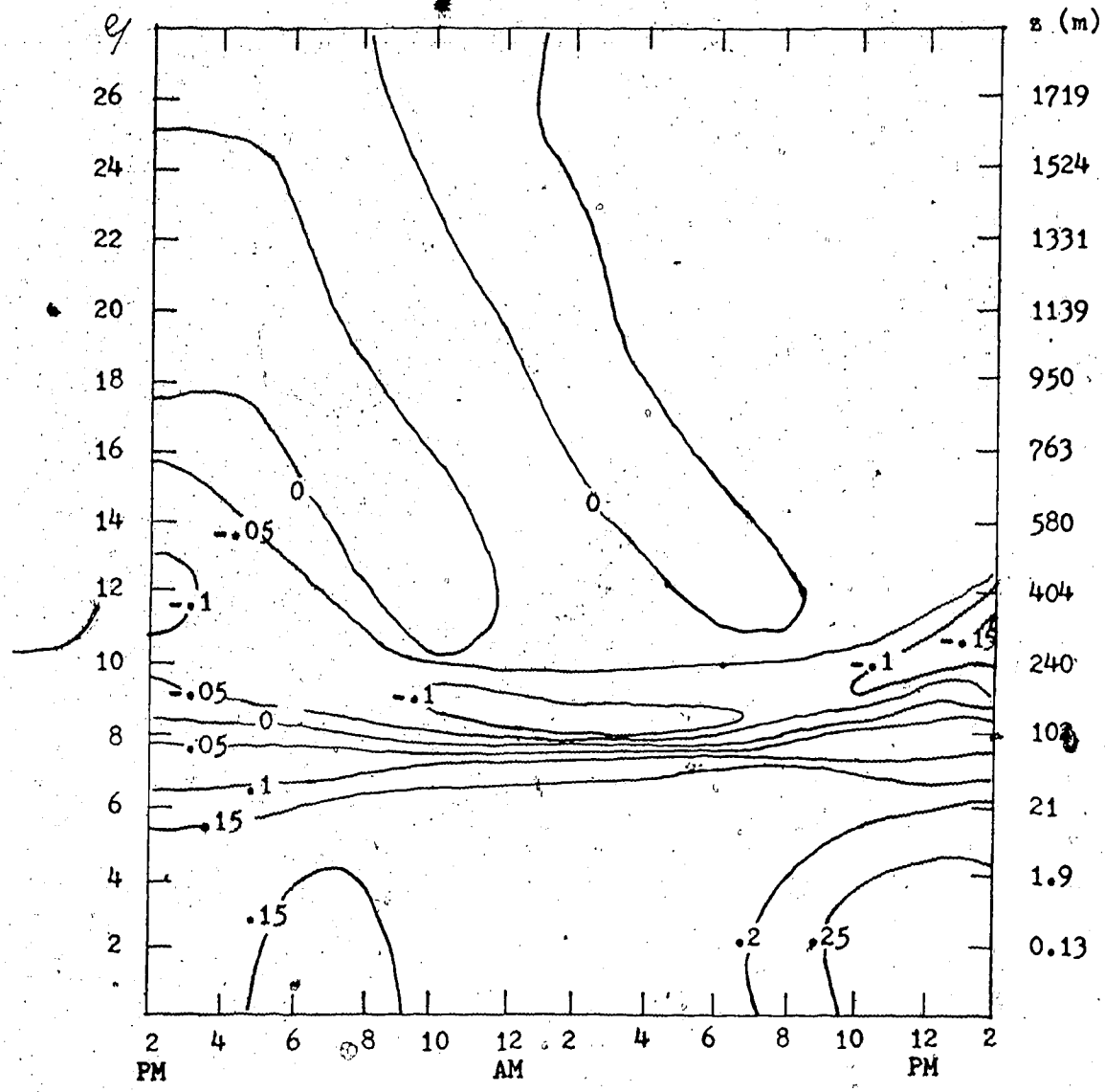

Figure 47. Diurnal variation of the vertical profile of $\overline{u\,v}$ for the case z_o = 1 cm, V_g = 20 m/sec and high soil conductivity. The units are $[m^2/sec^2]$.

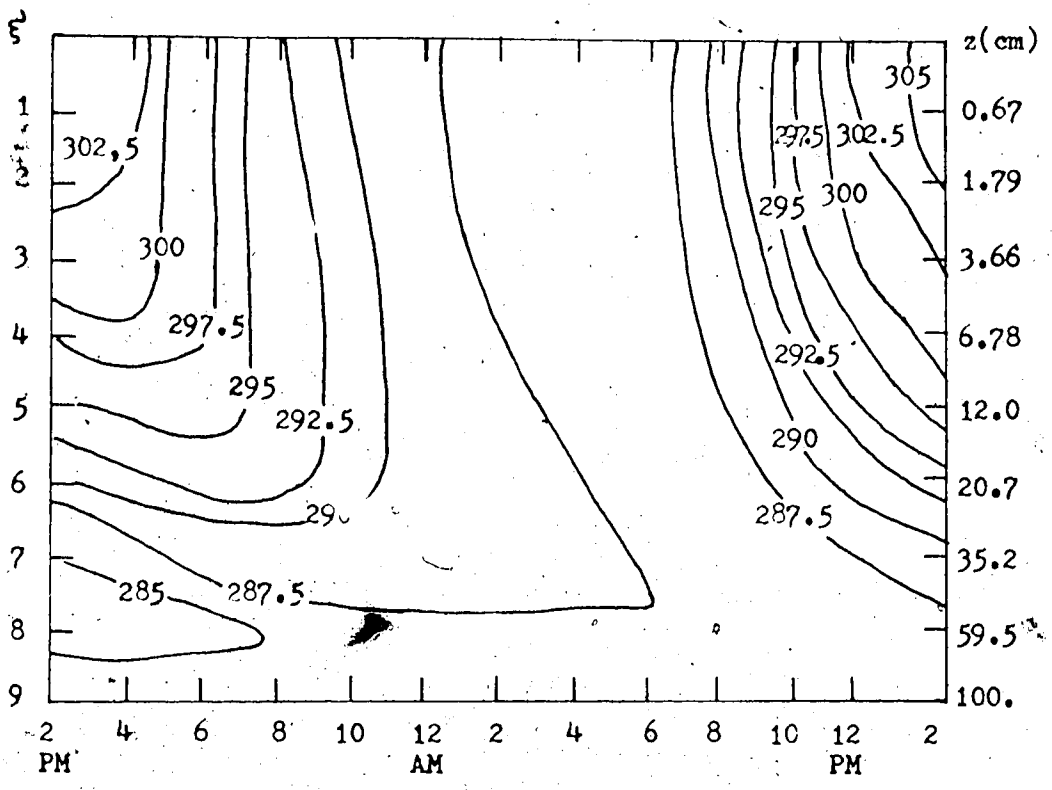

Figure 48. Diurnal variation of the soil temperature profile for the case z_o = 1 cm, V_g = 10 m/sec and high soil conductivity. The units are [°K].

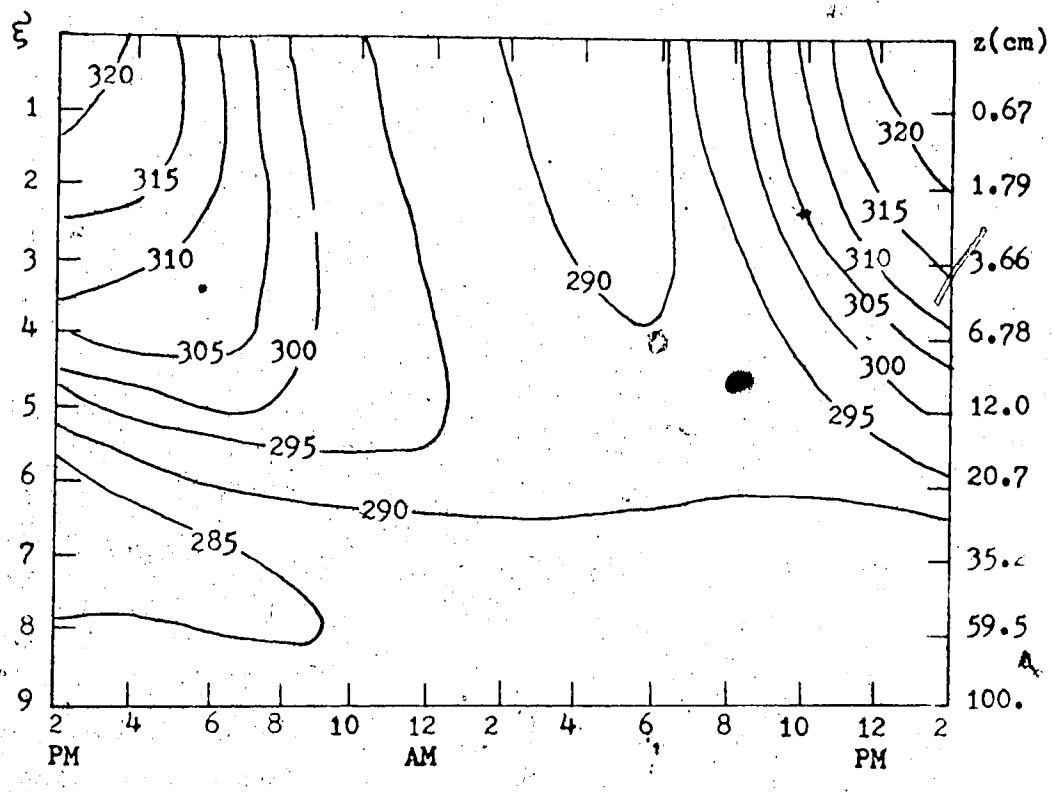

Figure 49. Diurnal variation of the soil temperature profile for the case z_o = 1 cm, V_g = 10 m/sec and low soil conductivity. The units are [°K].

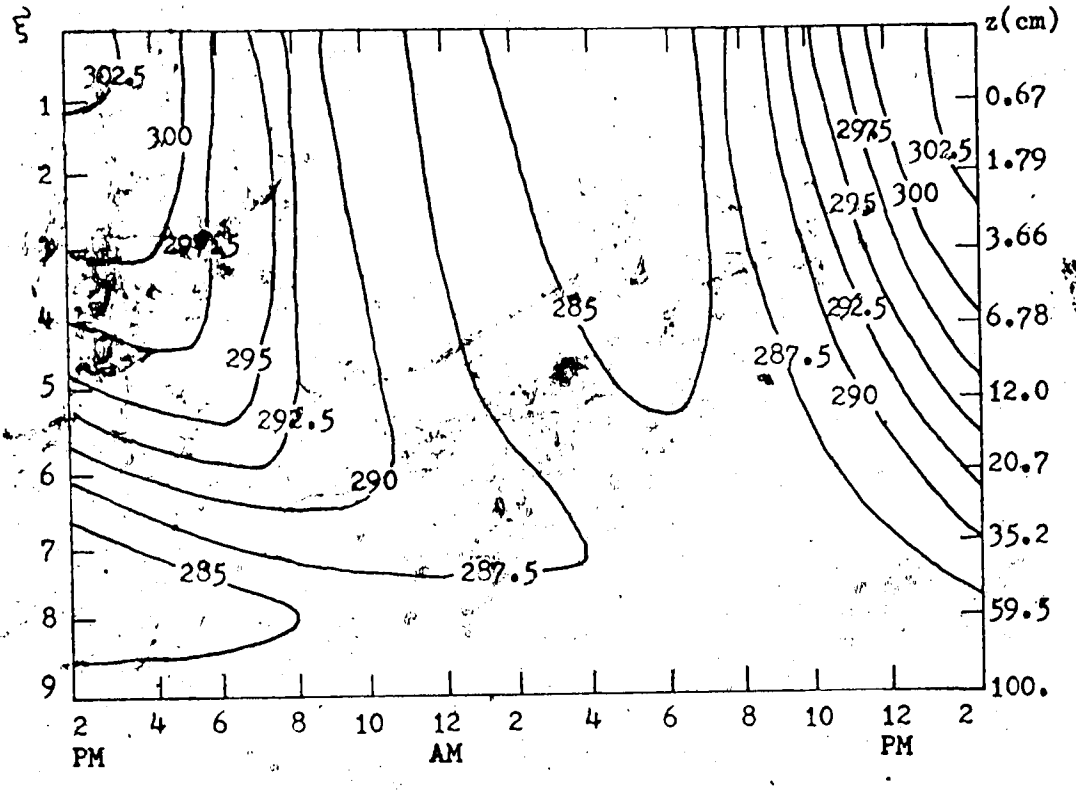

Figure 50. Diurnal variation of the soil temperature profile for the case z_o = 100 cm, V_g = 10 m/sec and high soil conductivity. The units are $[^oK]$.

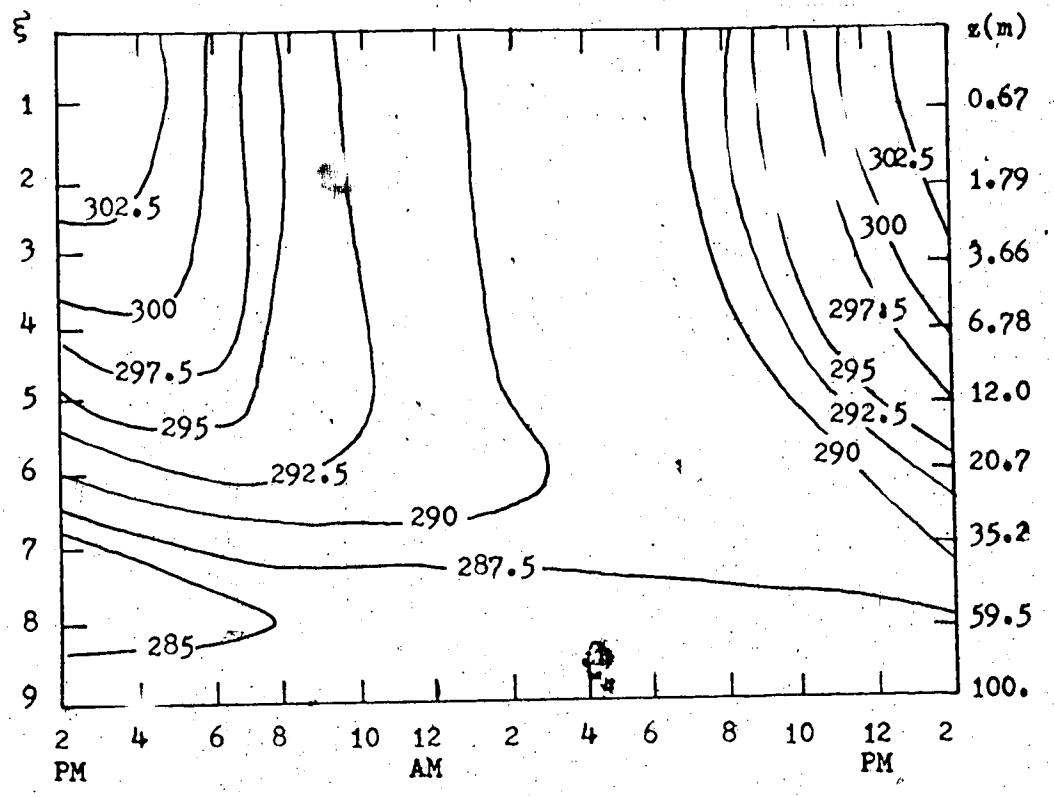

Figure 51. Diurnal variation of the soil temperature profile for the case z_o = 1 cm, V_g = 20 m/sec and high soil conductivity. The units are [°K].

are not perfectly cyclical. The second-day maximum is higher than that of the first day due to the decreased soil heat flux from one day to the other. The surface temperature could be lowered by modifying either the transmissivity factor or the albedo. In this way we could obtain more cyclical diurnal variations within the soil layer.

We now compare a poorly-conductive soil with a good-conductive one. The poorly-conductive soil has:

1- a larger temperature variation in the upper layers.

2- A smaller temperature variation in the lower layers.

3- The time lag between the maximum or minimum temperature in the upper levels and the lower levels is considerably increased.

All these differences are expected because we expect that the temperature wave will not penetrate a poorly-conductive soil as deeply as it would a good-conductive soil. This tends to concentrate the temperature gradients very close to the surface in the case of a poorly-conductive soil.

There is almost no difference between the soil temperature profiles due to a change in roughness height. The temperatures are slightly warmer in the case of z_o = 1 cm. A detailed calculation of the soil heat flux during the period 8 PM to 2 AM shows that the heat flux from the soil is about 10% higher with z_o = 100 cm. Therefore, the atmospheric heat flux and the soil heat flux are both larger overnight in the case of z_o = 100 cm, which should give a warmer surface temperature in this case. The number of iterations taken by the model with z_o = 100 cm was approximatively 2 to 3 times the number of iterations required by the model with z_o = 1 cm. This seems to have caused a significant difference in the convergence

Table 5. Comparison of the surface potential temperature between the four simulations of the urban heat island.

parameter \ model #	1	2	3	4
minimum $\Theta(z_o)$	289.5911	292.5137	287.9182	292.5120
maximum $\Theta(z_o)$	311.9797	310.2654	309.2634	330.2451
time of minimum	4^{40} AM	4^{40} AM	4^{50} AM	4^{40} AM
time of maximum	2^{20} PM	2^{30} PM	2^{50} PM	2^{20} PM
minimum $\overline{w\theta}(z_o)$	-3.54	-8.27	-5.49	-4.38
maximum $\overline{w\theta}(z_o)$	5.50	11.3	6.97	5.80
time of minimum	8 PM	7^{40} PM	7^{40} PM	8 PM
time of maximum	11^{20} AM	12^{20} PM	12^{40} PM	11^{40} PM
time of $\overline{w\theta}(z_o) = 0$	6 AM	7 AM	6 AM	5^{35} AM
	4^{10} PM	4^{20} PM	3^{50} PM	3^{40} PM
Surface warming rate:				
minimum	-3.3	-2.9	-3.2	-6.0
maximum	4.0	2.9	3.7	6.4
time of minimum	6^{50} PM	6^{50} PM	7^{10} PM	6^{20} PM
time of maximum	8^{50} AM	9^{30} AM	9^{30} AM	9^{30} AM
z_o [cm]	1	1	100	1
V_g [m/sec]	10	30	10	10
soil conductivity	high	high	high	low

of the surface temperature for both simulations. The model usually converged without any oscillation when we used OMEGA = 0.7, which increases the probability of a build-up of systematic errors as is the case here.

6.4 Assessment of the Urban Heat Island Effect.

We compare the quantities related to the behavior of the surface temperature for the four simulations in Table 5. Usually the city has a larger roughness height than the surrounding countryside. The city has also a higher soil thermal conductivity because of the abundance of concrete in the city and also because of the fact that clay, a poor thermal conductor, is often present in the countryside. Therefore, we expect a smaller diurnal amplitude over the city because of the increases in roughness height and soil thermal conductivity. The results seem to indicate that the countryside would be warmer than the city during daytime. However, another major factor counteracts the strong effect of the soil thermal conductivity: evaporation. There is generally a very important decline in evaporation over the city. This permits a large part of the solar energy to go into latent heat over the countryside. The difference in evaporation between the city and the countryside needed in order to obtain a warmer city depends mainly on the differences in the soil properties.

When the effects of evaporation and soil thermal properties nearly balance each other, the influence of other factors may become important in a specific case when we wish to determine which of the city or the countryside will become warmer during the daytime. The 99 cm

increase in roughness height cools down the city by 2 °C during daytime. The influence of an increase in the geostrophic wind is to reduce the amplitude of the diurnal temperature cycle and consequently to reduce the urban heat island effect in absolute value.

There is nc significant difference in the times of maximum and minimum temperatures for all four simulations. However, the time of change in stability in the lower atmosphere is retarded by strong winds and by high soil conductivity.

CONCLUSION

A numerical model using a more sophisticated approach to turbulence modelling than the ordinary K-theory has been applied with some success to the problem of the urban heat island. The unidimensional model basically describes the interaction between a soil layer and an atmospheric layer. Three factors were examined: roughness height, soil conductivity and wind speed. The model has demonstrated that the soil conductivity was an extremely important factor in determining the amplitude of the diurnal temperature cycle. The maximum temperature was considerably increased over a poorly conductive soil, which is often found in the countryside. Increased roughness height also reduced the amplitude of the diurnal temperature wave by a small amount. When we associate a high roughness height and a high soil conductivity with a city, we are led to the conclusion that the city is considerably cooler than the countryside during the daytime. The counterbalancing effect which was not studied is the difference in evaporation between the city and the countryside. If we suppose a dry city and a moist countryside, we expect that the daytime rural temperature will be cooler.

Many problems are associated with the numerical solution of the equations. An implicit finite-difference scheme was used in order to provide numerical stability and to permit a time step of 10 minutes. The equations have to be written very carefully in finite-difference form in order to reduce the round-off errors to which the temperature computations are very sensitive in the upper boundary layer. Double

precision had to be used for the mean quantities in order to obtain reasonable profiles above 1000 m. In some cases systematic errors have built up due to insufficient accuracy in the iterative procedure within each time step. The accuracy which we need in order to obtain good results must be determined by trial and error. The disadvantage of requiring more accuracy is the increase in computing time.

The most obvious improvement to the model is to include the moisture computations which present a few supplementary problems. We need a balance equation between the soil and atmospheric moisture. There is also the problem of water vapor build-up in the atmosphere. The main source of water vapor in the boundary layer is the evaporation at the surface which is enhanced during daytime. The water vapor is also transported fairly high in the atmosphere under unstable lapse rates. However, the main sink of water vapor is not the overnight condensation at the surface which involve only a shallow layer close to the ground under stable conditions. The main sink is the formation of clouds and precipitation. Therefore, we would need to incorporate some cloud physics into the model or we could remove artificially any excess water. If we include condensation in the atmosphere, we have to introduce a source term in the equation of temperature due to the release of latent heat. This would imply also a modification of the solar energy received at the surface of the earth due to reflection by the clouds and to absorption within the cloud. The infrared balance would also be affected.

Other improvements may include an albedo model which permits

a diurnal variation of the albedo with the solar angle. Radiative flux divergence could be important in the lowest 100 m over a city. The disadvantage of the roughness height concept over a city is that the value associated with very dense and tall buildings is of the order of a few meters. Therefore, we do not model the lowest meters over the city although often this is the layer in which we are interested. We could use two- and three-dimensional models in which some care has to exercised in order to model properly the change in roughness height. As pointed out earlier, the forced-convection parameterization of some of the turbulent quantities gives a different result than the one predicted in the free-convection limit. Therefore, we must reconcile the two points of view. We would also like to model more complex soil layers in which the amount of water influences greatly the soil conductivity. Also, we could investigate the effects of two or more types of soil layers superposed one upon another.

REFERENCES

Angle, R.P., 1973: Airflow Modification due to a Change in Surface Roughness. M. Sc. thesis, University of Alberta, 130 pp.

Atwater, M.A., 1966: Comparison of numerical methods for computing radiative temperature changes in the atmospheric boundary layer. J. Appl. Meteor., 5, 824-831.

Bornstein, R.D., 1968: Observations of the urban heat island effect in New York City. J. Appl. Meteor., 7, 575-582.

Brooks, D.L., 1950: A tabular method for the computation of temperature change by infrared radiation in the free atmosphere. J. Meteor., 7, 313-321.

Businger, J.A., 1972: The atmospheric boundary layer. Chapter 6, Remote Sensing of the Troposphere, U.S. Dept. of Commerce (Superintendent of Documents, Govt. Printing Office).

Businger, J.A., J.C. Wyngaard, Y. Izumi and E.F. Bradley, 1971: Flux profile relationships in the atmospheric surface layer. J. Atmos. Sci., 28, 181-189.

Craig, C. and W. Lowry, 1972: Reflections on the urban albedo. Preprint of the Conference on Urban Environment and Second Conference on Biometeorology, 77-82.

Deardorff, J.W., 1973: Three-dimensional numerical modeling of the planetary boundary layer. Workshop on Micrometeorology, A.M.S., 271-311

Donaldson, C. duP., 1973: Construction of a dynamic model of the production of the atmospheric turbulence and the dispersal of atmospheric pollutants, Workshop on Micrometeorology. A.M.S., 313-390.

Duckworth, F.S. and J.S. Sandberg, 1954: The effects of cities upon horizontal and vertical temperature gradients. Bull. Amer. Meteor. Soc., 35, No: 5, 198-207.

Dufort, E.C. and S.P. Frankel, 1953: Stability conditions in the numerical treatment of parabolic differential equations. Math. Tables Aids Comput., 7 , 135-152.

Elliot, W.P. and D.W. Stevens, 1961: A numerical method for computing radiative temperature changes near the earth's surface. GRD Research Notes, No. 69, L.G. Hanscom Field, Bedford, Mass., 21 pp.

Eskinazi, S. and F.F. Erian, 1969: Energy reversal in turbulent flows. Phys. Fluids, 12, 1988-1998.

Estoque, M.A., 1973: Numerical modeling of the planetary boundary layer. Workshop on Micrometeorology. A.M.S., 217-269.

Godson, W.L., 1958: Atmospheric Thermodynamics. Research and Training Division, Meteor. Branch, D.O.T, Toronto, 117 pp.

Hales, J.V., W. Zdunkowski and D. Henderson, 1963: A study of the physical thermodynamical and dynamical causes of low ceilings and visibilities. Final Rpt, Contract AF19(604)-7333 (DDC NO AD423535), Inter-Mountain Weather Inc., Salt Lake City, 77 pp.

Haltiner, G.J., and F.L. Martin, 1957: Dynamical and Physical Meteorology. New York, McGraw-Hill, 74-156.

Hanjalic, K. and B.E. Launder, 1972: Fully developed asymetric flow in a plane channel. J. Fluid Mech., 52, 609-638.

Hage, K.D., 1972: Nocturnal temperatures in Edmonton, Alberta. J. Appl. Meteor., 11, 123-129.

Hage, K.D., 1975: Urban-rural humidity differences. J. Appl. Meteor., 14, 1277-1283.

Howard, L., 1833: The Climate of London Deduced from Meteorological Observations Made in the Metropolis and at Various Places Around it. 2nd ed., 3 vols. London, J. and A. Arch.

Kolmogoroff, A.N., 1942: The equations of turbulent motion in an incompressible fluid. Izv. Akad. Nauk. SSSR, Ser. Fiz., 6, No 1,2, 56-58.

Kuo, H.L., 1968: The thermal interaction between the atmosphere and earth and the propagation of diurnal temperature waves. J. Atmos. Sci., 25, 682-702.

Landsberg, H.E., 1956: The Climate of Towns. Man's Role in Changing the Face of the Earth, Univerity of Chicago Press, 1193 pp.

Lilly, D.K., 1967: The representation of small-scale turbulence in numerical simulation experiments. Proc. IBM Sci. Comput. Symp. Environmental Sci., IBM Form No. 320-1951, 195-210.

McElroy, J.L., 1972: Effects of alternate land-use stategies on the structure of the nocturnal urban boundary layer. Preprint of the Conference on Urban Environment and Second Conference on Biometeorology, 185-190.

Mellor, G.L., 1972: The large Reynolds number asymptotic theory of turbulent boundary layers. Intern. J. Eng. Sci., 11, 851-873.

Mellor, G.L., 1973: Analytic prediction of the properties of stratified planetary surface layers. J. Atmos. Sci., 30, 1061-1069.

Mellor, G.L. and H.J. Herring, 1968: Two methods of calculating turbulent boundary layer behavior based on numerical solutions of the equations of motion. Proc. AFOSR-IFF Stanford Conference, Vol. 1, 331-345.

Mellor, G.L. and H.J. Herring, 1973: A survey of mean turbulent field closure models. AIAA J., 11, 590-599.

Mellor, G.L. and T. Yamada, 1974: A hierarchy of turbulence closure models for planetary boundary layers. J. Atmos. Sci., 31, 1791-1806.

Meroney, R.N., 1974: Buoyancy effects on a turbulent shear flow. Symposium on Atmospheric Diffusion and Air Pollution.

Miller, E.L., R. Johnson and W.P. Lowry, 1972: The case of the muddled metromodel. Preprint of the Conference on Urban Environment and Second Conference on Biometeorology, 77-82.

Mitchell, J.M., 1961: The temperature of cities. Weatherwise, 14, 224-229.

Monin, A.S. and A.M. Yaglom, 1971: Statistical Fluid Mechanics: Mechanics of Turbulence. The MIT Press, 769 pp.

Myrup, L.O., 1969: A numerical model of the urban heat island. J. Appl. Meteor., 8, 908-918.

Nappo, C.J., 1972: A numerical study of the urban heat island. Preprint of the Conference on Urban Environment and Second Conference on Biometeorology, 1-4.

Ohmstede, W.P., 1966: Numerical solution of the transport and energy equations in the planetary boundary layer. Tech. Rpt ECOM-6020, U.S. dept of Commerce.

Oke, T.R. and G.B. Maxwell, 1975: Urban heat island dynamics in Montreal and Vancouver. Atmos. Envir., 9, 191-200.

Roden, G.I., 1966: A Modern statistical analysis and documentation of historical temperature records in California, Oregon and Washington, 1821-1964. J. Appl. Meteor., 4, 3-24.

Rotta, J.C., 1951: Statistische Theorie nichthomogener Turbulenz. Z. Phys., 129, 547-572; 131, 51-77.

Sundborg, A., 1951: Climatological studies in Uppsala, with special regard to temperature conditions in the urban area. Geographica, No. 27, Universitet Geografiska Instituten, Uppsala, 111 pp.

Taylor, P.A. and Y. Delage, 1972: A note on finite-difference schemes for the surface and planetary boundary layers. Bound. Layer Meteor., 2, 108-121.

Taulbee, D., 1973: private communication to Deardorff (1973).

APPENDIX A

LOG-LINEAR ATMOSPHERIC GRID

As explained in Chapter III the best transformation of coordinates in the lower boundary layer is,

$$\varphi = AC\left\{ \ln\left[(z+z_o)/z_o\right] /k_o+z/ \ell_o\right\} \qquad (A.1)$$

where, φ = log-linear coordinate

z = ordinary vertical coordinate (cm) with origin at z_o

z_o = roughness height

k_o = von Karman's constant

ℓ_o = length fixing the maximum size of the eddies

AC = constant chosen for our convenience.

The grid is defined by the following statements,

- The maximum number of φ levels is 40
- φ and z are zero at z_o
- the top of the boundary layer is at 3000 m and correspond to $\varphi = 39$
- the number of grid-points is fixed at 40 and the index k representing the height of the grid-point is related to $k = \varphi + 1$.

The constant AC is determined when we assign a value to z_o and ℓ_o.

$$AC = \frac{39}{\left[\frac{1}{k_o} \ln\left(\frac{300000+z_o}{z_o}\right) + \frac{300000}{\ell_o}\right]} \qquad (A.2)$$

During the transformation of coordinates various derivatives of φ with respect to z appear; these derivatives can be derived exactly from equation (A.1).

$$\frac{\partial \psi}{\partial z} = AC\left[\frac{1}{k_o(z+z_o)} + \frac{1}{\ell_o}\right] \qquad (A.3)$$

$$\frac{\partial^2 \psi}{\partial z^2} = -\frac{1}{k_o(z+z_o)^2} \qquad (A.4)$$

Therefore we only have to solve the equation for z at each ψ level. There are three iterative ways of solving (A.1) for z.

Method 1. Near z_o the grid is almost logarithmic because of the small contribution from the linear term in that region. The most rapidly converging formula is obtained by isolating the term inside the logarithm,

$$z = z_o\left\{\exp\left[k_o(\psi/AC - z/\ell_o)\right] - 1\right\} \qquad (A.5)$$

Method 2. Near the top of the boundary layer the grid is almost linear because the logarithmic term has a small influence there. Therefore we isolate the linear term,

$$z = \ell_o\left\{\psi/AC - \ln\left[(z+z_o)/z_o\right]/k_o\right\} \qquad (A.6)$$

Method 3. If formulas (A.5) and (A.6) do not give reasonable results we can use formula (A.1) and do the iteration on ψ instead of on z. In this case we readjust the value of z until we get close enough to the integral value for a given level.

A.1 Determination of IKM.

Firstly we replace ψ by $k = \psi + 1$ because most computing systems do not accept an index 0. The level IKM is the level representing the upper limit of the applicability of (A.5). Close to the roughness height the initial guess will be purely exponential,

$$z_i = z_o\left\{\exp\left[(k_o-1)/AC\right] - 1\right\} \qquad (A.7)$$

where, z_i = initial guess for z.

The initial guess is always greater than the true value for z because we have neglected a negative number in the exponential, namely $-z_i/\ell_o$. At some level the initial value of z will be large enough to cause the term inside the exponential in (A.5) to become negative: that level can be considered as the first one where the exponential initialization is inappropriate. Therefore, IKM is the level immediately below the first level where,

$$(k-1)/AC - z_i/\ell_o < 0$$

A.2 Initialization of the Other Levels.

We use the assumption of a linear spacing to initialize all the other levels,

$$z_i = \varphi * (\text{top of the B.L.})/(\text{maximum } \varphi) = (k-1)*300000/39 \quad (A.9)$$

That initial guess is very good for the top levels where the spacing is indeed almost linear but there is a critical region where neither the exponential spacing nor the linear spacing is expected to be good. One way of determining that region is to input z_i into (A.6) in order to get a second guess z',

$$z' = \ell_o\left\{\varphi/AC - \ln\left[(z_i+z_o)/z_o\right]/k_o\right\} \quad (A.10)$$

The overestimation in z_i in the lower levels can cause z' to become negative which would stop the iterative procedure because the next guess would require the estimation of a logarithm of a negative number. Therefore, each time that z' is negative we readjust z_i to a smaller number

$$z_i' = z_i/B \quad (A.11)$$

where B is a positive constant greater than 1.

A.3 Accelerated Gauss-Seidel Process.

We use the accelerated Gauss-Seidel process which consists in refining our initial guess by giving a weight both to the last approximation and to the new computed value. For example, we call,

Z = last value of z

TEMP = computed value for z

TP = TEMP - Z = difference between two successive iterative values of z

Z' = Z + TP OMEGA = new approximation to z

OMEGA is an acceleration factor which gives a weight both to Z and TEMP. It can vary from 0 to 2 and,

OMEGA = 1 implies that the computed value of z is TEMP.

OMEGA > 1 implies acceleration, appropriate for the cases in which Z' approaches a value steadily without oscillations.

OMEGA < 1 implies deceleration, appropriate for the cases where Z' oscillates around the real value of z.

Unfortunately it does not seem possible to devise a general formula for the optimum value of OMEGA in our problem. Some of the difficulties are,

(a) close to z_o, OMEGA = 1 is fairly appropriate because the oscillations around the real value are damped very rapidly,

(b) Near IKM large oscillations prevail due to the fact that the initial guess is poor in that region and also that neither (A.5) nor (A.6) are really appropriate there.

(c) The level IKM is dependent on the roughness height z_o and to a lesser extent on λ_o.

(d) Above IKM the iterative formula changes and most of the diffi-

culties arise near IKM where OMEGA < 1 is needed for convergence. Near the top of the boundary layer the convergence is rather rapid with OMEGA=1.

A.4 Detailed Analysis of OMEGA in a Specific Case.

With OMEGA = 1 two successive iterations will always give one value above and the other one below the actual value of z. This phenomenon is due to the form of the equations. When the formulas are applied in their appropriate regions the oscillations are damped very rapidly. It would be difficult to determine the best OMEGA a priori for all the grid points. However, after the solution has been obtained we can compute what the best OMEGA should have been. The best OMEGA is defined by

$$\text{OMEGA}' = (Z'-Z)/(\text{TEMP}-Z)$$

where, Z' = actual height of the grid point

Z = last iterative value for z.

The best OMEGA is therefore defined as the one which would give the true value in only one iteration. We will study OMEGA in the special case where $z_o = 1$ cm and $\ell_o = 2700$ cm. In this case we find that AC = 0.2650463308. In Tables 6 and 8 we list the computed values of the grid-point heights at various stages of iteration. In Tables 7 and 9 we have tabulated the computed best OMEGA at all stages of iteration.

A.4.1 Analysis of the Iterative Process Below IKM.

We note that the initialization is extremely good close to the ground and worsens considerably near IKM where the initial value

Table 6. Computed values for the grid-point heights z(k) at various stages of iteration. The first entries in each columns are the initial values for which fomula (A.4) was used. The successive values are computed from (A.5). The levels are in terms of k = ℓ + 1.

z(2)	z(3)	z(4)	z(5)	z(6)
2.745382866	13.02789281	51.53982937	195.78177670	736.0339460
2.744050185	13.00422248	51.18997609	190.08504693	674.9963432
2.744050832	13.00426545	51.19234303	190.09731477	674.8039290
2.744050831	13.00426538	51.19232702	190.09700948	674.2916315
		51.19232713	190.09701708	674.3364784
			190.09701689	674.3325524
				674.3328961
				674.3328660
				674.3328686
				674.3328684

z(7)	z(8)	z(9)
2760.433670	10337.88097	38723.06763
1929.065229	2705.932184	255.8352926
2148.690295	7279.085837	37258.92336
2088.351785	4023.201229	300.3897878
2104.758060	6136.303980	37243.19405
2101.284420	4665.759005	308.9370814
2101.230814	5645.811378	37201.95099
2101.245422	4972.118966	310.5985422
2101.241441	5425.952268	37193.93929
2101.242526	5115.893194	310.9235327
2101.242311	5325.744693	37192.37819
2101.242289	5182.995555	310.9854507
2101.242295	5279.748775	37192.07383
2101.242293	5213.794914	310.9977602
	5258.570325	37192.01448
	5228.131046	311.0001605
	5248.805082	37192.00291
	.	.
	.	311.0007420
	5240.437109	37192.00009

Table 7. Best OMEGA corresponding to the computed values of the grid points at various stages of iteration.

z(2)	z(3)	z(4)	z(5)	z(6)
0.99390	0.9981	0.99327	0.9978	0.9198
0.99845	0.9983	0.99328	0.9957	0.91948
0.999			0.9957	0.91951
				0.91991

z(6)	z(7)	z(9)
0.792898	0.6679	
[illegible]	0.5542	
[illegible]	0.6261	
[illegible]	0.5760	0.2695
[illegible]	0.6092	0.7305
[illegible]	0.58637	0.2695
0.83	0.60172	0.7305
0.72	0.59122	
	0.59822	
	0.5934	
	0.5967	

Table 8. Computed values of the grid-point heights z(k) at various stages of iteration. We have used formula (A.10) for the initial values (first entry in each column) and formula (A.6) for the other values.

z(10)	z(11)	z(12)	z(13)	z(14)	z(15)
75000.0000	82500.0000	90000.0000	97500.0000	105000.000	112500.000
9087.24000	14538.9041	24054.5795	33624.0000	43239.2259	52893.8983
25843.0580	27930.2370	34233.2230	41836.5800	50083.3298	58715.5240
13306.2064	22893.9750	31511.1692	40150.8100	48949.8161	57910.0400
18426.7500	24487.7900	32150.3100	40468.0000	49098.6320	58016.6000
15915.3529	23927.5590	31995.4144	40407.3700	49102.9959	58002.4190
17045.5800	24087.1600	32032.6700	40418.9500	49102.3103	58004.3050
16516.3606	24035.8800	32025.6900	40416.7400	49102.4180	58004.0544
16759.6509	24052.3200	32025.8500	40417.1640	49102.4011	58004.0877
16646.8531	24047.0400	32025.3300		49102.4037	58004.0833
16698.9450	24048.7400	32025.4599		49102.4033	58004.0839
16674.8443	24048.1970	32025.4291		49102.4034	
16685.9853	24048.3718				
16680.0833	24048.3160				
.	24048.3339				
.	24048.3281				
.	24048.3303				
16682.5					

Table 9. Best OMEGA corresponding to the computed grid-point heights at some of the iteration steps.

z(10)	z(11)	z(12)	z(13)	z(14)	z(15)
0.8340	0.8600	0.879	0.8930	0.865	0.882
0.5586	0.7100	0.783	0.8270		
0.7306	0.7700	0.811	0.8421		
0.6590	0.7526		0.8419		
0.6945	0.7585				
0.6780					
0.6860					

is too large by a factor of 3. The number of iterations rises from 3 at the second grid point to 10 at the sixth grid point, jumps to 60 at the eighth grid point and would never converge at IKM = 9 because there is an oscillation between two stable values at this grid point. Examining the values of OMEGA at various stages of iteration, we observe that a different value for OMEGA is needed depending on whether we start from below the actual value or from above. This phenomenon peaks at IKM where the iteration process breaks down if we used OMEGA = 1. At IKM it converges to one value above the actual value for z and to another value below the actual value for z. This points out that there is no guarantee of an unique answer with this iteration process. In fact there are three solutions to the equation for ℓ : one using the lowest value for z in the linear term and the highest one in the logarithmic term, another one using the lowest value for z in the logarithmic term and the highest one in the linear term, and finally one using the actual value for z in both terms. Obviously we are interested only in the last solution. The only iteration process which would give an unique answer all the time is the one on ℓ, but this is generally a fairly slow process and difficult to implement. Now we will try to derive an analytical function which will give the best OMEGA at all levels below IKM. The matching can be done with the help of the following rules,

(a) exact match of OMEGA = 1 at k = 1.

(b) Match the lowest value for OMEGA at IKM, i.e. OMEGA = 0.2695.

(c) Assume an exponential variation of OMEGA in terms of k.

Therefore, we will use an expression like,

$$\text{OMEGA}(k) = 1 + A\left\{1-\exp\left[(k-1)/(\text{IKM}-1)\right]^{n}\right\} \qquad \text{(A.12)}$$

where A and n are constants to be determined by fitting the actual values found for OMEGA at various grid points. Good values for these constants were found to be,

$$A = 0.425 \qquad \text{(A.13)}$$

$$n = 3 \qquad \text{(A.14)}$$

It is obvious that this formula will not be perfect for all roughness heights because of the arbitrariness in the choice of IKM and the discreteness of the levels which affect the efficiency of (A.5) at IKM. However, it is clear that an uniform value for OMEGA at all levels is not acceptable. A value of 1 would not give convergence to the desired value at IKM, whereas a value of 0.3 would increase considerably the number of iterations required at the grid points where convergence is rapid with OMEGA = 1. Formula (A.12) seems a fair compromise between simplicity, generality and speed of convergence.

A.4.2 Analysis of the Iterative Process Near and Above IKM.

It takes many more iterations near IKM than much above that level. We also note that the initialization improves as the level of the grid point increases. In this case the best OMEGA varies more gently above IKM than below it. Therefore, we try to fit an analytical expression of the form,

$$\text{OMEGA}(k) = 1 - B\,(NS-k)/(NS-IKP)^{x} \qquad \text{(A.15)}$$

where, NS = top of the boundary layer = 40

IKP = IKM + 1

x = exponent determined to be about 5

B = constant determined to be about 0.32.

A.5 Iteration Process on φ

In the cases where (A.5) nor (A.6) have not converged within the specified number of iterations, we can complete the process by the iteration on φ which uses (A.1) in the form,

$$\varphi' = AC\left\{\ln\left[(z'+z_o)/z_o\right]/k_o + z'/\ell_o\right\} \qquad (A.16)$$

If we define DIFF $= \varphi' - \varphi$. Then, when DIFF is positive, the implication is that z' is too high and similarly, when DIFF is negative, z' is too low. Therefore, the next guess will be,

$$z'' = z' - f(DIFF) \qquad (A.18)$$

where f(DIFF) is a positive function involving DIFF. This function has to be determined empirically and will probably vary from grid point to grid point.

APPENDIX B

STEADY-STATE ATMOSPHERIC EQUATIONS

B.1 Equations: First Form.

The basic equations in log-linear coordinates are given in Section 3.3.1 and simplify to,

$$\frac{\partial^2 U}{\partial y^2} K_m \left(\frac{\partial y}{\partial z}\right)^2 - \frac{\partial U}{\partial y}\left(\frac{\partial K_m}{\partial y}\left(\frac{\partial y}{\partial z}\right)^2 + K_m \frac{\partial^2 y}{\partial z^2}\right) = f(V - V_g) \qquad (B.1)$$

$$\frac{\partial^2 V}{\partial y^2} K_m \left(\frac{\partial y}{\partial z}\right)^2 - \frac{\partial V}{\partial y}\left(\frac{\partial K_m}{\partial y}\left(\frac{\partial y}{\partial z}\right)^2 + K_m \frac{\partial^2 y}{\partial z^2}\right) = f(U_g - U) \qquad (B.2)$$

$$\frac{1.15}{3}\left(\left(\ell \left(\frac{\partial y}{\partial z}\right)^2\right)\frac{\partial^2 e^2}{\partial y^2} + \left(\frac{\partial e\ell}{\partial y}\left(\frac{\partial y}{\partial z}\right)^2 + e\ell \frac{\partial^2 y}{\partial z^2}\right)\frac{\partial e^2}{\partial y}\right) = 2\left(K_m \left|\frac{\partial \vec{V}}{\partial y}\right|^2 \left(\frac{\partial y}{\partial z}\right)^2 - \frac{e^3}{B_1 \ell}\right) \qquad (B.3)$$

The diffusion operator $\mathcal{D}(\ )$ is defined in (3.30) and used in the equation for K_m,

$$K_m = \frac{A_1' \ell \left((1 - 3C_1)e^3 + 0.23 \times 4 A_1 \ell \mathcal{D}(e^2)\right)}{e^2 + 6 A_1^2 \ell^2 \left|\frac{\partial \vec{V}}{\partial y}\right|^2 \left(\frac{\partial y}{\partial z}\right)^2} \qquad (B.4)$$

The other coefficients of diffusivity are not used in the computations but can be evaluated diagnostically,

$$K_t \doteq K_w = \frac{A_1 \ell \left(e^3 + 4 \times 0.23\, A_1 \ell \mathcal{D}(e^2) - 6 A_1 \ell K_m \left|\frac{\partial \vec{V}}{\partial y}\right|^2 \left(\frac{\partial y}{\partial z}\right)^2\right)}{e^2} \qquad (B.5)$$

The other turbulent moments involving θ or q vanish,

$$\overline{\theta^2} = \overline{\theta q} = \overline{q^2} = 0 \qquad (B.6)$$

The mean mixing ratio and the mean potential temperature are assumed constant throughout the boundary layer and their actual values

are determined by their values at the surface of the earth.

B.2 Mixing Length.

The formula for the mixing length is,

$$\ell = \frac{k_o(z+z_o)}{1 + \frac{k_o(z+z_o)}{\ell_o}} \qquad (B.7)$$

where ℓ_o is defined by,

$$\ell_o = 0.1 \frac{\int_o^\infty z\, e\, dz}{\int_o^\infty e\, dz} \qquad (B.8)$$

These integrals are transformed into finite summations by,

$$\int_o^\infty z\, e\, dz = \int_o^\infty z\, e\, \frac{dz}{d\varphi}\, d\varphi = \sum_{k=1}^{n} z(k)\, e(k)/DELZ(k) \qquad (B.9)$$

$$\int_o^\infty z\, dz = \int_o^\infty z\, \frac{dz}{d\varphi}\, d\varphi = \sum_{k=1}^{n} z(k)/DELZ(k) \qquad (B.10)$$

Now we look at the vertical derivative of ℓ. In the surface layer ℓ varies exponentially in φ-coordinates. A simple centered finite [redacted] approximation like,

$$\left.\frac{\partial \ell}{\partial \varphi}\right|_k \approx \frac{\ell(k+1) - \ell(k-1)}{2}$$

would have a large truncation error. Therefore, we will use a more exact formulation obtained by taking the derivative of (B.7) with respect to φ.,

$$\left.\frac{\partial \ell}{\partial \varphi}\right|_k = DELZZ(k)/\ell^2(k) \qquad (B.11)$$

where

$$DELZZ(k) = -\left.\frac{\partial^2 \varphi / \partial z^2}{AC \cdot \partial \varphi / \partial z}\right|_k \qquad (B.12)$$

B.3. Vertical Derivative of K_m.

As we know, in the surface layer K_m behaves like,

$$K_m = u_* k_o(z+z_o) \qquad (B.13)$$

The grid is predominantly logarithmic in that region, which implies,

$$\varphi \propto \ln[(z+z_o)/z_o] \qquad (B.14)$$

Therefore,

$$K_m \propto \exp(\varphi) \text{ and} \qquad (B.15)$$

$$\frac{\partial K_m}{\partial \varphi} \propto \exp(\varphi) \qquad (B.16)$$

Therefore, a simple finite-difference approximation to the vertical derivative of K_m,

$$\frac{\partial K_m}{\partial \varphi} = \frac{K_m(k+1)-K_m(k-1)}{2} \qquad (B.17)$$

will be greatly in error in the lower boundary layer. The following transformation corrects the problem:

$$\frac{\partial K_m}{\partial \varphi} = K_m \frac{\partial \ln K_m}{\partial \varphi} \qquad (B.18)$$

This is better in the surface layer because

$$\ln K_m \propto \varphi \text{ and} \qquad (B.19)$$

$$\frac{\partial \ln K_m}{\partial \varphi} \propto \text{constant} \qquad (B.20)$$

The finite-difference approximation in the lower boundary layer should be

$$\frac{\partial K_m}{\partial \varphi} = \frac{K_m(k)}{2} \ln[(K_m(k+1)/K_m(k-1)] \qquad (B.20)$$

B.4 Finite-Difference Equations.

B.4.1 Mean Wind U.

The appropriate equation for U is (B.1) in which the various terms are approximated by,

$$2\left.\frac{\partial K_m}{\partial \eta}\right|_k = DLNK = \begin{cases} K_m(k+1) - K_m(k-1) & \text{above the constant-flux layer} \\ K_m(k)\,\ln\left[\dfrac{K_m(k+1)}{K_m(k-1)}\right] & \text{in the constant-flux layer} \end{cases} \quad (B.21)$$

$$A(2) = \frac{\partial K_m}{\partial \eta}\left(\frac{\partial \eta}{\partial z}\right)^2 + K_m\frac{\partial^2 \eta}{\partial z^2} = DLNK\ DELZ2(k)/2 + K_m(k)\ DEL2Z(k) \quad (B.22)$$

$$A(3) = K_m\left(\frac{\partial \eta}{\partial z}\right)^2 = K_m(k)\ DELZ2(k) \quad (B.23)$$

$$A(4) = \frac{\partial U}{\partial \eta} = \left[U(k+1) - U(k-1)\right]/2 \quad (B.24)$$

$$\frac{\partial^2 U}{\partial \eta^2} = U(k+1) - 2\,U(k) + U(k-1) \quad (B.25)$$

We group all the terms different from U(k),

$$DU = \left[U(k+1) + U(k-1)\right]\ A(3) + A(4)\ A(2) + F\ (V(k) - V_g) \quad (B.26)$$

Finally,

$$U(k) = DU/[2\ A(3)] \quad (B.27)$$

B.4.2 Equation for the Mean Wind V.

The terms A(2) and A(3) will be used also in the equation for V. The other terms are

$$A(5) = \frac{\partial V}{\partial \eta} = \left[V(k+1) - V(k-1)\right]/2 \quad (B.28)$$

$$\frac{\partial^2 V}{\partial \eta^2} = V(k+1) - 2\,V(k) + V(k-1) \quad (B.29)$$

All the terms except V(k) are grouped into,

$$DV = \left[V(k+1) + V(k-1)\right]\ A(3) + A(5)\ A(2) - F\left[U(k) - U_g\right] \quad (B.30)$$

Therefore,

$$V(k) = DV/[2\ A(3)] \qquad (B.31)$$

B.4.3 Equation for e.

The equation for e is (B.3) in which we have to evaluate the vertical derivative of $(e\,\ell)$:

$$\frac{\partial\, e\ell}{\partial y} = e\,\frac{\partial \ell}{\partial y} + \ell\,\frac{\partial e}{\partial y} \qquad (B.32)$$

We will use a simple centered finite-difference approximation to the vertical derivative of e such that

$$\frac{\partial e}{\partial y} = [e(k+1) - e(k-1)]/2 \qquad (B.33)$$

The vertical derivative of ℓ is given by (B.11) and will be called DL(k). Therefore, (B.32) can be written as

$$DEL = e(k)\ DL(k) + \ell(k)\,[e(k+1)-e(k-1)]/2 \qquad (B.34)$$

The coefficient of $2\,\frac{\partial e^2}{\partial y}$ becomes

$$A(14) = (DEL\ DELZ2(k) + e(k)\,\ell(k)\ DEL2Z(k))\ 0.23/2 \qquad (B.35)$$

The coefficient of $\frac{\partial^2 e^2}{\partial y^2}$ is

$$A(13) = e(k)\,\ell(k)\ DELZ2(k)\ 0.23 \qquad (B.36)$$

We call

$$A(8) = \left|\frac{\partial \vec{V}}{\partial z}\right|^2 = \left[\left(\frac{\partial U}{\partial z}\right)^2 + \left(\frac{\partial V}{\partial z}\right)^2\right] = [A(4)\ A(4) + A(5)\ A(5)]\ DELZ2(k) \qquad (B.37)$$

We isolate the terms in $e^2(k+1)$ and those in $e^2(k-1)$ and call AA and AB their respective coefficients,

$$AA = A(13) + A(14) \qquad (B.38)$$

$$AB = A(13) - A(14) \qquad (B.39)$$

Gathering all the terms except $e^2(k)$, we have

$$A(16) = e^2(k+1)\ AA + e^2(k-1)\ AB + 1.2\ K_m(k)\ A(8) \quad (B.39)$$

Finally we obtain

$$e^2(k) = A(16)/A(15) \quad (B.40)$$

$$e(k) = SQRT[e^2(k)] \quad (B.41)$$

B.4.4 Equation for K_m.

The array B contains most of the commonly-used variables which do not need to be computed each time that the program is run. In this case we have

$$B(28) = (1-3C_1) \quad (B.42)$$

$$B(61) = 3\ A_1^2 \quad (B.43)$$

$$B(5) = A_1 \quad (B.44)$$

The diffusion operator applied to e^2 is called A(9) where

$$A(9) = 4\ A_1 \ell\ D_1(e^2) = B(31)\ \ell(k)\ [AA\ e^2(k+1) + AB\ e^2(k-1) - 2\ A(13)\ e^2(k)] \quad (B.45)$$

A(10) will represent $e^3(k)$ so that

$$A(10) = e^2(k)\ e(k) \quad (B.46)$$

The denominator becomes

$$A(12) = e^2(k) + 2\ B(61)\ \ell^2(k)\ A(8) \quad (B.47)$$

$$A(11) = A(10)\ B(28) + A(9) \quad (B.48)$$

Therefore, $K_m(k)$ is expressed as

$$K_m(k) = B(5)\ \ell(k)\ A(11)/A(12) \quad (B.49)$$

B.4.5 Iteration scheme.

The accelerated Gauss-Seidel iteration process is used for U, V, K_m and e. The basic scheme has been described in detail in

Section 3.5. Some refinements were needed in order to prevent divergence which can occur very easily in the uppermost levels. Most of the problems occur when K_m drops to a very small value which causes the wind to become very large. Therefore, a minimum value much larger than the molecular diffusivity has to be specified near the top of the boundary layer. This can be done by specifying a reasonable value for K_m at the top of the boundary layer, say of the order of 100 cm^2/sec, and devising an analytical function for the minimum value of K_m at the uppermost grid points. In the lower boundary layer the molecular value (about 0.15 cm^2/sec) can be used as the minimum value for K_m. When the top of the boundary layer is fixed at 2 or 3 km it is necessary generally to compute U and V in double precision in order to get a good value for K_m. However, K_m, e and ℓ have enough accuracy in single precision.

The next problem is to determine when the iteration procedure has been completed. This is done by comparing two successive iterative values of K_m. We could use a criteria expressing the minimum percentage that the difference between two successive iterative values must meet in order to have convergence. In our case this is not desirable because we are more likely to obtain much greater accuracy in the lower boundary layer than near the top of the boundary layer. If we used a percentage we would have to choose between either a fairly large percentage with a reasonable number of iterations or a small percentage and an unnecessarily large number of iterations. Therefore, it is better to use an absolute number of the order of 1 to 10 cm^2/sec as a criterion which would insure high accuracy in the region where it is desired, that is, in the lower and middle

boundary layer. We will probably have less accuracy in K_m near the top of the boundary layer but this has only a very small influence on the wind profile.

B.5 Finite-Difference Equation for K_t and K_w.

As K_t and K_w are required in the time-dependent model they will be computed diagnostically from (B.5) which is transformed into

$$K_t(k) = K_w(k) = \left\{ B(5)\, \ell(k) \left[A(10) + A(9) \right] \right\} / e^2(k) \qquad (B.50)$$

B.6 Finite-Difference Equations: Second Form.

The diffusion terms in the equations for U and V can be written in two forms. The first form uses (3.26) and (3.27) and has been discussed in the previous sections. The second form uses (3.26') and (3.27'), and it has the advantage of giving a reasonable profile of not only the mean wind but also of the stress. The second form should be used if the set (3.26') to (3.29') is used in the time-dependent model. The finite-difference expressions are much more stable near the top of the boundary layer when we use the second form. This permits a greater OMEGA near the top of the boundary layer and insures a faster convergence.

B.6.1 Equation for U.

The diffusion term in (3.26') can be expanded as,

$$\left[\frac{\partial}{\partial y} \left(K_m \frac{\partial U}{\partial y} \frac{\partial y}{\partial z} \right) \right] \frac{\partial y}{\partial z} = \left[\left(K_m \frac{\partial U}{\partial y} \frac{\partial y}{\partial z} \right) \Big|_{k+\frac{1}{2}} - \left(K_m \frac{\partial U}{\partial y} \frac{\partial y}{\partial z} \right) \Big|_{k-\frac{1}{2}} \right] \frac{\partial y}{\partial z} \qquad (B.51)$$

In order to evaluate the stress at $k+\frac{1}{2}$, we recall that in

the surface layer

$$K_m \frac{\partial u}{\partial z} \propto (\ell u_*)/(AC\ \ell) = \text{constant} \qquad (B.52)$$

Therefore, it seems justified to assume the following arithmetic average

$$XKMP = \left(K_m \frac{\partial u}{\partial z}\right)\Big|_{k+\frac{1}{2}} = \tfrac{1}{2}\left[K_m(k+1)\ DELZ(k+1) + K_m(k)\ DELZ(k)\right] \qquad (B.53)$$

The vertical derivative of U is approximated by a finite-difference equation centered at $k+\frac{1}{2}$

$$\left.\frac{\partial U}{\partial y}\right|_{k+\frac{1}{2}} = U(k+1) - U(k) \qquad (B.54)$$

The stress is evaluated at $k-\frac{1}{2}$ by the same procedure,

$$XKMM = \left(K_m \frac{\partial u}{\partial z}\right)\Big|_{k-\frac{1}{2}} = \tfrac{1}{2}\left[K_m(k-1)\ DELZ(k-1) + K_m(k)\ DELZ(k)\right] \qquad (B.55)$$

$$\left.\frac{\partial U}{\partial y}\right|_{k-\frac{1}{2}} = U(k) - U(k-1) \qquad (B.56)$$

The coefficient of U(k) is

$$A(3) = XKMP + XKMM \qquad (B.57)$$

We group all the terms except U(k) in

$$DU = XKMP\ U(k+1) + XKMM\ U(k-1) + F\ (V(k) - V_g) \qquad (B.58)$$

Finally,

$$U(k) = DU/A(3) \qquad (B.59)$$

B.6.2 Equation for V.

The diffusion term in (3.27') is similar to the one in (3.26') with U being replaced by V. Therefore, it is sufficient to mention the resulting terms. All the terms except V(k) are grouped in

$$DV = XKMP\ V(k+1) + XKMM\ V(k-1) + F\ (U_g - U(k)) \qquad (B.60)$$

Finally,

$$V(k) = DV/A(3) \qquad (B.61)$$

APPENDIX C

TIME-DEPENDENT ATMOSPHERIC EQUATIONS

C.1 Equations.

The basic equations for the time-dependent model in φ-coordinates are given in Section 3.3.1 and will not be repeated here. The equation for the mixing length ℓ and for its derivative with respect to φ have been derived in Section B.2. The discussion in Section B.3 about the vertical derivative of K_m in the steady-state model is also valid for the time-dependent model. However, in this case the thickness of the surface layer will vary according to the diurnal cycle and may be fairly small during the nocturnal inversion. Therefore, we should use (B.20) only up to the level expected to represent the top of the nearly-constant-stress layer during the nightime.

C.2 Notation.

In our implicit finite-difference scheme all of the variables in the equations which are not differentiated with respect to time have to be evaluated at the two time steps t_o and $t_o + \Delta t$. This would imply repeating two nearly identical terms differing only in their time index. In our discussion we will outline how the calculations are done and write out these terms with a general time index t. The following arrays are frequently used:

A = expressions involving the atmospheric variables,

B = various constants,

C = expressions related to the computation of the surface tem-

perature,

D = expressions involving the atmospheric variables at the past time step t_o.

The variables starting with the letter D and containing at least three letters indicate a finite-difference approximation to a derivative. Termination with 1 implies the first derivative and termination with 2 implies the second derivative. For example,

DU1 = first derivative of U

DT2 = second derivative of Ⓗ.

The name of the variable being differentiated is found between D and 1 or 2. As the symbol Ⓗ is not generally available in FORTRAN, T has been substituted for it.

As pointed out in Section 3.3.2, the diffusion term can be expressed in two forms in σ-coordinates. Equations (3.26) to (3.29) involve differentiation of the coefficient of eddy diffusivity and the first and second derivatives of the mean quantities. This form leads to computational problems which are described in Section C.5. Equations (3.26') to (3.29') involve differentiation of the flux of the mean quantity with respect to σ. This second form gives a realistic variation of the flux in the vertical and is computationally more stable. Section C.3 uses the first form whereas Section C.4 uses the second form.

C.3 Finite-Difference Equations: First Form.

C.3.1 Equation for U.

The basic equation is (3.26). The vertical derivative of K_m is evaluated as,

$$\left.\frac{\partial K_m}{\partial \varphi}\right|_t = DKM1\Big|_t = \begin{cases} \frac{1}{2}(K_m(k+1,t)-K_m(k-1,t)) & \text{above the constant-flux layer} \\ \frac{K_m(k,t)}{2}\ln\left(\frac{K_m(k+1,t)}{K_m(k-1,t)}\right) & \text{in the constant-flux layer} \end{cases} \quad (C.1)$$

Other terms involved in the diffusion term are,

$$A(2)\Big|_t = \tfrac{1}{2}\left(\frac{\partial K_m}{\partial \varphi}\left(\frac{\partial \varphi}{\partial z}\right)^2 + K_m\frac{\partial^2 \varphi}{\partial z^2}\right)\Big|_t =$$

$$\tfrac{1}{2}\left(DKM1\Big|_t\, DELZ2(k) + K_m(k,t)\, DEL2Z(k)\right) \quad (C.2)$$

$$A(1)\Big|_t = K_m\left(\frac{\partial \varphi}{\partial z}\right)^2 = K_m(k,t)\, DELZ2(k) \quad (C.3)$$

The ratio of these two coefficients is,

$$AA\Big|_t = A(2)/A(1)\Big|_t \quad (C.4)$$

The geostrophic and Coriolis terms become,

$$FAC = f(V-V_g) = \tfrac{1}{2}f(V(k,t_o)+V(k,t_o+\Delta t)-2V_g) \quad (C.5)$$

The first and second derivative terms are,

$$DU1\Big|_t = 2\frac{\partial U}{\partial \varphi} = U(k+1,t)-U(k-1,t) \quad (C.6)$$

$$DU2\Big|_t = \frac{\partial^2 U}{\partial \varphi^2} = U(k+1,t)-U(k,t)+U(k-1,t)-U(k,t) \quad (C.7)$$

The diffusion term at t_o is evaluated as,

$$D(k,1) = \left(DU2\Big|_{t_o} + AA\Big|_{t_o} DU1\Big|_{t_o}\right) \quad (C.8)$$

If we exclude $U(k,t_o+\Delta t)$ in the diffusion term at $t_o+\Delta t$, we are left with,

$$DU\Big|_{t_o+\Delta t} = \left(U(k+1,t_o+\Delta t)+U(k-1,t_o+\Delta t)+(AA\ DU1)\Big|_{t_o+\Delta t}\right) \quad (C.9)$$

The coefficient of $U(k,t_o+\Delta t)$ is,

$$CST = 1/\Delta t + A(1) \quad (C.10)$$

Therefore, the expression for $U(k,t_o+\Delta t)$ is,

$$U(k,t_o+\Delta t) = \left\{U(k,t_o)/\Delta t + FAC + A(1)\left[\left[DU+D(k,1)\right]/2\right]\right\}/CST \quad (C.11)$$

C.3.2 Equation for V.

The equation for V is very similar to the one for U. Therefore, the coefficients of the diffusion term involved in (3.26) are the same ones as those involved in (3.25). The first and second derivative terms are:

$$DV1\Big|_t = 2\,\frac{\partial V}{\partial \eta} = V(k+1,t)-V(k-1,t) \qquad (C.12)$$

$$DV2\Big|_t = \frac{\partial^2 V}{\partial \eta^2} = V(k+1,t)-V(k,t)+V(k-1,t)-V(k,t) \qquad (C.13)$$

The diffusion term at t_o becomes,

$$D(k,2) = \left(DV2\Big|_{t_o} + AA\Big|_{t_o}\, DV1\Big|_{t_o}\right) \qquad (C.14)$$

A part of the diffusion term at $t_o+\Delta t$ is,

$$DV\Big|_{t_o+\Delta t} = \left(V(k+1,t_o+\Delta t)+V(k-1,t_o+\Delta t)+(AA\ DV1)\Big|_{t_o+\Delta t}\right) \qquad (C.15)$$

The geostrophic and Coriolis terms are written as,

$$FAC = f(U_g-U) = \tfrac{1}{2}f\left\{2V_g-\left[V(k,t_o)+V(k,t_o+\Delta t)\right]\right\} \qquad (C.16)$$

Finally,

$$V(k,t_o+\Delta t)=\left\{V(k,t_o)/\Delta t+FAC+A(1)\left\{\left[DV+D(k,2)\right]/2\right\}\right\}/CST \qquad (C.17)$$

C.3.3 Equation for Ⓗ.

The derivative of K_t with respect to η is,

$$\frac{\partial K_t}{\partial \eta}\Big|_t = DKT1\Big|_t = \begin{cases} \tfrac{1}{2}(K_t(k+1,t)-K_t(k-1,t)) & \text{above the constant-flux layer} \\ \dfrac{K_t(k,t)}{2}\ln\left(\dfrac{K_t(k+1,t)}{K_t(k-1,t)}\right) & \text{in the constant-flux layer} \end{cases} \qquad (C.18)$$

The coefficients involved in the diffusion term at t_o are,

$$A(6)\Big|_t = \tfrac{1}{2}\left(\frac{\partial K_t}{\partial \eta}\left(\frac{\partial \eta}{\partial z}\right)^2 + K_t\frac{\partial^2 \eta}{\partial z^2}\right)\Big|_t =$$

$$\tfrac{1}{2}\left(DKT1\Big|_t\ DELZ2(k) + K_t(k,t)\ DEL2Z(k)\right) \qquad (C.19)$$

$$A(5)\Big|_t = K_t \left(\frac{\partial \psi}{\partial z}\right)^2 = K_t(k,t)\ DELZ2(k) \qquad (C.20)$$

The first and second derivatives of Θ with respect to ψ are,

$$DT1\Big|_t = 2\frac{\partial \Theta}{\partial \psi} = \Theta(k+1,t) - \Theta(k-1,t) \qquad (C.21)$$

$$DT2\Big|_t = \frac{\partial^2 \Theta}{\partial \psi^2} = \Theta(k+1,t) - \Theta(k,t) + \Theta(k-1,t) - \Theta(k,t) \qquad (C.22)$$

The diffusion term evaluated at t_o is,

$$D(k,3) = \left(DT2\Big|_{t_o} + (A(6)/A(5)DT1)\Big|_{t_o}\right) \qquad (C.23)$$

Part of the diffusion term at $t_o + \Delta t$ can be written as,

$$DDT\Big|_{t_o+\Delta t} = \Theta(k+1,t_o+\Delta t) + \Theta(k-1,t_o+\Delta t) + \left[A(6)/A(5)DT1\right]\Big|_{t_o+\Delta t} \qquad (C.24)$$

The coefficient of $\Theta(k,t_o+\Delta t)$ is,

$$CST2 = 1/\Delta t + A(5) \qquad (C.25)$$

Therefore,

$$\Theta(k,t_o+\Delta t) = \left\{\Theta(k,t_o)/\Delta t + A(5)\left[\left[DDT + D(k,3)\right]/2\right]\right\}/CST2 \qquad (C.26)$$

C.3.4 Equation for Q.

The basic equation is (3.29). The vertical derivative of K_w is,

$$\frac{\partial K_w}{\partial \psi}\Big|_t = DKW1\Big|_t = \begin{cases} \frac{1}{2}(K_w(k+1,t) - K_w(k-1,t)) & \text{above the constant-flux layer} \\ \frac{K_w(k,t)}{2}\ln\left(\frac{K_w(k+1,t)}{K_w(k-1,t)}\right) & \text{in the constant-flux layer} \end{cases} \qquad (C.27)$$

The coefficients of the diffusion terms are,

$$A(9)\Big|_t = \frac{1}{2}\left(\frac{\partial K_w}{\partial \psi}\left(\frac{\partial \psi}{\partial z}\right)^2 + K_w\frac{\partial^2 \psi}{\partial z^2}\right)\Big|_t =$$

$$\frac{1}{2}\left(DKW1\Big|_t\ DELZ2(k) + K_w(k,t)\ DEL2Z(k)\right) \qquad (C.28)$$

$$A(8) = K_w\left(\frac{\partial \psi}{\partial z}\right)^2 = K_w(k,t)\ DELZ2(k) \qquad (C.29)$$

The first and second derivative terms become,

$$DQ1\Big|_t = 2\frac{\partial Q}{\partial \eta} = Q(k+1,t) - Q(k-1,t) \qquad (C.30)$$

$$DQ2\Big|_t = \frac{\partial^2 Q}{\partial \eta^2} = Q(k+1,t) - Q(k,t) + Q(k-1,t) - Q(k,t) \qquad (C.31)$$

The diffusion term at t_o is,

$$D(k,4) = \left(DQ2\Big|_{t_o} + (A(9)/A(8)DQ1)\Big|_{t_o}\right) \qquad (C.32)$$

The diffusion term at $t_o + \Delta t$ can be written as follows when we exclude $Q(k,t_o+\Delta t)$,

$$DDQ\Big|_{t_o+\Delta t} = Q(k+1,t_o+\Delta t) + Q(k-1,t_o+\Delta t) + (A(9)/A(8)DQ1)\Big|_{t_o+\Delta t} \qquad (C.33)$$

The coefficient of $Q(k,t_o+\Delta t)$ is,

$$CST3 = 1/\Delta t + A(8) \qquad (C.34)$$

Finally,

$$Q(k,t_o+\Delta t) = \left\{Q(k,t_o)/\Delta t + A(8)\left[(DDQ + D(k,4))/2\right]\right\}/CST3 \qquad (C.35)$$

C.3.5 Equation for e.

Equation (3.31) is the equation for e^2. We define some of the terms which are frequently used in the equations. The various derivatives of the mean quantities are called,

$$A(11)\Big|_t = 2\left|\frac{\partial \vec{V}}{\partial z}\right|^2 = 2\left(\left(\frac{\partial U}{\partial z}\right)^2 + \left(\frac{\partial V}{\partial z}\right)^2\right) = \tfrac{1}{2}\left((DU1)^2 + (DV1)^2\right)\Big|_t \; DELZ2(k) \qquad (C.36)$$

$$DTA\Big|_t = 2\frac{\partial \Theta}{\partial z} = 2\,DT1\Big|_t \; DELZ(k) \qquad (C.37)$$

$$DQA\Big|_t = 2\frac{\partial Q}{\partial z} = 2\,DQ1\Big|_t \; DELZ(k) \qquad (C.38)$$

The covariances representing the heat flux and the flux of water vapor are, respectively,

$$WT\Big|_t = 2\,\overline{w\theta} = -K_t(k,t)\,DTA \qquad (C.39)$$

$$WQ\Big|_t = 2\,\overline{wq} = -K_w(k,t)\,DQA \qquad (C.40)$$

These two covariances can be combined through the concept of virtual temperature,

$$A(12)\Big|_t = 2\frac{g}{T_o}\overline{w\theta_v} = B(21)\,WT + B(20)\,WQ \qquad (C.41)$$

where,

$$B(21) = g/T_o \qquad (C.42)$$

$$B(20) = 0.6078\,g \qquad (C.43)$$

We define,

$$AF\Big|_t = e\,l\Big|_t = e(k,t)\,l(k,t) \qquad (C.44)$$

The coefficients of the diffusion terms are,

$$A(13)\Big|_t = \frac{5x0.23}{3}\,e\,l\left(\frac{\partial y}{\partial z}\right)^2 = B(22)\,AF\Big|_t\,DELZ2(k) \qquad (C.45)$$

$$A(14)\Big|_t = \tfrac{1}{2}\left(e\,l\Big|_t\frac{\partial^2 y}{\partial z^2} + \frac{\partial e\,l}{\partial y}\left(\frac{\partial y}{\partial z}\right)^2\right) = \qquad (C.46)$$

$$\tfrac{1}{2}\left\{AF\;DEL2Z(k) + \left[l(k,t)\,DE\Big|_t + e(k,t)\,DL(k)\right]DEL2Z(k)\right\}$$

where,

$$DE\Big|_t = \frac{\partial e}{\partial y} = \tfrac{1}{2}(e(k+1,t) - e(k-1,t)) \qquad (C.47)$$

$$DL(k) = \frac{\partial l}{\partial y} = DELZZ(k)/\,l^2(k,t) \qquad (C.48)$$

$$B(22) = \frac{5x0.23}{3} \qquad (C.49)$$

The terms evaluated at t_o are grouped in,

$$D(k,5) = \left(\frac{\partial}{\partial z}\left(e\,l\frac{\partial e^2}{\partial z}\right) + K_m\left|\frac{\partial \vec{V}}{\partial z}\right|^2 + \frac{g}{T_o}\overline{w\theta_v}\,e^2/2/\Delta t - \frac{2\,e^3}{B_1\,l}\right)\Big|_{t_o} =$$

$$(A(13)\,DE2 + A(14)\,DE1 + A(12))\Big|_{t_o} + K_m(k,t_o)\,A(11)\Big|_{t_o} + e^2(k,t_o)\,(2/\Delta t$$

$$- B(24)\,e(k,t_o)/\,l(k,t_o)) \qquad (C.50)$$

The terms which are different from $e^2(k,t_o+\Delta t)$ and which are evaluated at $t_o+\Delta t$, are,

$$A(16) = \left(\frac{5x0.23}{3}\left[\frac{\partial}{\partial z}\left(e\,l\frac{\partial e^2}{\partial z}\right)\right] + 2\left(K_m\left|\frac{\partial \vec{V}}{\partial z}\right|^2 + \frac{g}{T_o}\overline{w\theta_v}\right)\right)\Big|_{t_o+\Delta t} =$$

$$B(22)\,(A(13)\,DE2 + A(14)\,DE1) + K_m(k,t)\,A(11) + A(12) \qquad (C.51)$$

Finally,

$$E2T = e^2(k,t_o+\Delta t) = (D(k,5)+A(16))/[2(1/\Delta t+A(13))\Big|_{t_o+\Delta t})+B(24)\, e(k,t_o+\Delta t)/\ell(k,t_o+\Delta t)] \quad (C.52)$$

$$e(k,t_o+\Delta t) = (e^2(k,t_o+\Delta t))^{\frac{1}{2}}=SQRT(E2T) \quad (C.53)$$

C.3.6 Computation of $\overline{\theta^2}$.

Equation (3.32) is used. The coefficients of the diffusion term are similar to A(13) and A(14) which were derived for e^2. The only difference is that the constant B(22) has been replaced by 0.23. Therefore,

$$A'(13)\Big|_{\overline{\theta^2}} = 0.6\ A(13)\Big|_{e^2} \quad (C.54)$$

$$A'(14)\Big|_{\overline{\theta^2}} = 0.6\ A(14)\Big|_{e^2} \quad (C.55)$$

The first and second derivatives are respectively,

$$DT21\Big|_t = 2\left(\frac{\partial \overline{\theta^2}}{\partial y}\right) = \overline{\theta^2}(k+1,t) - \overline{\theta^2}(k-1,t) \quad (C.56)$$

$$DT22\Big|_t=\left(\frac{\partial^2 \overline{\theta^2}}{\partial y^2}\right)= \overline{\theta^2}(k+1,t)-\overline{\theta^2}(k,t)+\overline{\theta^2}(k-1,t)-\overline{\theta^2}(k,t) \quad (C.57)$$

A term which is encountered in $\overline{\theta^2}$, $\overline{\theta q}$ and $\overline{q^2}$, is,

$$A(21)\Big|_{t_o} = 2(1/\Delta t-e/(\ell B_2))\Big|_{t_o} = 2/\Delta t-B(26)\ e(k,t_o)/\ell(k,t_o) \quad (C.58)$$

where,

$$B(26) = 2/B_2 \quad (C.59)$$

The terms evaluated at the past time step t_o are,

$$D(k,6) = (A'(13)\ DT22+A'(14)\ DT21-WT\ DQA/2)\Big|_{t_o} + \overline{\theta^2}(k,t_o)\ A(21)\Big|_{t_o} \quad (C.60)$$

The coefficient of $\overline{\theta^2}(k,t_o+\Delta t)$ is,

$$A(18) = 2(1/\Delta t+A(13))+ B(26)\ e(k,t_o+\Delta t)/\ell(k,t_o+\Delta t) \quad (C.61)$$

The terms different from $\overline{\theta^2}(k,t_o+\Delta t)$ at $t_o+\Delta t$, are,

$$A(19) = \left[A'(13)\ DT22 + A'(14)\ DT21 - WT\ DQA/2\right]\Big|_{t_o+\Delta t} \quad (C.62)$$

Finally,

$$\overline{\theta^2}(k,t_o+\Delta t) = (A(19) + D(k,6))/A(18) \quad (C.63)$$

C.3.7 Computation of $\overline{q^2}$.

The reference equation is (3.33) whose formulation is similar to (3.32). Therefore, the coefficients A'(13), A'(14), A(18) and A(21) remain unchanged. The first and second derivative terms are,

$$DQ21\ \Big|_t = 2\,\frac{\partial\,\overline{q^2}}{\partial y} = \overline{q^2}(k+1,t) - \overline{q^2}(k-1,t) \quad (C.64)$$

$$DQ22\ \Big|_t = \frac{\partial^2\overline{q^2}}{\partial y^2} = \overline{q^2}(k+1,t) - \overline{q^2}(k,t) + \overline{q^2}(k-1,t) - \overline{q^2}(k,t) \quad (C.65)$$

The terms which are evaluated at the past time step, are,

$$D(k,7) = (A'(13)\ DQ22 + A'(14)\ DQ21 - WQ\ DQA/2)\Big|_{t_o} + \overline{q^2}(k,t_o)\ A(21) \quad (C.66)$$

We group together all the terms evaluated at $t_o+\Delta t$, except $\overline{q^2}(k,t_o+\Delta t)$.

$$A(22) = A'(13)\ DQ22 + A'(14)\ DQ21 - WQ\ DQA/2 \quad (C.67)$$

Therefore,

$$\overline{q^2}(k,t) = (A(22) + D(k,7))/A(18) \quad (C.68)$$

C.3.8 Equation for $\overline{\theta q}$.

Equation (3.34) is used for $\overline{\theta q}$. Again, the coefficients A'(13), A'(14), A(18) and A(21) are the same ones as derived for $\overline{\theta^2}$. The first and second derivatives are,

$$DTQ1\Big|_t = 2\,\frac{\partial\,\overline{\theta q}}{\partial y} = \overline{\theta q}(k+1,t) - \overline{\theta q}(k-1,t) \qquad (C.69)$$

$$DTQ2\Big|_t = \frac{\partial^2\,\overline{\theta q}}{\partial y^2} = \overline{\theta q}(k+1,t) - \overline{\theta q}(k,t) + \overline{\theta q}(k-1,t) - \overline{\theta q}(k,t) \qquad (C.70)$$

The terms evaluated at t_o are,

$$D(k,8) = (A'(13)\ DTQ2 + A'(14)\ DTQ1 - (WQ\ DTA + WT\ DQA)/4)\Big|_{t_o} + \overline{\theta q}(k,t_o)\ A(21)\Big|_{t_o} \qquad (C.71)$$

The term at $t_o+\Delta t$ which is equivalent to D(k,8), is,

$$A(22) = (A'(13)\ DTQ2 + A'(14)\ DTQ1 - (WQ\ DTA+WT\ DQA)/4)\Big|_{t_o+\Delta t} \qquad (C.72)$$

The final result is that,

$$\overline{\theta q}(k,t_o) = (A(22) + D(k,8))/A(18) \qquad (C.73)$$

C.3.9 Equation for K_m.

Equation (3.35) is the equation for K_m. We will drop the time index for the next three sections because the coefficients of diffusivity K_m, K_t and K_w are evaluated diagnostically at the time step $t_o+\Delta t$. Some terms are common to all three coefficients of eddy diffusivity and are,

$$AG = e^3 = e^2(k)\ e(k) \qquad (C.74)$$

$$A(23) = 4\,A_1\,l\,\frac{\partial}{\partial z}\left(e\,l\,\frac{\partial e^2}{\partial z}\right) \qquad (C.75)$$

When we use the results which we have obtained in the previous sections, we can rewrite (C.75) as,

$$A(23) = B(31)\ (A'(13)\ DE2 - 2\,e^2(k) + A'(14)\ DE1)\,l(k) \qquad (C.76)$$

where,

$$B(31) = 4\,A_1 \qquad (C.77)$$

Also,

$$AR = B(5)\,\ell(k) \qquad (C.78)$$

where,

$$B(5) = A_1 \qquad (C.79)$$

The numerator in (3.35) is expanded as,

$$A(24) = AR\,(B(28)\,AG + A(23) + (B(43)\,WT + B(45)\,WQ)\,\ell(k)) \qquad (C.80)$$

where,

$$B(28) = 1 - 3C_1 \qquad (C.81)$$

$$B(43) = \frac{21\,A_1}{2}\,\frac{g}{T_o} \qquad (C.82)$$

$$B(45) = \frac{21\,A_1}{2}\,0.6078\,g \qquad (C.83)$$

The denominator is,

$$A(25) = e^2(k,t) + B(47)\,(A(11) + 1.5\,(B(21)\,DTA + B(20)\,DQA))\,\ell^2(k) \qquad (C.84)$$

where,

$$B(47) = 3\,A_1^2 \qquad (C.85)$$

Finally,

$$K_m(k) = A(24)/A(25) \qquad (C.86)$$

C.3.10 Equation for K_t.

Equation (3.36) is appropriate for K_t. A term common to both K_t and K_w is,

$$AX = e^3 + 4\,A_1\,0.23\,\ell\,\frac{\partial}{\partial z}\left(e\,\ell\,\frac{\partial e^2}{\partial z}\right) - 6\,A_1\,\ell\,K_m\left|\frac{\partial \vec{V}}{\partial z}\right|^2$$

$$= AG + A(23) - B(36)\,\ell(k)\,K_m(k)\,A(11) \qquad (C.87)$$

where,

$$B(36) = 3\,A_1 \qquad (C.88)$$

The numerator in (3.36) is,

$$A(26)\,AR = AR\,(AX + B(46)\,WQ\,\ell(k) - 6\,\ell(k)\,(B(21)\,\overline{\theta^2}(k) + B(20)\,\overline{\theta q}(k))/DTA) \qquad (C.89)$$

where,

$$B(46) = 6\,A_1\,0.6078\,g \qquad (C.90)$$

The denominator becomes,

$$A(27) = e^2(k) + B(58)\ DTA\ \ell^2(k) \qquad (C.91)$$

where,

$$B(58) = 6A_1^2\ g/T_o \qquad (C.92)$$

Therefore,

$$K_t(k) = AR\ A(26)/A(27) \qquad (C.93)$$

C.3.11 Equation for K_w.

Equation (3.37) is used for K_w. The numerator can be expressed as,

$$A(28)\ AR = AR\left\{ AX+B(63)\ \ell(k)\ WT-6\ e(k)\left[B(21)\ \overline{\theta q}(k)+B(20)\ \overline{q^2}(k)\right]/DQA\right] \qquad (C.94)$$

where,

$$B(63) = 6\ A_1\ g/T_o \qquad (C.95)$$

The denominator is,

$$A(29) = e^2(k) + B(33)\ \ell^2(k)\ DQA \qquad (C.96)$$

Finally,

$$K_w(k) = AR\ A(28)/A(29)$$

C.4 Finite-Difference Equations: Second Form.

C.4.1 Equation for U.

The diffusion term in (3.26') is expanded as,

$$\frac{\partial}{\partial y}\left(K_m \frac{\partial U}{\partial y}\frac{\partial \ell'}{\partial z}\right)\frac{\partial y}{\partial z} = \left[\left(K_m \frac{\partial U}{\partial y}\frac{\partial y}{\partial z}\right)\Big|_{k+\frac{1}{2}} - \left(K_m \frac{\partial U}{\partial y}\frac{\partial y}{\partial z}\right)\Big|_{k-\frac{1}{2}}\right]\frac{\partial y}{\partial z} \tag{C.97}$$

In order to evaluate the stress at $k+\frac{1}{2}$, we recall that in the surface layer,

$$K_m \frac{\partial y}{\partial z} \alpha \left(\ell u_*\right)/(AC\ell) = \text{constant} \tag{C.98}$$

Therefore, it seems justified to assume the following arithmetic average,

$$2\,XKMP\Big|_t = \left(K_m \frac{\partial y}{\partial z}\right)\Big|_{k+\frac{1}{2},t} = \tfrac{1}{2}\left(K_m(k+1,t)\,DELZ(k+1) + K_m(k,t)\,DELZ(k)\right) \tag{C.99}$$

The vertical derivative of U is approximated by a finite-difference equation centered at $k+\frac{1}{2}$,

$$\frac{\partial U}{\partial y}\Big|_{k+\frac{1}{2},t} = U(k+1,t) - U(k,t) \tag{C.100}$$

The stress is evaluated at $k-\frac{1}{2}$ by the same procedure,

$$2\,XKMM\Big|_t = \left(K_m \frac{\partial y}{\partial z}\right)\Big|_{k-\frac{1}{2},t} = \tfrac{1}{2}\left[K_m(k-1,t)\,DELZ(k-1) + K_m(k,t)\,DELZ(k)\right] \tag{C.101}$$

$$\frac{\partial U}{\partial y}\Big|_{k-\frac{1}{2},t} = U(k,t) - U(k-1,t) \tag{C.102}$$

We group all the results and obtain,

$$\tfrac{1}{2}\frac{\partial}{\partial z}\left(K_m \frac{\partial U}{\partial z}\right)\Big|_t = DELZ(k)\left[U(k+1,t)\,XKMP - U(k,t)(XKMM+XKMP) + U(k-1,t)\,XKMM\right] \tag{C.103}$$

We will use the same finite-difference scheme as described in Section 3.4.2. As a result, we group the expressions evaluated at

the past time step in D(k,1),

$$D(k,1) = DELZ(k)\{[U(k+1,t_o)-U(k,t_o)]\,XKMP|_{t_o} + [U(k-1,t_o)-U(k,t_o)]\,XKMM|_{t_o}\} + F[V(k,t_o)/2 - V_g] \qquad (C.104)$$

The coefficient of $U(k,t_o+\Delta t)$ is,

$$CST = 1/\Delta t + (XKMP+XKMM)|_{t_o+\Delta t}\ DELZ(k) \qquad (C.105)$$

Finally,

$$U(k,t_o+\Delta t) = \{[XKMP|_{t_o+\Delta t}\ U(k+1,t_o+\Delta t) + XKMM|_{t_o+\Delta t}\ U(k-1,t_o+\Delta t)]\ DELZ(k) + D(k,1) - F\ V(k,t_o+\Delta t)/2 + U(k,t_o)/\Delta t\}/CST \qquad (C.106)$$

The mathematical expressions could have been condensed but the condensed expressions would not minimize the round-off errors as well as the expanded version of the equations. In Section C.6 we will discuss in some detail the problem of round-off errors in the determination of the profile of the mean quantities.

C.4.2 Equation for V.

The diffusion term in (3.27') is similar to the one in (3.26') with U being replaced by V. Therefore, it is sufficient to mention the resulting terms. The expressions evaluated at t_o are,

$$D(k,2) = DELZ(k)\{[V(k+1,t_o)-V(k,t_o)]\,XKMP|_{t_o} + [V(k-1,t_o)-V(k,t_o)]\,XKMM|_{t_o}\} + F[U_g - U(k,t_o)/2] \qquad (C.107)$$

Consequently,

$$V(k,t_o+\Delta t) = \{[XKMP|_{t_o+\Delta t}\ V(k+1,t_o+\Delta t) + XKMM|_{t_o+\Delta t}\ V(k-1,t_o+\Delta t)]\ DELZ(k) + D(k,2) - F\ U(k,t_o+\Delta t)/2 + V(k,t_o)/\Delta t\}/CST \qquad (C.108)$$

C.4.3 Equation for Ⓗ.

The diffusion term involved in (3.28') is similar to the one in (3.26') if we replace U by Ⓗ, and K_m by K_t. Therefore, parts of the heat-flux terms are,

$$2\ XKTM\big|_t = \left(K_t \frac{\partial \mathcal{Y}}{\partial z}\right)\Big|_{k-\frac{1}{2},t} = \tfrac{1}{2}\left[K_t(k-1,t)\ DELZ(k-1) + K_t(k,t)\ DELZ(k)\right] \tag{C.109}$$

$$2\ XKTP\big|_t = \left(K_t \frac{\partial \mathcal{Y}}{\partial z}\right)\Big|_{k+\frac{1}{2},t} = \tfrac{1}{2}\left[K_t(k+1,t)\ DELZ(k+1) + K_t(k,t)\ DELZ(k)\right] \tag{C.110}$$

When we use the centered finite-difference approximation to the $\mathcal{Y}$-derivative of Ⓗ, we obtain,

$$\tfrac{1}{2}\left(\frac{\partial}{\partial z} K_t \frac{\partial Ⓗ}{\partial z}\right)\Big|_t = DELZ(k)\left[Ⓗ(k+1,t)\ XKTP\big|_t - Ⓗ(k,t)(XKTP+XKTM)\big|_t + Ⓗ(k-1,t)\ XKTM\big|_t\right] \tag{C.111}$$

The expressions computed at the past time step are grouped into,

$$D(k,3) = DELZ(k)\left\{\left[Ⓗ(k+1,t_o) - Ⓗ(k,t_o)\right] XKTP\big|_{t_o} + \left[Ⓗ(k-1,t_o) - Ⓗ(k,t_o)\right] XKTM\big|_{t_o}\right\} \tag{C.112}$$

The coefficient of $Ⓗ(k,t_o+\Delta t)$ is,

$$CST2 = 1/\Delta t + (XKTM+XKTP)\big|_{t_o+\Delta t}\ DELZ(k) \tag{C.113}$$

Finally,

$$Ⓗ(k,t_o+\Delta t) = Ⓗ(k,t_o)\left\{\left\{\left[\left(XKTP\big|_{t_o+\Delta t}\ (Ⓗ(k+1,t_o+\Delta t)/Ⓗ(k,t_o)\right) + XKTM\big|_{t_o+\Delta t}\ (Ⓗ(k-1,t_o+\Delta t)/Ⓗ(k,t_o))\right] - DELZ(k)\right\}/CST2\right\} \tag{C.114}$$

C.4.4 Equation for Q.

Equation (3.29') is similar to (3.28') if we replace K_t by K_w, and Ⓗ by Q. Therefore, parts of the water-vapor-flux terms are,

$$2\,XKWP\big|_t = \left(K_w \frac{\partial \psi}{\partial z}\right)\Big|_{k+\frac{1}{2},t} = \tfrac{1}{2}\left[K_w(k+1,t)\,DELZ(k+1) + K_w(k,t)\,DELZ(k)\right] \qquad (C.115)$$

$$2\,XKWM\big|_t = \left(K_w \frac{\partial \psi}{\partial z}\right)\Big|_{k-\frac{1}{2},t} = \tfrac{1}{2}\left[K_w(k-1,t)\,DELZ(k-1) + K_w(k,t)\,DELZ(k)\right] \qquad (C.116)$$

The diffusion term can be expressed as,

$$\tfrac{1}{2}\left(\frac{\partial}{\partial z} K_w \frac{\partial Q}{\partial z}\right)\Big|_t = DELZ(k)\left[Q(k+1,t)\,XKWP\big|_t - Q(k,t)(XKWP+XKWM)\big|_t + Q(k-1,t)\,XKWM\big|_t\right] \qquad (C.117)$$

in which the centered finite-difference approximation has been used to evaluate the ψ-derivative of Q. The expressions computed at t_o are,

$$D(k,4) = DELZ(k)\left\{\left[Q(k+1,t_o)-Q(k,t_o)\right]XKWP\big|_{t_o} + \left[Q(k-1,t_o)-Q(k,t_o)\right]XKWM\big|_{t_o}\right\} \qquad (C.118)$$

The coefficient of $Q(t_o+\Delta t)$ is,

$$CST3 = 1/\Delta t + (XKWP+XKWM)\big|_{t_o}\,DELZ(k) \qquad (C.119)$$

Finally,

$$Q(k,t_o+\Delta t) = \left\{\left[XKWP_{\,t_o+\Delta t}\,Q(k+1,t_o+\Delta t) + XKWM\big|_{t_o+\Delta t}\,Q(k-1,t_o+\Delta t)\right]DELZ(k) + D(k,4) + Q(k,t_o)/\Delta t\right\}/CST3 \qquad (C.120)$$

C.4.5 Other Equations.

The other equations are left unchanged and can be found from Section C.3.5 to Section C.3.11.

C.5 Computational Problems.

In this section we will deal with the computational problems associated with the first form of the diffusion term. We will discuss only the problems encountered with (3.28) for the following reasons:

1) The computation of the temperature profile is the most sensitive to these problems.

2) The equation for Ⓗ is simpler to analyse than the ones for U and V because it does not involve Coriolis or pressure-gradient forces.

3) The derived conclusions from the analysis of Ⓗ are applicable to the other 3 main quantities because of the similitude of the equations.

Therefore, it is sufficient to analyse the behavior of the equation for Ⓗ. Another simplifying assumption in the analysis is the use of the forward-in-time finite-difference approximation to (3.28) instead of the finite-difference approximation used in our equations and described in section 3.4.2. Therefore,

$$\frac{\partial A}{\partial t} = f \qquad \text{(C.121)}$$

will be approximated in our discussion by,

$$A(t_o+\Delta t) = A(t_o) + \Delta t\, f(t_o+\Delta t) \qquad \text{(C.122)}$$

The reasons for that simplification are:

1) The finite-difference equation becomes simpler as it involves roughly only half the number of terms required by the other time-finite-difference approximation.

2) The conclusions which will be drawn from our discussions are almost immediately applicable to the actual finite-difference equations used in the program if we look into the effect caused by two consecutive

time steps.

C.5.1. Formation of Artificial Inversions: Case of no Real Inversion.

The inversion can be generated only by the earth's surface in our model because the temperature at the top of the boundary layer is kept fixed at all times. The top of the inversion will be carried upward with the help of turbulent diffusion. The diurnal temperature cycle has only one maximum and one minimum per day because we neglect advection and cloud formation. The model is started from neutral stability at the time of maximum temperature. Therefore, the earth's surface will cool down for the first few hours creating a stable layer throughout the atmosphere without any inversion. If the model develops any inversion, this will be caused by numerical problems. The model ran smoothly until we obtained a region where K_t was varying rapidly due to the increasing stability, and this caused the formation of an unstable layer on top of the surface-based stable layer. This behavior caused a deterioration of the model and ultimately caused divergence of the results. The finite-difference version of (3.28) becomes, when we neglect the time-derivative term,

$$Ⓗ(k) = \frac{(A(1) + A(2))Ⓗ(k+1) + (A(1) - A(2))Ⓗ(k-1)}{2\,A(1)} \qquad (C.123)$$

where, $A(1) = K_t(k)\ DELZ2(k)$, associated with the second derivative,

and $A(2) = K_t \frac{\partial^2 \varphi}{\partial z^2} + \frac{\partial K_t}{\partial \varphi}\left(\frac{\partial \varphi}{\partial z}\right)^2$, associated with the first derivative of Ⓗ with respect to φ.

If we restrict K_t to non-negative values, then A(1) is always positive. However, A(2) can be of either sign depending on the sign of the φ-derivative of K_t. Some possibilities are,

Case 1: $A(2) = A(1)$

In this case we have: $\textcircled{H}(k) = \textcircled{H}(k+1)$

Case 2: $A(2) = 0$

Now, we obtain: $\textcircled{H}(k) = \dfrac{\textcircled{H}(k+1) + \textcircled{H}(k-1)}{2}$

Case 3: $A(2) = -A(1)$

This implies: $\textcircled{H}(k) = \textcircled{H}(k-1)$

Therefore, for

$$A(2) \in [-A(1), A(1)],$$

we have,

$$\textcircled{H}(k) \in [\textcircled{H}(k-1), \textcircled{H}(k+1)]$$

where $\in$ signifies that the term on the left-hand side is within the range defined by the terms inside the brackets on the right-hand side. Conversely if $A(2)$ is not in the above-defined range, then $\textcircled{H}(k)$ is computed outside the range $[\textcircled{H}(k-1), \textcircled{H}(k+1)]$. This means that the diffusion term which normally tends to smooth out any temperature gradient, would increase the temperature gradient if certain conditions are met. We will derive the conditions under which such nonphysical results are obtained from the finite-difference scheme. Mathematically, $A(2) \geq |A(1)|$ implies that,

$$q \frac{\partial \ln K_t}{\partial y} \geq \left| 2 - \frac{\partial^2 y / \partial z^2}{\frac{\partial y}{\partial z}} \right|^2 \qquad \text{(C.124)}$$

Equation (C.124) can be put into a finite-difference formula and, for the grid usually used in our simulations, requires a variation in K_t of an order of magnitude between two successive grid points. Excessive cooling or warming will be computed whenever condition (C.124) is met. This problem can be partly cured by imposing that $A(2) \leq |A(1)|$ at all time steps. But this is an arbitrary assumption

which interferes with the computational scheme. The inclusion of the time derivative term adds very little, and the condition $A(2) \leqslant |A(1)|$ insures now that,

$$\textcircled{H}(k,t_o+\Delta t) \in [\textcircled{H}(k,t_o),\textcircled{H}(k-1,t_o+\Delta t),\textcircled{H}(k+1,t_o+\Delta t)] \quad (C.125)$$

C.5.2. Blocking of the Height of the Daytime Inversion.

Another prdblem related to the use of (3.28) appears a few hours after sunrise when the inversion height, after rising relatively well, suddently refuses to move higher than about 50 m. This produces a very unstable surface layer capped by a very stable layer. The causes for that behavior are a complex interaction between K_t, $\overline{\theta^2}$ and $\textcircled{H}$.

1. K_t depends strongly on the sign of the temperature gradient. A small value of K_t is obtained in stable cases and a large one in unstable cases. The difference in sign of the temperature gradient means usually a few orders of magnitude difference in the computed value of K_t.

2. $\overline{\theta^2}$ should nearly vanish whenever the temperature gradient decreases to a very small value. Below the inversion, in the unstable region, $\overline{\theta^2}$ is relatively large. In the stable region above the inversion, $\overline{\theta^2}$ is again important where the temperature gradient is large. Therefore, we expect a minimum in $\overline{\theta^2}$ at the inversion. However, the value of this minimum becomes dominated by the diffusion term and the time-dependent terms in (3.32) and no longer by the temperature gradient term. That means that $\overline{\theta^2}$ does not vanish in the limit of a very small temperature gradient.

3. The equation for Θ is not solved in terms of the vertical variation of the heat flux. Consequently, the computed temperature profile cannot force alone the lifting of the inversion height, but permits very often the existence of a very unstable layer capped off by a very stable layer.

In the equation for K_t the product $\overline{\theta^2}\,\frac{\partial \Theta}{\partial z}$ appears. Near the inversion, $\overline{\theta^2}$ is larger than expected from the limit $\Delta\Theta \to 0$ and $\frac{\partial \Theta}{\partial z}$ is positive. This gives a very small value to K_t, which in turns prevents the lifting of the inversion height. In order to lift the inversion height we would need $\Delta\Theta < 0$, which causes large values for $\overline{\theta^2}$ and K_t. This would maintain the inversion height at a relatively high position. The computational scheme seems to be able to lift the inversion height under some conditions which are not always met. One way of curing the problem is to neglect the time-dependent and the diffusion terms in (3.32) near the inversion height. This allows a smaller value for $\overline{\theta^2}\,\frac{\partial \Theta}{\partial z}$ near the inversion height, which permits a l... value for K_t and which ultimately will lead to the lifting of he inve...ion height. However, this method of solving the problem ca... ...tiate some oscillations caused by the variations in $\overline{\theta^2}$ because we are using two different formulas to compute $\overline{\theta^2}$. Therefore, convergence is not readily insured at each time step.

C.6 Refinements to the Finite-Difference Equations.

C.6.1 Double Precision.

Near the top of the boundary layer, the mean atmospheric variables vary slowly both in the vertical and in time. However, the coefficients of eddy diffusivity and the other turbulent quantities vary appreciably in that region and their exact value depend to a great extent on the gradient of the mean atmospheric variables. Therefore, in order to get a good estimate of the turbulent quantities we need a fairly accurate evaluation of the mean variables. This implies that double precision is generally needed for U, V, Ⓗ and Q whereas single precision is probably always sufficient for all of the other atmospheric variables. The great inconvenience of double precision is that it requires 2 to 4 times the computing time of single precision. Consider a specific example in which we assign 7 decimal digits to single precision and 14 decimal digits to double precision. We define an elementary operation as the operation between two digits. We will compare the number of elementary operations required for addition and multiplication in single precision with the number of similar operations in double precision. We consider two numbers A and B which consist of n digits each,

$$A = x_1\, x_2 \cdots x_n \qquad (C.126)$$

$$B = y_1\, y_2 \cdots y_n \qquad (C.127)$$

The addition A+B involves n elementary addition of the type x_i+y_i. If $x_n+y_n \geqslant 10$ we add 1 to x_{n-1}. There is on the average a 50% probability that this additional operation has to be done. Therefore, an addition requires 3 n/2 elementary operations.

Table 10. Average number of elementary operations for addition and multiplication in single and double precision when we use the decimal system.

operation \ precision	single 7 digits	double 14 digits
addition	10	21
multiplication	126	509

Table 11. Average number of elementary operations for addition and multiplication in single and double precision when we use the binary system.

operation \ precision	single 7 digits	double 14 digits
addition	9	18
multiplication	102	399

By similar reasoning we can estimate that an average multiplication will require about $\left[(n-1)^2 + n^2\right]3/2$ elementary operations. Table 10 compares the number of elementary operations required in single precison and in double precision for the operations of addition and the operations of multiplication in the decimal system. Table 11 does the same comparison in the binary system. The most important conclusion which can be drawn is that addition requires only about twice as much computing in double precison with respect to single precision, whereas multiplication in double precision needs at least 4 times the computing time of a single pecision multiplication. Therefore, if we want to save computing time, we should try to reduce the number of multiplications which are done in double precision. For example the temperature difference $\Theta(k+1) - \Theta(k-1)$ is computed in double precision and the resulting value is put in a single precision variable DT1. This temperature difference is needed, for example, in the computation of some of the turbulent variables. By using DT1 we do not lose any significant information and we gain by reducing the number of computations performed in double precision.

C.6.2 Minimization of Round-Off Errors.

The round-off errors can be very important near the top of the boundary layer. During some numerical experiments these have been observed to add up consistently. This effect was most visible on the temperature profile which showed an increasingly large temperature gradient between the top two grid points. When the computations were done in single precision this was enough to prevent the convergence of the model. In double precision the problem is somewhat

reduced but problems can arise if the model is run long enough. Therefore, it seems important to devise a finite-difference scheme which reduces the possible round-off errors. This is achieved mostly by being careful in choosing the order of the operations inside an expression. We will take the example of a constant isentropic atmosphere, for which a round-off error will mean a deviation from the constant value. Ordinarily the computer transforms the decimal numbers into hexadecimal numbers. There are a few operations in real number arithmetics which should not give any round-off errors. These are

1- The hexadecimal representation of a small real decimal number without any decimal part is exact. For example 3. would have an exact hexadecimal representation whereas 0.3×10^1 would not.

2- The difference A - A = 0. exactly.

3- The division A/A = 1. exactly.

4- The sum A + 0. = A exactly.

5- The operations Ax1 = A and A ÷ 1 = A exactly.

6- The addition or subtraction of two small real numbers without any decimal part is exact.

There are other operations which may give round-off errors:

1- The multiplication between two real numbers A and B, followed by the division by B, gives A with a round-off error. (A x B)/B = A + round-off error. This round-off error could be prevented by changing the order of the operations: A x (B/B) = A x (1) = A without round-off error.

2- The operation (A + A)/A gives 2 with a round-off error. This can be cured by (A/A + A/A) = 1. + 1. = 2. exactly.

We go back to (C.26) in which D(k,3) is identically zero for a constant-temperature profile because $DT1\big|_{t_o}$ and $DT2\big|_{t_o}$ are exactly zero according to operation 2 which is the difference between two equal numbers. We note that $DT1\big|_{t_o+\Delta t}$ is also identically zero for the same reason. We are left with

$$\widehat{\textcircled{H}}(k,t_o+\Delta t) = \left\{\textcircled{H}(k,t_o)/\Delta t + A(5)\left\{\tfrac{1}{2}\left[\textcircled{H}(k+1,t_o+\Delta t)+\textcircled{H}(k-1,t_o+\Delta t)\right]\right\}\right\}/\left[1/\Delta t+A(5)\right]$$

The operation $\frac{1}{2}\left\{\textcircled{H}(k+1,t_o+\Delta t)+\textcircled{H}(k-1,t_o+\Delta t)\right\}$ may or may not give a round-off error in the case of an isentropic atmosphere. For example, we suppose a four-digit accuracy and $\textcircled{H}$ = 501.3. The real sum is 1002.6 which is transformed in four-digit accuracy into 1003. with a round-off error of 0.4. The subsequent division by 2 yields 501.5 with a round-off error of 0.2. However if $\textcircled{H}$ = 301.3, the sum is 602.6 and the divison by 2 gives back 301.3 with no round-off errors. Therefore, we suppose temporarily that there is no round-off errors for that operation. We have the ratio

$$\textcircled{H} = \frac{\textcircled{H}/\Delta t + A(5)\ \textcircled{W}}{1/\Delta t + A(5)}$$

The operation $\textcircled{W}/\Delta t$ and $A(5)\,\textcircled{H}$ are very likely to have round-off errors as well as the subsequent addition. Therefore, that formulation is very likely to give rise to round-off errors. However, if we rearrange the terms as,

$$\textcircled{H} = \textcircled{H}\left[\frac{1/\Delta t + A(5)}{1/\Delta t + A(5)}\right]$$

The factor $1/\Delta t + A(5)$ is common to both the denominator and the numerator and will give some answer B with round-off errors with respect to the true solution. This is not important as B/B = 1 without any round-off error, and $\textcircled{H}$ is computed without any round-off

error. Therefore, the best finite-difference equation isolates and factor A(5). Equation (C.26) is rewritten as

$$\textcircled{H}(k,t_o+\Delta t) = \textcircled{H}(k,t_o)\left\{(1/\Delta t+A(5))\left\{\left[DDT/\textcircled{H}(k,t_o)+D(k,3)/\textcircled{H}(k,t_o)\right]/2\right\}\right.$$
$$\left./(1/\Delta t + A(5))\right\}$$

We have noted that in actual numerical tests $DDT/\textcircled{H}(k,t_o)$ gave exactly 2. with no round-off errors. This implies that there is no need to extend the division inside DDT. The rearrangement of the terms is effected for all the other finite-difference equations for the mean quantities.

C.6.3 Higher-Order Approximation to the Derivatives.

In Section 3.4 we have devised finite-difference approximations to the first and second derivatives which were more exact by an order of approximation in the Taylor Series. As pointed out previously there is no need for the improved and time consuming second-order approximation to the derivatives in the regions where the atmospheric variables are varying gently, namely in the surface layer and in the upper boundary layer. The higher-order approximation is optional in the time-dependent model and is used in the region determined by the range $[m(4),m(3)]$, where m is an integer variable used in the program.

C.6.4 Restriction on the Temperature Profile.

As noted in Section C.5, (3.28) has a tendency to create many stable-unstable transitions. We can devise limits to the temperature at each grid point based on the principle that there is no internal energy source term and that warming and cooling can only

come from the other levels. In the program we have called

$$D(k_o,10) = Ⓗ(k_o+1,t_o) - Ⓗ(k_o,t_o)$$

which represents the stability at the past time step above the grid point k_o. At the actual time step, the stability around k_o is defined by

$$SIGN = Ⓗ(k_o+1,t_o+\Delta t) - Ⓗ(k_o-1,t_o+\Delta t)$$

From the knowledge of these two variables we want to impose a restriction on $Ⓗ(k_o,t_o+\Delta t)$. As an example, we suppose that $D(k_o, 10)$ is positive, which implies stability above the grid point k_o at the past time step. If SIGN is also positive, that implies that the layer around k_o at the actual time step is also stable. The restriction to $Ⓗ(k_o,t_o+\Delta t)$ is to impose the condition that it must be smaller than $Ⓗ(k_o+1,t_o+\Delta t)$. Only when $Ⓗ(k_o-1,t_o)$ is greater than $Ⓗ(k_o,t_o)$ is it possible to expect that the restriction interferes with a real change in stability. But this case is certainly rare as it would require very rapid changes in the surface temperature. We tabulate all the possible combinations of $D(k_o,10)$ with SIGN and the restriction imposed on $Ⓗ(k_o,t_o+\Delta t)$ in Table 12. This restriction on the temperature is optional in the time-dependent model. It can be imposed for any layer that we wish, it can be done during the computations at each grid point or after a complete iteration has been completed. Whenever the restriction is imposed, we reset $Ⓗ(k_o,t_o+\Delta t)$ within the range $\left[Ⓗ(k_o+1,t_o+\Delta t), Ⓗ(k_o-1,t_o+\Delta t)\right]$.

Table 12. Restriction on $\textcircled{H}(k_o,t_o+\Delta t)$. We define:

$$D(k_o,10) = \textcircled{H}(k_o+1,t_o) - \textcircled{H}(k_o,t_o)$$

and

$$SIGN = \textcircled{H}(k_o+1,t_o+\Delta t) - \textcircled{H}(k_o-1,t_o+\Delta t)$$

SIGN \ $D(k_o,10)$	positive	negative
positive	$< \textcircled{H}(k_o+1,t_o+\Delta t)$	$> \textcircled{H}(k_o-1,t_o+\Delta t)$
negative	$< \textcircled{H}(k_o-1,t_o+\Delta t)$	$> \textcircled{H}(k_o+1,t_o+\Delta t)$

APPENDIX D

INFRARED FLUX DUE TO WATER VAPOR

D.1 Hypotheses.

The following hypotheses are made in order to simplify the computational task:

Hypothesis 1: the pressure at the roughness height is constant at all times. This implies that the pressure at the top of the boundary layer will vary.

Hypothesis 2: we neglect the infrared flux emitted by the layer between z_o and the ground. This layer is fairly thin and the infrared flux received at the earth's surface is not modified sensibly by neglecting the contribution from that layer.

Hypothesis 3: the layer above the boundary layer is not modelled and we neglect the infrared flux coming from that layer. That assumption is justified by the relatively rapid decrease in the mixing ratio with height and by the fact that most of the infrared flux emitted by water vapor and received at the ground is emitted in the lowest 100 meters of the boundary layer.

Hypothesis 4: only the mean infrared flux will be considered and consequently we will use only the mean atmospheric variables in our computations.

Hypothesis 5: the hydrostatic equation will be used to compute the mean pressure.

D.2 Computation of Temperature.

In the computation of the infrared radiation we need the temperature which can be obtained from the definition of potential temperature. In index form we have

$$T(k) = \Theta(k)\left[\frac{P(k)}{P_o}\right]^K \qquad (D.1)$$

where $K = R/C_p$ and P_o = reference pressure = 1000 mb.

D.3 Computation of Pressure.

We use the hydrostatic approximation

$$\frac{\partial P}{\partial z} = -\rho g \qquad (D.2)$$

The perfect gas law is

$$P = \rho R T_v \qquad (D.3)$$

The virtual temperature T_v is related to the temperature T and to the mixing ratio Q by the approximate expression

$$T_v = T (1 + 0.6078 Q) \qquad (D.4)$$

Combining these equations with (D.1) we obtain

$$P^{K-1} \frac{\partial P}{\partial z} = -\frac{g P_o}{R \Theta (1+0.6078 Q)} \qquad (D.5)$$

$$\frac{1}{K} \frac{\partial P^K}{\partial z} = -\frac{g P_o}{R \Theta (1+0.6078 Q)} \qquad (D.6)$$

Equation (D.6) has isolated the pressure and will be used in a finite-difference form

$$P(k+1) = P(k)\left[1 - \frac{2 g (P_o)^K / DELZ(k+\frac{1}{2})}{C_p P(k)^K [\Theta(k+1)+\Theta(k)]\{1+0.3039[Q(k+1)+Q(k)]\}}\right]^{1/K} \qquad (D.7)$$

D.4 Equation for the Infrared Flux.

The basic equations for the infrared flux are (5.9) and (5.10) which we recall here,

$$F_w(0) = \sum_{k=1}^{n} (\overline{\sigma T^4})\Big|_k \left(\frac{\partial \varepsilon}{\partial u}\right) \Delta u \qquad (D.8)$$

$$\Delta u = \overline{P}\,\overline{Q}\,\frac{\Delta P}{g} \qquad (D.9)$$

where $F_w(0)$ = infrared flux received at z_o due to water vapor

n = index of the top level considered

ε = emissivity of water vapor

$\overline{P}$ = average pressure of the layer [mb]

$\overline{Q}$ = average mixing ratio in the layer (g/g)

g = gravity = 980 cm /sec^2

$\overline{T}_k$ = average temperature of the layer (°K)

Δu = path length in a given layer (cm)

σ = Stefan-Boltzmann constant.

We will consider the layers between grid points. An average quantity in the layer will be taken as the arithmetic mean of the value of that quantity at the upper grid point and of its value at the lower grid point. For example, the average pressure is,

$$\overline{P} = [P(k+1) + P(k)]/2$$

Therefore, (D.9) is written in finite-difference form as,

$$\Delta u = [P(k+1)+P(k)][P(k+1)-P(k)][Q(k+1)+Q(k)]/(4\,g) \qquad (D.10)$$

The total path length w is defined as the sum of all the path lengths contained in the layers between z_o and the top of the layer under consideration,

$$w = \sum_{(z_o)}^{(top)} \Delta u \qquad (D.11)$$

The slope of the emissivity curve can be derived from Table 2,

$$\frac{\partial \varepsilon}{\partial u} = \frac{0.1579}{1+4275\ w} \qquad \text{for} \quad 0 < w < 10^{-4} \qquad (D.12)$$

$$\frac{\partial \varepsilon}{\partial u} = \frac{0.0396}{w} \qquad \text{for} \quad 10^{-4} < w < 10^{-3} \qquad (D.13)$$

$$\frac{\partial \varepsilon}{\partial u} = \frac{0.0565}{w} \qquad \text{for} \quad 10^{-3} < w < 10^{-2} \qquad (D.14)$$

$$\frac{\partial \varepsilon}{\partial u} = \frac{0.0653}{w} \qquad \text{for} \quad 10^{-2} < w < 10^{-1} \qquad (D.15)$$

$$\frac{\partial \varepsilon}{\partial u} = \frac{0.0778}{w} \qquad \text{for} \quad 10^{-1} < w \qquad (D.16)$$

The finite-difference equation corresponding to (D.8) is,

$$F_w(0) = \sum_{k=1}^{n} \sigma (T^4(k+1) + T^4(k)) \left(\frac{\partial \varepsilon}{\partial u} \right)_k (\Delta u)_k / 2 \qquad (D.17)$$

D.5 Computation of the Infrared Flux.

All the quantities can now be computed and the successive steps in the computation of the infrared flux are,

D.5.1 For the Lower Boundary:

Step 1: Compute from (D.1) the temperature at z_o.

D.5.2 For the Other Levels.

Step 2: the pressure at the grid point k+1 is computed from (D.7).

Step 3: the temperature at the grid point k+1 is computed from (D.5).

Step 4: Δu is computed from (D.10).

Step 5: the total path length w is computed from (D.11).

Step 6: the contribution to the infrared radiation from each layer is

computed from (D.12)

D.5.3. Integrated Result.

Step 7: finally the contribution from each layer to the infrared flux is added up to give the total infrared flux received at the ground.

APPENDIX E

SOLUTION OF THE SURFACE TEMPERATURE EQUATION

We will use the results obtained in Chapter V and transform the equations into a finite-difference form. Equation (5.20) becomes,

$$E = KW(2)*(Q(3)-Q(1))*DELZ(2)/2 \qquad (E.1)$$

where KW(k) = coefficient of eddy diffusivity for water vapor at grid point k = ℓ + 1

DELZ(k) = the derivative of ℓ with respect to z at grid-point k

Q(k) = mixing ratio at grid-point k

Equation (5.19) is transformed into

$$S = KS(2)\ (TS(3)-TS(1))\ DDZ(2)/2 \qquad (E.2)$$

where KS(1) = molecular coefficient of diffusivity in the soil at grid-point 1 = ξ + 1

TS(1) = soil temperature at grid-point 1

DDZ(1) = first derivative of ξ with respect to z_s at grid-point 1.

The equation for the atmospheric-sensible-heat flux involves the potential temperature whereas all the other terms in (5.1) contain the temperature. This is why we transform (5.13) into a form compatible with the other terms. The equation for the potential temperature is

$$\textcircled{H} = T\ \left(\frac{1000}{p}\right)^{K} \qquad (E.3)$$

where $K = R/C_p = 2/7$

Taking the derivative of the logarithm of (E.3), we have

$$\frac{\partial \ln \Theta}{\partial z} = \frac{\partial \ln T}{\partial z} - K \frac{\partial \ln p}{\partial z} \qquad (E.4)$$

We use the hydrostatic approximation in (E.4) so that

$$\frac{\partial \Theta}{\partial z} = \frac{\Theta}{T} \left(\frac{\partial T}{\partial z} + \frac{g}{C_p} \right) \qquad (E.5)$$

Equation (E.5) becomes, in a finite-difference form,

$$\Delta\Theta = (\Delta T + \Delta z \; g/C_p)\Theta/T \qquad (E.6)$$

The integral form of (5.13) is

$$\Delta\Theta = \frac{H}{k_o \, u_*} P_{rt} \ln \left(\frac{z+z_o}{z_o}\right) \qquad (E.7)$$

We combine the last two equations and obtain

$$H = \frac{k_o \, u_*}{P_{r_t} \ln (z+z_o)/z_o} \frac{[\Theta(2) - \Theta(1)]}{[T(2) - T(1)]} [\Theta(2) + \Theta(1)] + \frac{g}{C_p} z(2) \qquad (E.8)$$

In the last expression we have evaluated the finite-difference equation betwee z_o and the first grid point. We combine the outgoing terrestrial infrared radiation with the sky infrared radiation due to CO_2,

$$R\uparrow = \varepsilon \sigma T^4(0) \qquad (E.9)$$

where $\varepsilon = (1 - 0.18)\varepsilon_1$ = effective emissivity of the ground.

The infrared radiation from water vapor (F_w) has been computed in Appendix D, and the incoming solar radiation (I_a) has been defined in Chapter V. Therefore, the following equation results if we group all the results,

$$T^4(0) + C(2) \; T(0) + C(1) = 0 \qquad (E.10)$$

where,

$$C(2) = \frac{\rho_s\, c_s\, K_s\, DDZ(2)/2 + BB}{\varepsilon\, \sigma}$$

$$BB = \rho\, C_p\, \frac{k_o\, u_*}{P_{rt}(\ln\,(z+z_o)/z_o)}\left[\frac{\textcircled{H}(2) + \textcircled{H}(1)}{T(2) + T(1)}\right]$$

$$C(1) = -\,\frac{\left[I_a + F_w + L\, K_w(2)\, Q(3) - Q(1)\, DELZ(2)/2 + BB\, T(2) + \frac{g z(2)}{C_p}\right]}{\varepsilon\, \sigma}$$

Equation (E.10) can be solved exactly. We will follow the steps outlined in the 14th Edition of the CRC Abridged Mathematical Tables (1967), pp. 291-293. This requires that we solve first a resolvent cubic equation, whose solution gives the desired solution to the quartic equation after a few manipulations. The procedure will be simplified by making use of the fact that C(1) is always negative and that C(2) is always a real number.

E.1 Solution of the Resolvent Cubic Equation.

The quartic equation to be solved is of the type

$$x^4 + a\, x^3 + b\, x^2 + c\, x + d = 0 \qquad (E.11)$$

where

$$a = b = 0$$

$$c = C(2) \geqslant 0$$

$$d = C(1) \leqslant 0$$

The resolvent cubic equation is

$$y^3 + e\, y + f = 0 \qquad (E.12)$$

where

$$e = -\,4\, d = -\,4\, C(1) \geqslant 0$$

$$f = -\,c^2 = -\,[C(2)]^2 \leqslant 0$$

Now we let

$$A = \left(-\frac{f}{2} + \left(\frac{f^2}{4} + \frac{e^3}{27}\right)^{\frac{1}{2}}\right)^{\frac{1}{3}} \qquad (E.13)$$

$$B = \left(-\frac{f}{2} + \left(\frac{f^2}{4} + \frac{e^3}{27}\right)^{\frac{1}{2}}\right)^{\frac{1}{3}} \qquad (E.14)$$

The three solutions are

$$y_1 = A + B \qquad (E.15)$$

$$y_2 = -\tfrac{1}{2}\left[(A+B)-(A-B)(-3)^{\frac{1}{2}}\right] \qquad (E.16)$$

$$y_3 = -\tfrac{1}{2}\left[(A+B)-(A-B)(-3)^{\frac{1}{2}}\right] \qquad (E.17)$$

If the disciminant $\left(\frac{f^2}{4} + \frac{e^3}{27}\right)$ is

> 0 we have one real root and two imaginary roots,

$=0$ we have three real roots of which at least two are equal,

< 0 we have three unequal real roots.

In our case

$e^3 > 0$ because e is always positive, and

$f^2 > 0$ because f is real.

Therefore, the discriminant is always positive and the only real root is y_1. We define the following variables:

$$C(3) = -\tfrac{1}{2} f = C(2)\ C(2)/2 \qquad (E.18)$$

$$C(4) = f^2/4 = C(3)\ C(3) \qquad (E.19)$$

$$C(5) = e^3/27 = -\left[C(1)^{1/3}\right] 64/27 \qquad (E.20)$$

The discriminant is

$$DIS = C(4) + C(5) \qquad (E.21)$$

The constants A and B are, therefore,

$$C(7) = A = \left[C(3) + SQRT(DIS)\right]^{1/3} \qquad (E.22)$$

$$C(8) = B = \left[C(3) - SQRT(DIS)\right]^{1/3} \qquad (E.23)$$

where SQRT = square root of the function inside the parenthesis. Therefore, the solution of the resolvent cubic equation is

$$Y1 = C(7) + C(9) \qquad (E.24)$$

We note that B is always negative but smaller in absolute value than A, so that Y1 is always positive.

E.2 Solution of the Quartic Equation.

We define R as

$$R = (a^2/4 - b + Y1)^{\frac{1}{2}} = SQRT(Y1) \qquad (E.25)$$

Therefore, R will always be real and positive. In this case we define D and E as

$$D = (-R^2 - 2\ c/R)^{\frac{1}{2}} \qquad (E.26)$$

$$E = (-R^2 + 2\ c/R)^{\frac{1}{2}} \qquad (E.27)$$

We must eliminate all of the non-physical roots. c = C(2) is always positive which implies that D is an imaginary number and is rejected for that reason. E is the only real root for which the following inequality must be satisfied:

$$-R^2 + 2\ c/R \geq 0 \qquad (E.28)$$

The two possible solutions are

$$x = \tfrac{1}{2} (- R \pm E) \qquad (E.29)$$

As R and E are both positive, the only positive real solution of the quartic equation is

$$x = \tfrac{1}{2} (- R + E)$$

APPENDIX F

LIST OF SYMBOLS

α kinematic coefficient of viscosity for heat

also roughness angle; angle between the lower boundary layer wind and the geostrophic wind

γ ratio of the heat capacity at constant pressure over the heat capacity at constant volume for air

δ Kronecker's delta

also solar declination

Δ finite difference operator

partial derivative operator

ε alternating tensor

also ratio of the gas constant for dry air over the one for water vapor

also effective emissivity of the earth's surface

ε_1 emissivity of the earth's surface

φ latitude

K ratio of the gas constant over the heat capacity at constant pressure for the air

λ, Λ various length scales

μ, μ_* first and second coefficients of viscosity

μ^T molecular coefficient of diffusion for heat

ν kinematic coefficient of viscosity

ρ, ρ_s density of the air and density of the soil

σ rate of strain

also frequency in the Fourier analysis

also Stefan-Boltzmann's constant

τ stress

Θ, θ mean and fluctuating potential temperature

ξ soil logarithmic coordinates

η atmospheric log-linear coordinates

ψ zenith angle

Ω earth's angular velocity

a albedo

also constant between $\frac{1}{2}$ and 1 used in the expression for the path length for water vapor

also departure from isotropy in the ordering of terms

A,B various constants

B_ν blackbody radiance

C_p, C_v heat capacities of dry air at constant pressure and at constant volume

C_{p_v} heat capacity of water vapor at constant pressure

C set of constants used in the computations of the surface temperature

c_s soil heat capacity

CST coefficient of $U(k,t_o+\Delta t)$ and $V(k,t_o+\Delta t)$

CST2 coefficient of $\Theta(k,t_o+\Delta t)$

CST3 coefficient of $Q(k,t_o+\Delta t)$

d total derivative operator

also half the soil depth in Myrup's (1969) model

D amplitude of the Fourier modes

DDZ derivative of ξ' with respect to the soil linear coordinate

DD2Z second derivative of ξ' with respect to z_s

DDZ2 square of DDZ

DELZ first derivative of ℓ with respect to z

DELZZ ratio of the ℓ-derivative of l over l^2

DEL2Z second derivative of ℓ with respect to z

DELZ2 square of DELZ

DIFF constant used in various expressions

DL first derivative of l with respect to ℓ

DEL first derivative of e l with respect to ℓ

$\mathcal{D}$ diffusion operator

e $\overline{u_1 u_1}$

also partial pressure of water vapor

also coefficient in the resolvent cubic equation used to find the surface temperature

E latent heat flux

also part of the solution of the quartic equation

f Coriolis parameter

ϕ also used to represent any function

also one of the coefficients in the resolvent cubic equation

F_{comp} computed value of a function F

F_{past} last iterative value of a function F

F_{new} new iterative value of F

F flux

F_w total infrared sky radiation received at the earth's surface

H sensible heat flux from the atmosphere

i	$\sqrt{-1}$
	also an index
I_a	net solar radiation
I_ν	intensity of radiation at frequency ν
IKM	level at which the iterative formula computing the grid point height changes
IKP	IKM + 1
j	a general index
$\vec{k}$	wavenumber vector
k	grid point
k_o	von Karman's constant
	also a specific grid point
K_m	coefficient of eddy diffusivity for momentum
K_s	molecular soil thermal conductivity
K_t	coefficient of eddy diffusivity for heat
K_w	coefficient of eddy diffusivity for water vapor
k	absorption coefficient of water vapor in a thin layer
K_{ijkl}	fourth-order tensor relating σ_{ij} to the gradient of the mean wind
l	wavenumber
	also a general index
ℓ	mixing length
ℓ_o	maximum size of the eddies
L	latent heat of vaporization
m	number of increments in Taylor's series
n	represents various exponents

NS	top of the boundary layer in terms of k = ℓ + 1
OMEGA	acceleration factor in the Gauss-Seidel iteration scheme
p	pressure
P_o	reference pressure = 1000 mb
P_{r_t}	turbulent Prandtl number
q,Q	fluctuating and mean mixing ratio for water vapor
R	gas constant of the dry atmosphere
R_w	gas constant of the water vapor
R↓	infrared sky radiation
R↑	terrestrial outgoing infrared radiation
R_o	solar constant
R_n	net radiation at the surface of the earth
S	entropy
S_a	entropy of dry air
S_v	entropy of the water vapor
S	soil heat flux
t	time
T	absolute temperature
T_v	virtual temperature
T_r	transmissivity of the cloudless atmosphere
T_{runc}	truncation error
u,U	fluctuating and mean winds along the x direction
u_*	friction velocity
v,V	fluctuating and mean winds in the y direction
V_g	geostrophic wind

w,W	fluctuating and mean winds in the z direction
w	path length in water vapor
x	the first Cartesian coordinate in the horizontal
y	the second Cartesian coordinate in the horizontal also solution of the resolvent cubic equation
z	vertical Cartesian coordinate
Z	zenith solar angle
z_s	roughness height
ZS	proportion at each grid point of the total temperature difference between the surface and the bottom of the soil layer
z_o	roughness height
z_1	canopy height in Myrup's (1969) model
z_2	top of the boundary layer in Myrup's model